University of Liege

Faculty of Sciences

ELECTRICAL AND OPTICAL CHARACTERIZATION OF AZO/Cu_2O:Mg TRANSPARENT SEMICONDUCTING HETEROJUNCTIONS GROWN BY RF MAGNETRON SPUTTERING

Author:
Thomas Ratz

Supervisor:
Ngoc Duy Nguyen

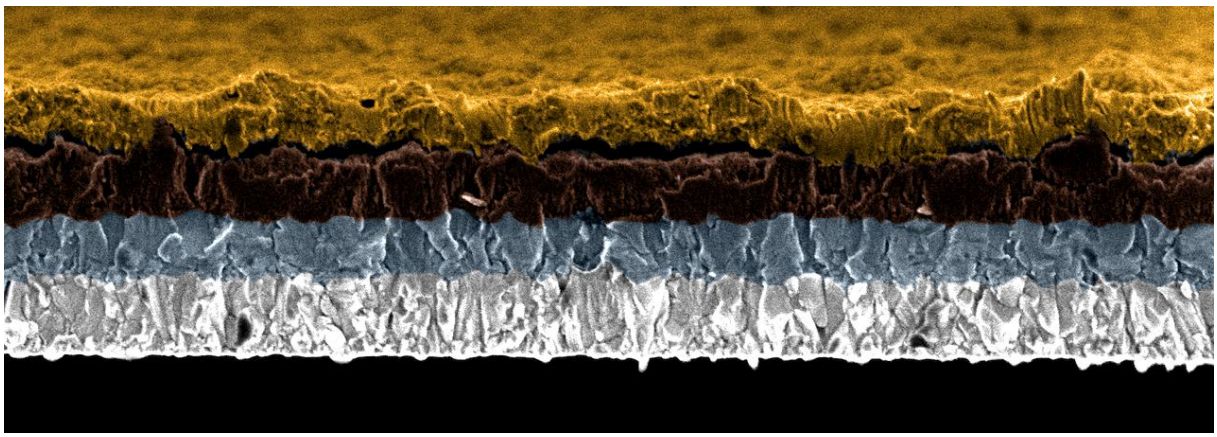

Master Thesis presented in partial fulfilment of the requirements for the master degree in Physical Sciences

Academic Year 2017-2018

Acknowledgements

My deepest acknowledgements to Dr. Ngoc Duy Nguyen for giving me the opportunity to realize this final master thesis in his research group. His guidance and his trust were precious to the proper achievement of this work. I also want to specifically thanks Emile Fourneau for all the countless ideas and suggestions he provided. His support and usual good mood contribute to the pleasure taken during this master thesis.

I would like to acknowledge Dr. Alejandro Silhanek, Dr. Peter Schlagheck and Dr. Geoffroy Lumay for their participation in my thesis committee.

I am grateful to the SPIN and EPNM research groups for their scientific advices and their support. Especially Joseph Lombardo for his time and knowledge during the SEM imaging and Dr. Jeremy Brisbois, Sylvain Blanco Alvarez, Xavier Baumans and Sunil Channam for the set up of a fun, motivating and working atmosphere. I am also grateful to Dr. Laura Manceriu for his assistance in the optical characterization.

I particularly thanks François Chaltin for the unlimited bad faith he demonstrated during these 5 years by chasing the first place against me. His friendship and support during the work and the parties have contributed to the success and the pleasure taken during these studies. I also want to acknowledge Pierre, Miguel and Alexis for their help and support during these five years.

Finally, it would be difficult to thanks sufficiently my sister, my mother, my father and my whole family for their support and their confidence not only during these studies but during these 22 years. My deepest thanks to my friends and Eloïse for their encouragements and trust.

Liege, 1st of June 2018

"*Science research is answering questions with an exponentially increasing amount of questions.*"

Contents

List of Figures

Notations and Physical Constants

Notation	Physical quantity	Units	Constant Value
α	Absorption coefficient	m^{-1}	
$\mathcal{A}$	Absorptance	%	
B	Bimolecular Recombination Coefficient	$m^{-3}s^{-1}$	
$\mathbf{B}$	Magnetic Field	T	
c	Speed of Light	ms^{-1}	299 792 458
χ	Electronic Affinity	eV	
$\mathcal{D}$	Distance between two absorption sites	m	
D_n	Electron Diffusion Constant	m^2s^{-1}	
D_p	Hole Diffusion Constant	m^2s^{-1}	
DR	Deposition Rate	$Ås^{-1}$	
η_{int}	Internal Quantum Efficiency	%	
η_{ext}	External Efficiency	%	
η	Global Efficiency	%	
ϵ	Electrical Permittivity	Fm^{-1}	
ϵ_0	Vacuum Electrical Permittivity	Fm^{-1}	$8.854\ 10^{-12}$
ϵ_r	Relative Electrical Permittivity	/	
E	Energy	eV	
E_{C}	Conduction Band Energy	eV	
E_{chem}	Chemisorption Binding Energy	eV	
E_{F}	Fermi Level	eV	
E_{g}	Band Gap Energy	eV	
E_{I}	Intrinsic Energy Level	eV	
E_{phys}	Physisorption Binding Energy	eV	
E_{S}	Activation Energy	eV	
E_{T}	Trap Level Energy	eV	
E_{V}	Valence Band Energy	eV	
E_{vac}	Vacuum Energy	eV	
$\mathbf{E}$	Electric Field	Vm	
F_{n}	Electrons Quasi-Fermi Level	eV	
F_{p}	Holes Quasi-Fermi Level	eV	
F_{T}	Electrons on Traps Quasi-Fermi Level	eV	
G	Generation Rate	$m^{-3}s^{-1}$	
γ	Surface Tension	Nm^{-1}	
h	Planck Constant	Js	$6.626\ 10^{-34}$
$\hbar$	Reduced Planck Constant	Js	$1.054\ 10^{-34}$
$\mathcal{I}$	Luminous Intensity	cd	
I	Current	A	

Notation	Physical quantity	Units	Constant Value
I_{S}	PN-Junction Saturation Current	A	
J	Current Density	Am^{-2}	
J_{i}	Incident Flux	$\mathrm{m}^{-2}\mathrm{s}^{-1}$	
J_{r}	Chemically Absorbed Flux	$\mathrm{m}^{-2}\mathrm{s}^{-1}$	
J_{v}	Re-evaporation Flux	$\mathrm{m}^{-2}\mathrm{s}^{-1}$	
k_B	Boltzmann Constant	JK^{-1}	$1.380\ 10^{-23}$
$\mathbf{k}$	Wave Vector	m^{-1}	
Λ	Atomic Diffusion Length	m	
L_n	Electron Mean Diffusion Length	m	
L_p	Hole Mean Diffusion Length	m	
m_e	Electron Mass	kg	$9.109\ 10^{-31}$
$m_e^\star$	Electron Effective Mass	kg	
$m_h^\star$	Hole Effective Mass	kg	
μ_{F}	Chemical Potential	Jmol^{-1}	
μ	Charge Carrier Mobility	$\mathrm{m}^2\mathrm{s}^{-1}\mathrm{V}^{-1}$	
ν	Frequency	s^{-1}	
n	Electron Concentration	m^{-3}	
n_{T}	Electron on Trap Concentration	m^{-3}	
n	Diode Ideality Factor	/	
n_i	Intrinsic Concentration	m^{-3}	
n_{s}	Atomic Concentration on Site	m^{-3}	
N_{D}^+	Ionised Donor Concentration	m^{-3}	
N_{A}^-	Ionised Acceptor Concentration	m^{-3}	
$\mathcal{N}_{\mathcal{A}}$	Avogadro Number	mol	$6.022\ 10^{-23}$
p	Hole Concentration	m^{-3}	
q	Elementary charge	C	$1.602\ 10^{-19}$
$\mathcal{P}$	Power	W	
$\mathcal{P}_{\mathrm{R}}$	Radiative Power	W	
P	Pressure	Torr	
P_{Ar}	Argon Pressure	Torr	
R	Recombination Rate	$\mathrm{m}^{-3}\mathrm{s}^{-1}$	
$\mathcal{R}$	Reflectance	%	
R_{H}	Hall Resistance	Ω	
R_{r}	Chemisorption Rate	$\mathrm{m}^{-2}\mathrm{s}^{-1}$	
R_{P}	Leakage Resistance	Ω	
R_{s}	Barrier Overcoming Flux	$\mathrm{m}^{-2}\mathrm{s}^{-1}$	
R_{S}	Series Resistance	Ω	
R_{sheet}	Sheet Resistance	Ω	
ρ	Electrical Resistivity	$\Omega\mathrm{m}$	
ρ_{s}	Space Charge Density	Cm^{-3}	
ρ	Electrical Resistivity	$\Omega\mathrm{m}$	
σ	Capture Cross Section	m^{-2}	

Notation	Physical quantity	Units	Constant Value
t	Thickness	m	
T	Temperature	K	
T_{RTA}	RTA Temperature	°C	
T_{S}	Substrate Temperature	°C	
$\mathcal{T}$	Transmittance	%	
τ	Charge Carrier Life Time	%	
$\mathbf{v}$	Velocity	ms^{-1}	
V	Electrical Potential	V	
V_0	PN-Junction Contact Potential	V	
V_{app}	External Bias Applied	V	
V_{H}	Hall Potential	V	
W_{d}	Depletion Width	m	
W_{A}	Active Region Width	m	
ξ_{ex}	Extraction Efficiency	%	
ξ_{c}	Chemisorption probability	%	

List of Abbreviations

AZO Aluminium-doped Zinc Oxide. viii–x, 3, 4, 28, 39, 43, 44, 62, 63, 66, 70, 71, 75, 85–101, 104, 107, 108

CVD Chemical Vapour Deposition. 36

DOS Density Of States. 8, 13, 14, 27, 72, 83

EHP Electron-Hole Pair. 5, 8, 12–15, 21, 23, 68, 72, 93

FTO Fluorin doped Tin Oxide. ix, x, 76, 80, 85, 86, 89, 96–99, 101, 102, 104, 109

IEA International Energy Agency. 2

IPA Isopropanol. 41

ITO Indium Tin Oxide. 43

LED Light Emitting Diode. x, 1, 2, 4, 5, 16, 23, 25, 26, 47, 55, 72, 74, 104, 105, 108, 109

MB Maxwell-Boltzmann. 8–10, 13, 14, 57, 62

OLED Organic Light Emitting Diode. 26, 27

PMT Photomultiplier. 53

PVD Physical Vapor Deposition. 29, 36, 37, 48, 86

RF Radio Frequency. viii, x, 29, 37, 39, 42, 44, 76, 107, 108

rpm Round Per Minute. 78, 98

RT Room Temperature. ix, 75–78, 80–93, 95–98, 100, 101

RTA Rapid Thermal Annealing. ix, 37, 41, 46, 75, 89–91

sccm Standard Cubic Centimeter per Minute. 38, 77, 86, 98

SEM Scanning Electron Microscope. ix, x, 35, 44, 47, 76, 80, 84, 85, 87–89, 94–96, 101, 102, 108, 109, 117, 118

SRH Schockley-Read-Hall. 5, 14, 15

SSL Semiconductor-based Solid-state Lightning. 2

TCO Transparent Conducting Oxide. vii, x, 3, 28, 29, 42, 43, 62, 63, 75, 81, 83, 84, 94, 100, 107, 108

TED Transparent Electronic Device. vii, 2–5, 25–27, 29, 43, 47, 82, 83

TEM Tunneling Electron Miscroscope. 35

TOF-SIMS Time of Flight Secondary Ion Mass Spectroscopy. 103, 104, 109

VdP Van der Paw. viii, 47–49, 51, 100

VdW Van der Waals. 30, 31

Chapter 1

Introduction

Over the past decades, Light Emitting Diodes (LEDs) have spread into our daily life. Cheaper and more cost-efficient, they started to replace the incandescent light bulbs. As a result, nowadays LEDs, are present in many devices of our everyday environment. For example, the fields of application of LED spread from lightning, indicators, data communication, remote controls to sensors. LEDs are based on a bridge between photonics and electronics.

Before starting the description of the theory, the methodology and the results of this thesis let's take a part of this chapter to briefly summarize the history of LEDs and of the electroluminescence phenomenon [1]. The electroluminescence mechanism was first observed one century ago by Captain Henry Joseph Round, an English engineer. Indeed, in 1907, Round published in Electrical World his discovery of the electroluminescence effect [2] in which he described the observation of a glowing phenomenon when a current is applied through a contact of carborundum (SiC) and another metallic material. However, in this note, Round did not provide a correct explanation of this effect but rather established a link between the electromagnetic field produced at the junction between both materials due to a possible thermoelectric effect and the light emitted. The electroluminescence phenomenon was discovered but not understood.

In 1928, Oleg Vladimirovich Losev, a Russian scientist who made important research in semiconductor physics and more precisely in the field of semiconducting junction during his life, invented the light emitting diode [3]. It appears that Losev did not know about the note of Round. Losev published 16 papers between 1924 and 1930 which provides a comprehensive research on LED and its applications. The LED invented and studied by Losev consists in a SiC metal-semiconductor rectifier. In opposition to Round, Losev did understand the diode nature of the emission rather than hypothetic a thermal behaviour. He used the quantum theory available at this time to explain the LED emission process and called it "the inverse photo-electric effect". He also went deeper by studying for example, the current-voltage characteristic of the device and the temperature dependance of the emission. He also understood the potential of LED in telecommunication but its proposal remained unknown until the middle of the 20th century. Then SiC semiconductor-metal rectifier which emits blue light were optimised but their global efficiency still remain low ($\eta = 0.03\%$) compared to other compounds [4] as defined in a following chapter (cfr. Section 2.3). The efficiency is the ratio between the emitted light power and the supplied electrical power In the 1950s, III-V semiconductors were produced

and began to be used in LED technology [5]. First, infrared LEDs were developed using GaAs. It was the beginning of the laser diodes which have been further developed thanks to the research in heterostructures and confinement effects. Then, green and red LEDs were produced based on GaP. GaN also presented a great interest due to its band gap in the ultraviolet wavelength range. However, further developments and research in p-doped GaN growth techniques were required in order to produce an efficient blue LED. Indeed, as it is presented in Fig. 1.1, light energy efficiency has evolved over the years. Starting with rudimental technologies through the incandescent light bulb, the fluorescence and as we have seen the Semiconductor-based Solid-state Lightning (SSL), the efficiency of the devices continuously increases [6]. Since the physical properties of LEDs like the efficiency and the brightness have started to overcome the incandescent light bulb physical characteristics in nearly all wavelength ranges, incandescence light sources have started to get replaced in many fields of applications (domestic light sources, traffic indicators). In 2014, Isamu Akasaki, Hiroshi Amano and Shuji Nakamura received the Nobel prize in Physics for their work on efficient blue LEDs which allowed the production of white LEDs [5, 7]. These ones could be a partial solution to the increasing emission of carbon dioxide in the Earth atmosphere due to the world appetite for artificial light thus electrical power. And consequently, a partial solution to the global warming mankind is dealing with.

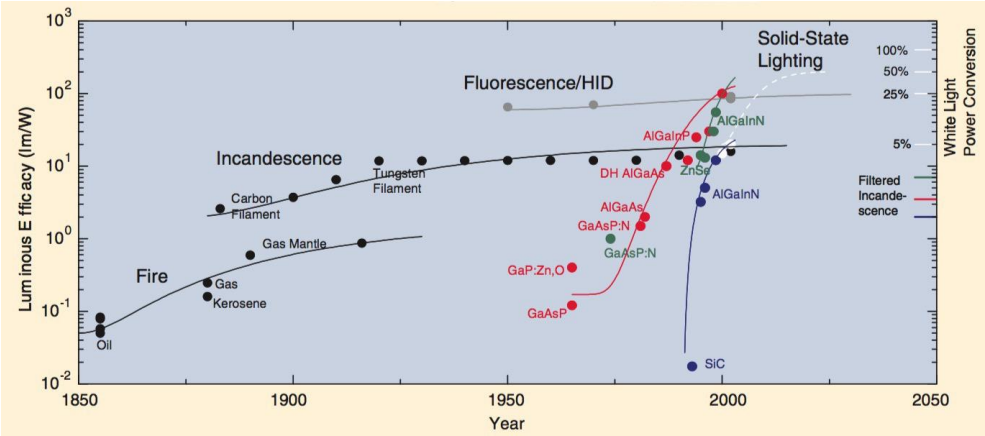

Fig. 1.1: Ratio of the luminous intensity regarding the power supplied (mainly electrical power) [lm/W] for various lightning technologies over 200 years [6]. The luminous efficiency represents the ration of the lumen flux emitted over the power supplied to the LED. the red, green and blue data stand for commercialised LEDs emitting in different wavelength range.

As it can be seen on the right scale of Fig. 1.1, the luminous efficacy in terms of electrical power conversion has nearly reach 50% for red and green LEDs. According to the projection realised, if an efficiency of 50% is achieved in all wavelength ranges, the worldwilde lightening electricity consumption would decrease by more than 50% [8, 9]. Furthermore, even if since the 17th century, the light cost has be reduced by 4.3 orders of magnitude, the light consumption has increased by 5.4 orders of magnitude [10]. And according to the International Energy Agency (IEA), lighting is responsible for 19% of energy consumption and 6% of carbon emission [11]. By consequence, the phase out of incandescent lamp [12] and the research in SSL could be a partial solution to, in one hand, sustain the world appetite for artificial light and in the other hand, to reduce the energy consumption thus the carbon dioxide emission and by consequence to tackle the global warming.

Over the last decades, in addition to the LED technology, Transparent Electronic Devices (TEDs) based on a new area of the semiconductor technology have emerged [13]. This new type of opto-electronic devices are made of Transparent Conducting Oxides (TCOs). The purpose of this technology is to use the semiconductor properties in order to produce optically transparent and electrically conductive thin films to realise transparent electronic circuits and opto-electronic devices. Nevertheless, the acquisition of these two properties for a same materials is not trivial. Indeed, the transparency is a property of insulating materials while conductive materials are generally opaque due to their natural crystalline structure and periodicity. The transparency in the visible wavelength range is obtained for high band gap semiconductors (over $\sim$ 3.1 eV) and the good electrical conductivity is achieved for high charge carrier concentrations ($\sim 10^{19}$ cm^{-3}) with high mobilities (~ 1 cm^{2}V^{-1}s^{-1}) [14]. The first TCO, In_2O_3:Sn (Indium Tin Oxide (ITO)), was reported by Rupperecht in 1954. In the next decades they were commercialised as transparent electrodes [15]. n-type TCOs are the most efficient and the most common are In_2O_3, SnO_2 and ZnO. Regarding the p-type TCOs, these ones have first been discovered in 1997 with $CuAlO_2$ [16]. Nevertheless, their electrical and optical properties are quite poor compare to n-type TCOs. In Figure 1.2a, several p-type and n-type semiconductors are presented in order to highlight the range of order of magnitude of the TCOs's electrical and optical properties [17].

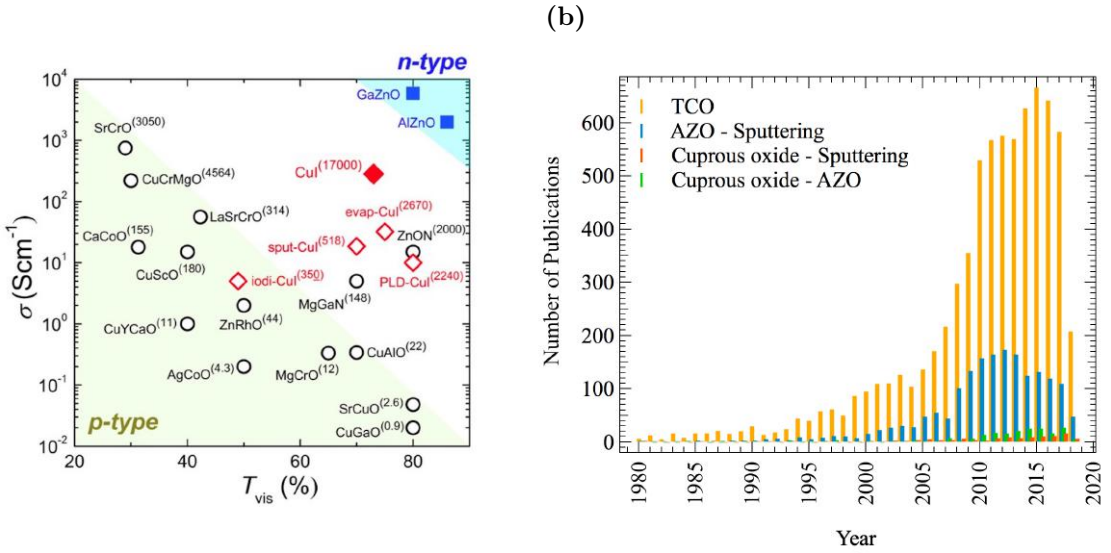

Fig. 1.2: (a) Visible wavelength range transmittance and electric conductivity cartography of p- and n-type TCOs [17]. (b) Number of publications as a function of the time determined using Scopus database.

In this work Aluminium-doped Zinc Oxide (AZO) is used as n-type TCO and magnesium-doped cuprous oxide Cu_2O:Mg is used as p-type TCO. As presented in Fig. 1.2b, the number of publications regarding TCOs drastically increase since the early 2000's due to their applicability in TEDs. Regarding the AZO, this n-type TCO is widely used thanks to its high transmittance in the visible wavelength range and its high charge carrier concentration when doped ($\sim 10^{21}$ cm^{-3}). The p-type TCO used in this work has not been deeply investigated. Nevertheless, a former doctoral thesis realised by Avelas

[18] in the SPIN research group gives promising results regarding this materials. In addition, as presented in Fig. 1.2b, the combinations of these two materials have not been deeply investigated giving an added value to this experimental investigation. Nowadays, the application fields of these TEDs spread from transparent thin film transistors, UV detectors, flexible organic LED displays, transparent solar panels, [19] to transparent electroluminescent devices [20]. This last application is the one envisioned in this work. In addition to the transparency, this kind of opto-electronic devices show several advantages like, flexibility, low power consumption and light weight [21].

The purpose of this thesis is to elaborate a transparent PN-junction which consists in a magnesium-doped cuprous oxide (Cu_2O:Mg) layer stacked with an AZO (ZnO:Al) layer. These p-doped (Cu_2O:Mg) and n-doped (ZnO:Al) semiconducting oxides are produced using a thin film deposition technique. A thorough and independent optimisation of the deposition parameters will be performed for both ZnO:Al and Cu_2O:Mg layers. **The main goal of this deposition parameter optimisation is the achievement of an efficient rectifying PN-junction**. A low electrical resistivity and a high transmittance in the visible wavelength range for both Cu_2O:Mg and ZnO:Al independent layers are also required.The optimisation process also includes an important optical, electrical, morphological and structural characterisation of the independent layers and of the device manufactured.

In addition to the experimental study, a one-dimensional numerical simulation of the PN-junction is performed using the numerical semiconductor solver code available in the SPIN research group [22]. Numerical simulations inputs are selected based on the experimental parameters and on the literature content. **The motivation behind these numerical simulations is to provide a clear description of the physical quantities related to the specific heterojunctions studied and to corroborate the predictions of the PN-junction theory**. Comparison between experimental and numerical results will also be performed to highlight the imperfections brought by the experimental fabrication and characterisation of the PN-junction.

This final thesis will be presented as followed. First, the theoretical background (cfr. Chapter 2) related to the semiconductor thin films gives the basis required to study the PN-junction and to understand the physics behind the electroluminescence phenomenon. This knowledge provides the reader a good insight of the physics of the LEDs studied in this work. The theoretical part is completed with a description of the thin film growth (cfr. Chapter 3), a description of the deposition process and finally a presentation of the state-of-the-art of Cu_2O:Mg and ZnO:Al semiconductors. Then the next chapter aims the description of the experimental processes (cfr. Chapter 4) used for the characterisation of the independent layers and of the heterostructure. The presentation and the interpretation of the results begin with the numerical simulations of the PN-junction (cfr. Chapter 5). In this chapter, the semiconductor equations to be solved are presented, the numerical resolution is described and the numerical results are presented and interpreted. Finally, the heterostructure fabrication is performed based on the optimisation of the deposition parameters and the characterisation results are presented, interpreted and discussed (cfr. Chapter 6). The main results are then summarised in a final chapter in order to provide a self-assessment of the work that can be related to the initial objectives, as well as an outlook of possible extensions of this project (cfr. Chapter 7).

Chapter 2

Theoretical Background

The purpose of this chapter is to provide the reader the physical knowledge required to understand the electroluminescence principle which is the physical concept responsible of the light emission in LEDs. In order to do so, the physics of semiconductor is presented with a particular attention on radiative and non-radiative recombinations occurring within the semiconducting material. The second section is dedicated to the explanation of the PN-junction and the advantages of this configuration compare to unique semiconducting material light emission are highlighted. The final section is dedicated to LEDs, the description of their efficiencies, as well as their applications in the framework of this thesis as light source in TEDs.

Main results and concepts presented and explained in this chapter:

- Recombinations of Electron-Hole Pairs (EHPs) are controlled by minority charge carriers in doped semiconducting materials. Two types of recombinations occur in the semiconductors: (i) radiative recombinations with no momentum change and for which energy conservation is managed through photon emission and (ii) non-radiative recombinations for which energy and momentum conservation occur through lattice vibrations and phonon emission. Schockley-Read-Hall (SRH) non-radiative recombinations occur via trap levels within the band gap and Auger non-radiative recombinations involve the excitation of an electron (resp. hole) in the conduction band (resp. valence band) (cfr. Section 2.1).
- Using a PN-junction heterostructure allows the increase of the minority carrier concentrations at the interface between both semiconductor thanks to a confinement effect. The recombination rate is proportional to this concentration, which involves more recombinations and a higher global efficiency η [%] of the LED, compared to semiconducting materials alone or PN-junction homostructure (cfr. Section 2.2).
- At a macroscopic scale, the external efficiency η_{ext} [%] of the LED also depends on the number of photons which goes out of the device, the extraction efficiency ξ_{ex} [%]. Therefore, a good transmittance $\mathcal{T}$ [%] in the emission spectrum of the semiconducting material is required. In this thesis, the LEDs studied aim the field of electronic in transparent displays like smart screen (cfr. Section 2.3).

2.1 Semiconductor

2.1.1 Electrons and energy bands

In quantum mechanic, discrete energy levels are allowed for electrons in the case of an **isolated atom** [23, 24][1]. These energy levels come from the resolution of the Schrödinger equation for an independent electron in motion in a Coulombic potential generated by the nucleus and by the other electrons. This is a complex problem involving many interacting particles which requires approximations in order to be solved. Electrons have a spin of 1/2, they are fermionic particles which obey Fermi-Dirac statistics. The distribution function given by Eq.(2.1) is shown in Fig. 2.1. By consequence, they have to respect Pauli's exclusion principle which states that two electrons in a given interacting system cannot be in the same quantum state. In statistical physics, the Fermi energy E_{F} [eV] represents the energy beyond which the probability to find an electron at 0 K is zero. However, in semiconductor physics, the Fermi level E_{F} does not refer to the Fermi energy even if it has the same notation but to the chemical potential μ_{F} [eV mol^{-1}].

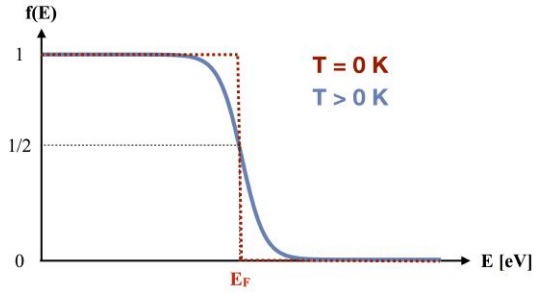

Fig. 2.1: Fermi-Dirac distribution at T=0K and T>0K. Direct consequence of the fermionic behaviour of the electrons. This distribution can be interpreted as the probability to find an electron at a specific energy.

$$f(E) = \frac{1}{1 + \exp\left[\frac{E - E_{\mathrm{F}}}{k_B T}\right]} \tag{2.1}$$

In a **solid material**, atoms bind with each other in order to form, at a larger scale, an amorphous, a crystalline or a polycrystalline structure. There are different types of bondings regarding the nature of the interaction between atoms. Ionic, covalent or metallic bondings respectively induce an exchange of the electronic density between atoms, a sharing of the electronic density between atoms or a pooling of the electronic density to the whole lattice. These bonds lead to the cohesion of the material balancing interatomic Coulombic repulsive forces. The balance between these repulsive and attractive forces induces a proper interatomic spacing. In order to form the solid state structure, a thought experiment can be made in which atoms are gathered from an infinite distance until the interatomic spacing distance is reached. In this configuration, energy levels of isolated atoms split into new energy levels out of respect for the Pauli principle. As the distance between the atoms is reduced, the Pauli principle which can be imagine as a repulsive interaction between electrons prevent two electrons to be in the same quantum states by shifting the energy levels of other atoms. Consequently, for N atoms, there will be a splitting in N energy levels and each one can be occupied by two electrons, one spin up and one spin down. This energy splitting leads to the formation of continuous energy

[1] Cfr. Streetman reference [23]: Chapter 1: "Crystal properties and growth of semiconductors".

bands. as shown in Fig. 2.2, the valence band represents the last occupied band with the highest energy and the conduction band is the band above the valence band which states are either empty of partially filled. The bottom of the conduction band is defined as the conduction band energy E_C [eV] and the upper edge of the valence band is defined as the valence band energy E_V [eV]. In the reciprocal space (momentum $\mathbf{k}$ space), the energy of an electron in the conduction band and a hole in the valence band are respectively given by:

$$E(\mathbf{k}) = E_C + \frac{\hbar^2 k^2}{2m_e^\star} \qquad (2.2) \qquad \text{and} \qquad E(\mathbf{k}) = E_V - \frac{\hbar^2 k^2}{2m_h^\star}, \qquad (2.3)$$

where the effective masses of the charge carriers $m_h^\star$ [kg] and $m_e^\star$ [kg] are related to the curvature of the energy in the reciprocal space $\mathbf{k}$. They represent inertia of electrons and holes at a specific momentum value in the solid structure lattice.

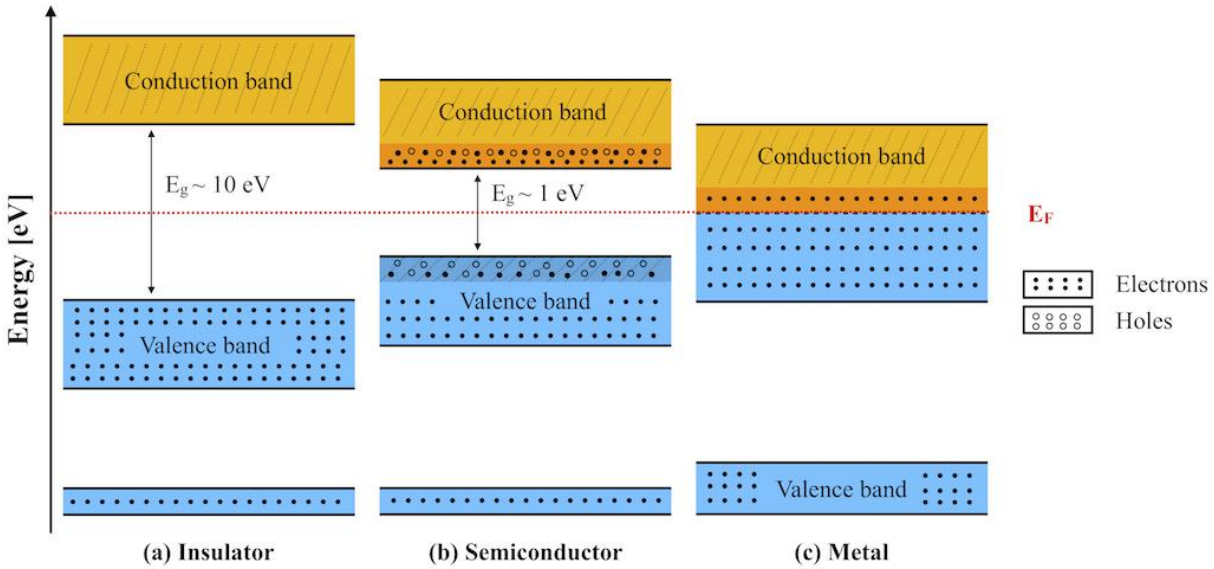

Fig. 2.2: Schematic representation of the band structure at non-zero temperature respectively for: (a) an insulator with a large band gap prohibiting electron excitations. (b) a semiconducting material with a band gap energy of the order of 1 eV in which electrons can be thermally excited from the valence band to the states available at higher energies in the conduction band, leaving electron vacancies in the valence band *i. e.* holes. (c) A metallic material where the Fermi level is within the conduction band allowing any thermal excitations of charge carriers participating to the whole lattice electrical conductivity.

Figure 2.2 shows that energy bands are separated by a region without electronic states called the band gap with an energy width E_g [eV]. In insulating materials, the Fermi level is located within the band gap and the valence band is completely filled while the conduction band is empty. In opposition, in a metal, the Fermi level is located in an available band which by definition is the conduction band. Consequently, electrons in the conduction band below E_F can be easily thermally excited above E_F to contribute to the whole lattice conductivity by becoming free charge carriers. The large energy band gap $E_g \simeq 10\ eV$ in an insulator prevents any moderate thermal excitation. However, for semiconducting material on which we focus in this thesis, the order of magnitude of E_g is 1 eV. Electrons in the valence band can therefore be thermally excited in the conduction band leaving electron vacancies called holes in the valence band. Electrons (resp. holes)

in the conduction band (resp. valance band) are free charge carriers which participate to the whole lattice conductivity. This band gap energy is a function of the stoichiometry of the material and of the interatomic spacing.

In the following part of this section, the distinction between intrinsic and extrinsic semiconducting materials is presented.

2.1.2 Intrinsic and Extrinsic Semiconductor Materials

A semiconductor with no intentionnaly added impurity nor native defect is called an **intrinsic semiconductor**. At 0 K, the valence band is completely filled with electrons, which does not have the thermal energy input required to cross the band gap and reach available electronic states into the conduction band leaving a hole in the valence band. While at higher temperature, as it is presented in Fig. 2.2, Electron-Hole Pair (EHP) are generated at a temperature-dependent rate $G_0(T)$. In a steady state intrinsic semiconductor, the generation rate $G_0(T)$ is equal to the recombination rate $R_0(T)$. The EHP generation and recombination mechanisms involve that the electron concentration n_0 is equal to the hole concentration p_0 which are both equal to the intrinsic carrier concentration ${n_i}^2$ (cfr. Eq.(2.4)). Indeed each excited electron leaves a hole in the valence band. The index 0 means that the concentration is the carrier concentration under thermodynamic equilibrium. These concentrations can also be linked to the intrinsic concentration through the law of mass action presented in Eq.(2.5). This one can be found by considering the Fermi level in the middle of the band gap like it is the case for intrinsic semiconductor [23][3]. In this particular case, the Fermi level is also called the intrinsic energy level E_{I} [eV].

$$n_i = n_0 = p_0 \qquad (2.4) \qquad \text{and} \qquad n_i^2 = n_0 p_0 \qquad (2.5)$$

The n-type carrier concentration can be expressed as the integration of the product of the density of states available[4] N(E) times the Fermi-Dirac distribution f(E) over the conduction band. Furthermore, the Fermi-Dirac distribution can be approximated by the Maxwell-Boltzmann (MB) distribution if we consider $k_B T \ll E - E_{\mathrm{F}}$. This is the case at room temperature where $k_B T = 0.026$ eV (cfr. Eq.(2.6)).

$$f(E) \;=\; \frac{1}{1+\exp\left[\frac{E-E_{\mathrm{F}}}{k_B T}\right]} \;\overset{\mathrm{MB}}{\approx}\; \exp\left[\frac{-(E-E_{\mathrm{F}})}{k_B T}\right] \qquad (2.6)$$

The resulting expressions of the carrier concentration which are valid for both extrinsic and intrinsic semiconductors are respectively given for the n-type carriers by Eq.(2.7) and for the p-type carriers by Eq.(2.8) as shown in the schematic representation in Fig. 2.3.

[2]For instance, the intrinsic carrier concentration in silicon semiconductor at room temperature is about 10^{10} cm^{-3}.

[3]Cfr. Streetman reference [23]: Chapter 3: "Energy bands and charge carriers in semiconductors".

[4]The theoretical demonstration of the Density Of States (DOS) as a function of the energy is not presented here but can be found in [23] Chapter 3: "Energy bands and charge carriers in semiconductors".

$$n_0 = \int_{E_C}^{\infty} f(E)\ N(E)\ dE \overset{\text{MB}}{\approx} N_c\ e^{-(E_C - E_F)/k_B T} \text{ with } N_c = 2\left(\frac{2\pi m_n^\star k_B T}{h^2}\right)^{\frac{3}{2}} \tag{2.7}$$

$$p_0 = \int_{0}^{E_V} (1 - f(E))\ N(E)\ dE \overset{\text{MB}}{\approx} N_v\ e^{-(E_F - E_V)/k_B T} \text{ with } N_v = 2\left(\frac{2\pi m_p^\star k_B T}{h^2}\right)^{\frac{3}{2}} \tag{2.8}$$

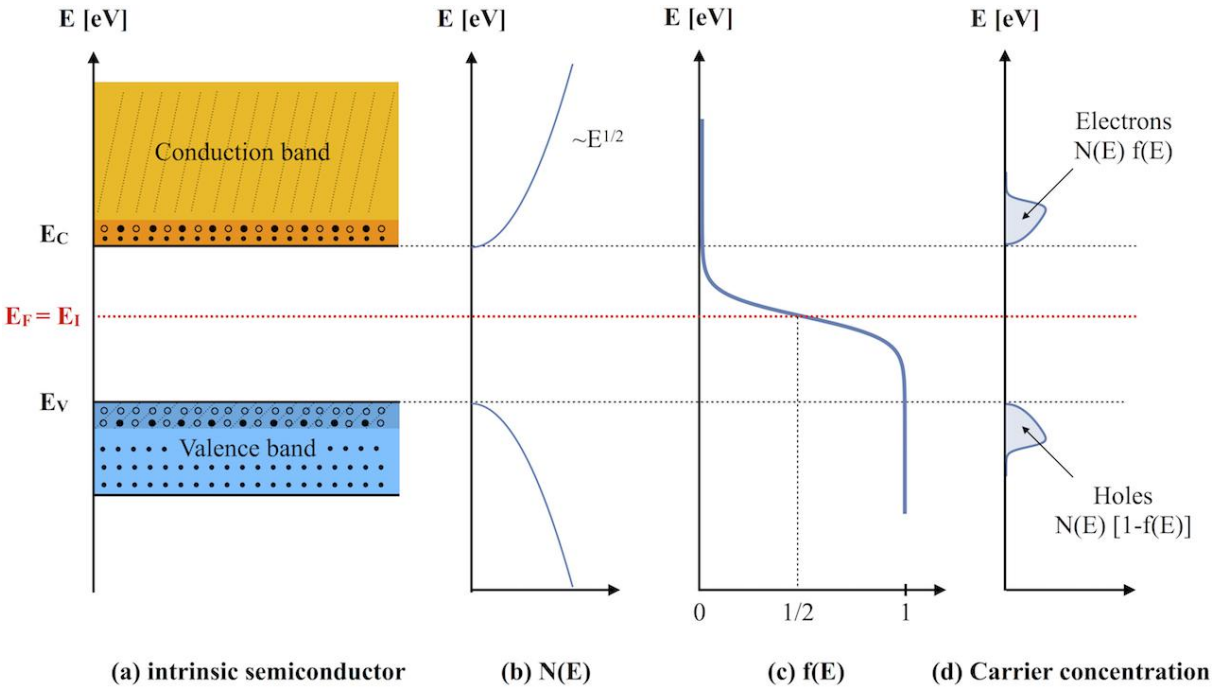

Fig. 2.3: Schematic band diagram representation. (a) The density of states which comes from the quantum mechanic resolution of the system. This one is proportional to the square root of the energy. (b) The Fermi-Dirac distribution (cfr. Eq.(2.1)). (c) The carriers concentrations for a n-type semiconductor.

These concentrations can also be linked to the intrinsic concentration (cfr. Eq.(2.9)) through the law of mass action (cfr. Eq.(2.5)).

$$n_i = \sqrt{N_c N_v}\ e^{-E_g/2k_B T} \tag{2.9}$$

In addition, semiconductor materials can be doped in order to increase the number of electrons or holes as charge carriers and consequently to increase the material conductivity. For an **extrinsic semiconductor**, the doping is performed by adding specific impurities into the crystal lattice. This doping allows one to tune the semiconductor conductivity by increasing the electron concentration (resp. hole concentration). In this case we talk about n-doped semiconductor (resp. p-doped semiconductor) as shown in the schematic

representation in Fig. 2.4. Group IV elements from Mendeleïev's periodic table like silicon are usually doped with group V (resp. group III) elements like phosphor (resp. like boron) in order to achieve a n-doped (resp. p-doped) semiconductor. In a n-type (resp. p-type) semiconducting material, the carrier concentration under equilibrium conditions n_0 (resp. p_0) is consequently different from the intrinsic carriers concentration n_i. This doping introduces additional electron (resp. hole) energy levels called donor levels with a concentration N_{D}^{+} [cm^{-3}] (resp. acceptor levels with a concentration N_{A}^{-} [cm^{-3}]) within the band gap and close to E_{C} (resp. E_{V}). At 0 K, these levels are filled with carriers and these ones can be easily thermally excited to improve the carriers concentration in the conduction band (resp. valence band) as shown in Fig. 2.4b and 2.4d. Consequently, doping is a direct way to tune the conductivity of the materials. The doping also influence the position of the Fermi level which is shifted compare to E_I regarding the doping concentration according to Eq.(2.7) and (2.8). Note that for a excessive doping, Fermi-level shift is too important and the previous MB assumption regarding the Fermi-Dirac distribution (cfr. Eq.(2.6)) is no more valid. In this particular case we talk about degenerate semiconductors for which the previous established relations are no more valid.

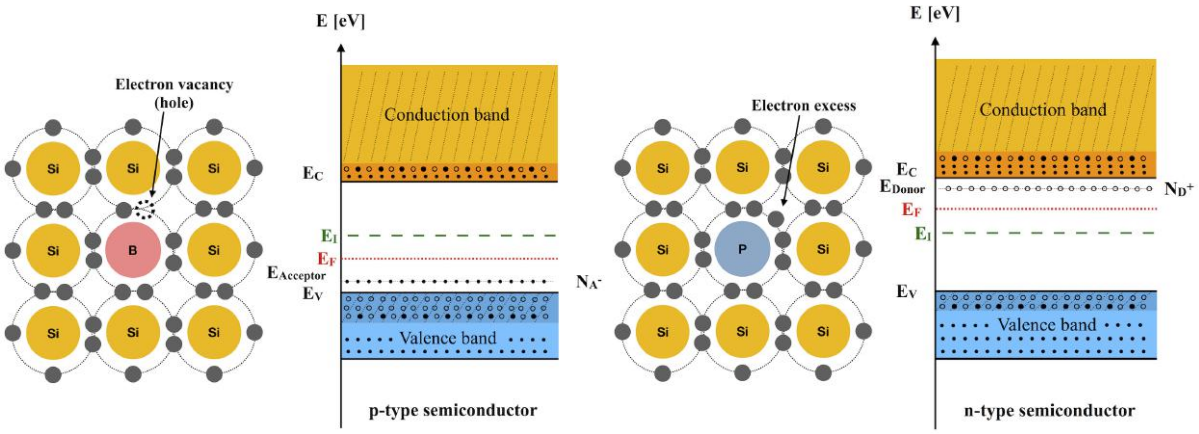

(a) p-doped semiconductor

(b) p-doped semiconductor band diagram

(c) n-doped semiconductor

(d) p-doped semiconductor band diagram

Fig. 2.4: Extrinsic semiconductors, illustrations of the making of example of silicon. (a) p-doped semiconductor, one silicon atom has been substituted by a boron atom with a lack of one valence electron compare to Si atom. Thermally excited electrons fill these vacancies and contribute to the increase of the hole concentration p in the valance band. (b) p-type semiconductor band diagram with a Fermi level shifted towards the valence band (c) n-semiconductor, one silicon atom has been substituted by a phosphor atom with one added valence electron which can be easily thermally excited to contribute to the electron concentration in the conduction band n. (d) n-type semiconductor band diagram with a Fermi level shifted towards the conduction band.

In a n-doped semiconductor electrons are the majority carriers and holes the minority carriers ($n_0 \gg p_0$) and inversely in a p-doped material. The carrier concentrations are given by Eq.(2.10) for n-doped semiconductor (resp. Eq.(2.11) for p-doped semiconductor). Indeed, the majority carrier concentration is dominated by the concentration of dopants and the minority carriers concentration are determined via the law of mass action

given by Eq.(2.5):

$$n_0 = N_{\mathrm{D}}^{+} \qquad and \qquad p_0 = \frac{n_i^2}{N_{\mathrm{D}}^{+}} \tag{2.10}$$

$$p_0 = N_{\mathrm{A}}^{-} \qquad and \qquad n_0 = \frac{n_i^2}{N_{\mathrm{A}}^{-}} \tag{2.11}$$

In a next chapter, the concept of electrical resistivity ρ [Ωm] is used to characterise electrically the layers and the structure determined. The resistivity can be defined as a physical property which allows one to quantify how a material is reticent to the flow of a charge carriers (electrons, holes, ions) inside this material. Equations (2.12) and (2.13) give respectively the resistivity for electron and hole motions which are related to the charge carrier concentrations and a total scattering rate. The phenomena which account for the electrical resistivity of the material are charge carrier scatterings. Indeed in a crystal, charge carriers like electrons for instance experienced inelastic scatterings with phonons, other electrons and lattice's impurities or defects. The Matthiessen rule (cfr. Eq.(2.14)) shows that the temperature-dependent scattering rates can be cumulated in order to acquire the total scattering rate.

$$\rho_n = \frac{m_e}{nq}\tau^{-1} \tag{2.12}$$ and $$\rho_p = \frac{m_h}{pq}\tau^{-1} \tag{2.13}$$

$$\tau^{-1}(T) = \tau_{\mathrm{el-imp}}^{-1} + \tau_{\mathrm{el-pho}}^{-1}(T) + \tau_{\mathrm{el-el}}^{-1}(T) \tag{2.14}$$

The next part of this section is dedicated to the presentation and the description of the electroluminescence phenomenon occurring in semiconducting materials.

2.1.3 Electron-Hole Pair Radiative and Non-Radiative Recombinations

In this part, we will focus on **excess carriers** in semiconductors. Excess carriers can be created in a semiconductor medium by optical absorption, electron bombardment or as it will be explained in the second section of this chapter by injected charge carriers. As we will see, this excess of charge plays a fundamental role in the electroluminescence mechanism. The injection of an excess in charge carriers induces the breaking down of the thermodynamic equilibrium conditions.

During the recombination of excess carriers, light can be emitted by the material in order to conserve the total energy. The property of light emission is called luminescence. Different processes of luminescence occur depending on the the mechanism of creation of excess of charge carriers excess. Carriers of both types can be initially created by photons (photoluminescence), by high-energy electron bombardment (cathodoluminescence) or by injecting a current into the material (**electroluminescence**) [23][5]. Two different types of recombinations between holes and electrons can occur depending on the semiconductor properties. The first type is the radiative recombination which results in the emission of photons. The second type is the non-radiative recombinations where the energy is lost by scattering with the lattice. This scattering induces lattice vibrations in the form of

[5]Cfr. Streetman reference [23]: Chapter 4:"Excess carriers in semiconductors".

phonons which are quanta of energy related to ionic vibrations in a solid. In light emitting devices the first process is obviously favoured. Nevertheless, as it will be explained, non-radiative recombinations cannot be reduced to zero.

Equation (2.5) tells us that in a semiconductor at a given temperature, the product of the concentration of charge carriers is a constant equals to the intrinsic concentration. Due to an injection of current, excess electron concentration Δn or excess of hole concentration Δp are generated in the semiconductor in addition to the thermodynamic equilibrium charge carrier concentrations n_0 and p_0 seen in the previous section. Furthermore, depending on the excitation level, the current injected in the material is considered as a low-level excitation if the concentration excess of carriers generated is much smaller than the majority carrier concentration $\Delta n \ll n_0$ (this case for a n-type semiconductor). Electrons and holes are generated in pairs which implies that $\Delta n = \Delta p$ in the steady-state regime. However depending on the doping of the semiconductor, the ratio of the excess concentrations and equilibrium thermodynamic concentrations between holes and electrons are not equal:

$$\frac{\Delta p}{p_0} \gg \frac{\Delta n}{n_0} \qquad \text{for a n-type semiconductor} \tag{2.15}$$

$$\frac{\Delta n}{n_0} \gg \frac{\Delta p}{p_0} \qquad \text{for a p-type semiconductor} \tag{2.16}$$

Due to recombinations theses excess concentrations are time-dependent. The total carrier concentrations are then given respectively for electrons and holes by:

$$n(t) = n_0 + \Delta n(t) \tag{2.17}$$ and $$p(t) = p_0 + \Delta p(t) \tag{2.18}$$

The excess concentrations of carriers evolve with time in order to come back to the thermal equilibrium state. This rate is given by the Eq.(2.19) which is the bimolecular rate equation [4][6].

$$R = B[n_0 + \Delta n(t)][p_0 + \Delta p(t)] \tag{2.19}$$

$$R = Bn_i^2 + B[n_0 + p_0]\Delta n(t) = R_0 + R_{\text{excess}} \tag{2.20}$$

Equation (2.20) is obtained from Eq.(2.19) by considering a low-level excitation $\Delta n \ll n_0$ (for n-type semiconductor) and the pair generation conditions $\Delta n = \Delta p$. In this equation, R_0 represents the recombination rate under thermal equilibrium conditions. Indeed, at a temperature T, a dynamic equilibrium takes place in the semiconductor. EHP are generated with a rate $G_0(T)$ [m^{-3} s^{-1}] and they recombine with a rate $R_0(T)$ [m^{-3} s^{-1}] equals to the generation rate. Out of thermodynamic conditions, the excess of charge carriers injected in the semiconductor produce a recombination rate excess R_{excess} in order to go back to thermodynamic equilibrium. If a low-level current is injected in the material and switched off at $t = t_0$, the recombination rate can be calculated using Eq.(2.21).

[6] Cfr. Schubert reference [4]: Chapter 2:"Radiative and non-radiative recombination".

$$\frac{d}{dt}\Delta n(t) = -B[n_0 + p_0]\Delta n(t) \tag{2.21}$$

$$\Leftrightarrow \Delta n(t) = \Delta n(0)\ e^{\frac{-t}{\tau}} \qquad with \qquad \tau = \frac{1}{B(n_0 + p_0)} \tag{2.22}$$

The characteristic time τ represents the average time before an EHP undergoes recombination. By using Eq.(2.15) and (2.16), a specific carrier lifetime is given for the minority carriers by Eq.(2.23) and (2.24) respectively for a p-type and n-type semiconductor.

$$\tau_n = \frac{1}{B\ p_0} = \frac{1}{B\ N_{\mathrm{A}}} \qquad \text{for a p-type semiconductor} \tag{2.23}$$

$$\tau_p = \frac{1}{B\ n_0} = \frac{1}{B\ N_{\mathrm{D}}} \qquad \text{for a n-type semiconductor} \tag{2.24}$$

These carriers lifetimes corresponds to the average time between the generation and the recombination of minority carriers. Majority carriers concentrations also decay with a life time τ but a small amount of majority charge carriers undergoes recombination compare to the minority carriers. Thus for low-level excitation the majority carrier lifetime is much higher than the minority carrier lifetimes [7]. In practice this majority carrier lifetime can be assumed to be infinite. With a high-level excitation the time constant depends on time but this particular case is not tackled here. The luminescence $\mathcal{I}$ [cd] is proportional to the recombination rate (cfr. Eq.(2.25) for low-level excitation) calculated from Eq.(2.22).

$$\mathcal{I} \propto R = -\frac{dn(t)}{dt} = \frac{\Delta n(0)}{\tau}\ e^{\frac{t}{\tau}} \tag{2.25}$$

and

$$E = h\nu \tag{2.26}$$

The theoretical emission spectrum determined (cfr. Fig. 2.5) is temperature-dependent. Indeed, EHP recombination does not occur only at photon energy equals to E_g. The photons energy is also related to the electromagnetic wave frequency through Eq.(2.26). Different energy resulting in different frequencies as it can presented in Fig. 2.5. Electrons are thermally excited and the resulting kinetic energy of these ones in the conduction band depend on the temperature of the system. As shown in Fig. 2.5, the emission spectrum resulting of EHP **radiative recombinations** is limited by the DOS between E_{g} and $E_{\mathrm{g}} + k_B T/2$. The highest energy level that can be accessed in the conduction band depends on the thermal energy available. Indeed, above $E_{\mathrm{g}} + k_B T/2$, the MB distribution which comes from the assumption made in Eq.(2.6) limits the intensity of the emission spectrum. The thermal energy input provided by the temperature is not sufficient to access higher energy levels even if these ones are available [4][8].

[7] With a p-doped GaAs ($\mathrm{N}_A = 10^{18}$ cm^{-3}), using B = 10^{-10} cm^3/s, $\tau_n = 0.01\mu s$ and $\tau = 2500s$ with undoped GaAs.

[8] Cfr. Schubert reference [4]: Chapter 5: "LEDs basics: optical properties".

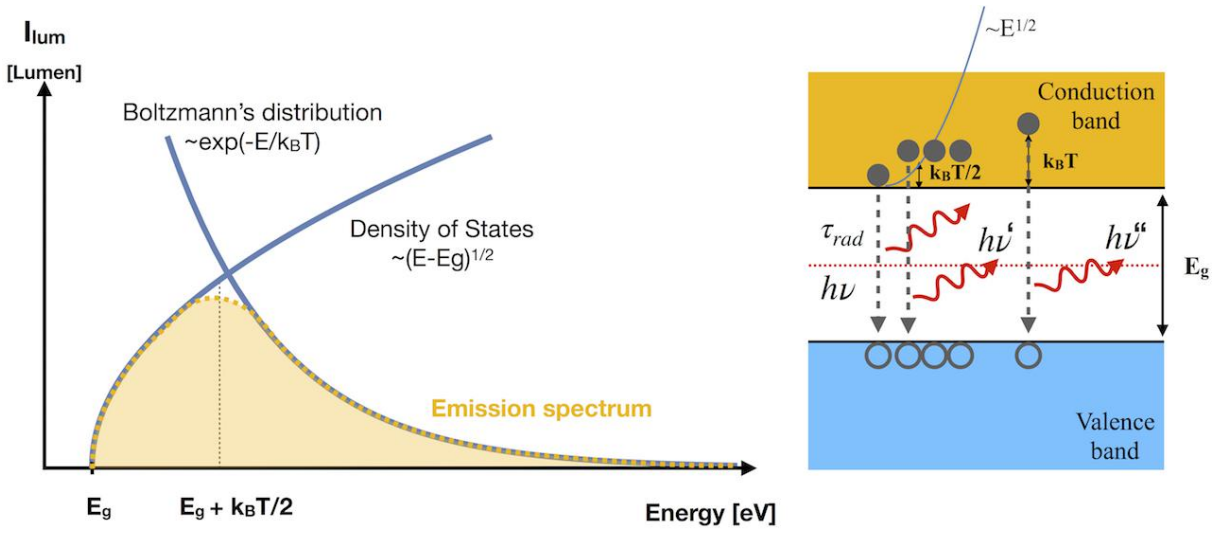

Fig. 2.5: Theoretical emission spectrum. Two limiting factors are present. First, the DOS available which behaves as the square root of the energy and consequently is more important at energy higher than E_g. And the second one is the MB distribution which dictates the energy distribution of the EHP and limit the luminous intensity for energy higher than E_g+$k_BT/2$. The EHP radiative recombination rate depends on the average time between the generation and the recombination τ_{rad}.

Undesired **non-radiative recombinations** also occur in the semiconductor materials. In opposition to radiative recombinations which, lead to the emission of a photon with an energy equals to the band gap energy E_g, non-radiative recombination processes convert the charge carrier energy into vibrational energy of the lattice. The electron energy is thus converted into a phonon whose energy is lost in the form of heat. As shown in Fig. 2.6, two main processes are responsible for the non-radiative recombinations: Schockley-Read-Hall (SRH) recombinations and Auger recombinations.

First, SRH non-radiative recombination processes occur due to the presence of defects in the crystal lattice. These defects are associated to the presence of additional energy levels E_T. Some of them are located within the band gap of the semiconductor. The additional energy levels (called trap states) are efficient recombination centres, in particular if they are located close to the middle of the band gap. This SRH type of recombination was first studied in 1952 by Hall, Shockley and Read [25, 26]. This recombination rate depends on the energy E_T and the concentration N_T of the traps. The process is limited by the minority carriers recombination rate and is temperature-dependent [4][9]. The second type of non-radiative recombination is Auger recombination. In these processes, the electron-hole energy recombination is transferred to a free charge carrier. The excited electron (resp. hole) with high energy in the conduction (resp. valence) band will ultimately loses its energy by phonon emissions and subsequently come back close to the band edge. The Auger recombination rate is proportional to the square of the carrier concentration since two carriers of the same type are involved in this mechanism. Consequently, Auger recombinations occur at high injection current densities or in confined structure. Furthermore in thin films, non-radiative recombination at the surface are also frequent. Indeed, surface or interfaces act like a perturbation in the crystal periodicity.

[9]Cfr. Schubert reference [4]: Chapter 2: "Radiative and non-radiative recombination".

This periodicity perturbation induces additional energy levels within the band gap. This effect involves the reduction of the luminescence and the heating of the surface due to phonon emissions.

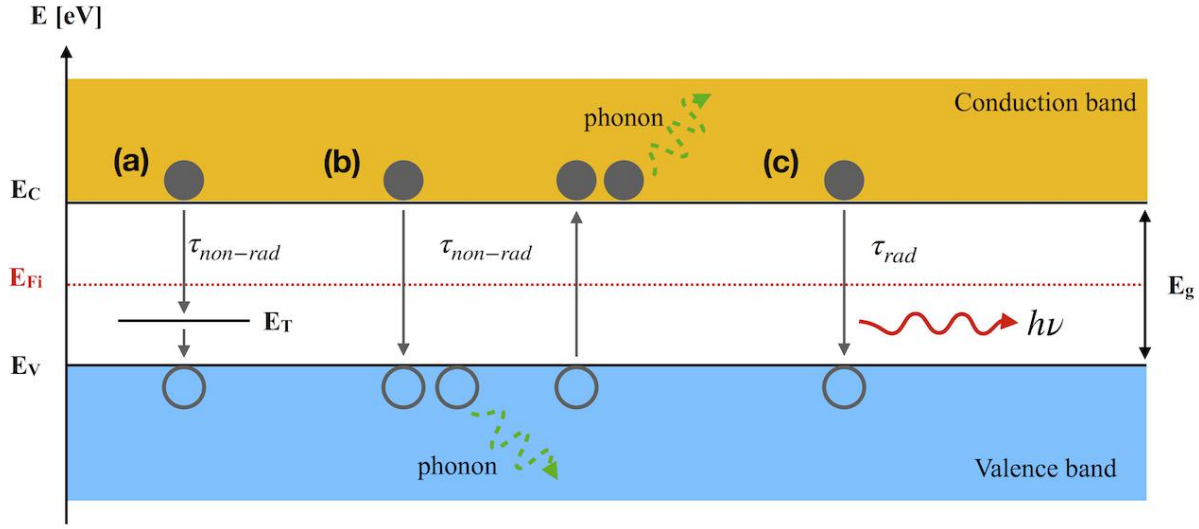

Fig. 2.6: Band diagram representation. Different recombination processes including (a) SRH recombinations of an EHP through a trap level state within the band gap. This type of recombination depends on the minority carrier concentration and also on the trap levels concentration. The conservation of energy is fulfilled through the emission of a phonon. (b) Auger recombinations occur at high carrier concentration. The EHP recombination energy is used to excite an electron which through scattering events induces the emission of phonons before getting back to an thermodynamic equilibrium state. (c) Radiative recombinations of an EHP with energy conservation happens through the emission of a photon.

Finally, the total recombination probability will be given by the sum of the radiative recombination and the non-radiative recombination probabilities which are directly related to the carriers life times in the different recombination processes (cfr. Eq.(2.27)).

$$\tau^{-1} = \tau_{\text{rad}}^{-1} + \tau_{\text{non-rad}}^{-1} \tag{2.27}$$

The ratio between the number EHP undergoing radiative recombinations and the total number of recombinations (cfr. Eq.(2.28)) is called the internal quantum efficiency η_{int} [%].

$$\eta_{\text{int}} = \frac{\tau_{\text{rad}}^{-1}}{\tau_{\text{rad}}^{-1} + \tau_{\text{non-rad}}^{-1}} \tag{2.28}$$

In **indirect band gap semiconductors**, the bottom of the conduction band is not located at the same momentum value than the top of the valence band. In this type of semiconductor, trap levels can be used to achieve radiative recombinations. This kind of radiative recombination is associated with the absorption or the emission of a phonon which ensures the conservation of the momentum. Furthermore, since the number of

phonons increases with the temperature, the occurrence of these radiative recombination also increases.

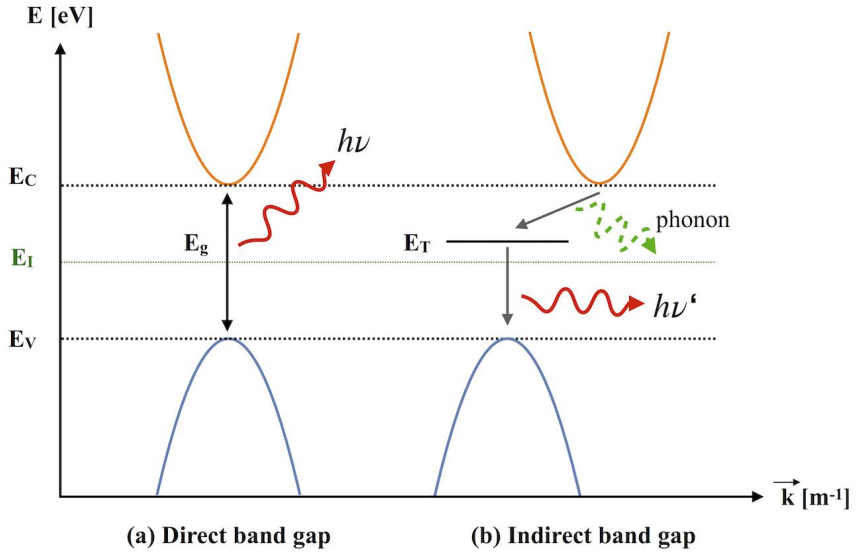

Fig. 2.7: Schematic representation of radiative recombination occurring in a direct (a) and an indirect band (b) gap semiconductor. In an indirect band gap semiconductor, the recombination is assisted by phonon emission in order to preserve the momentum conservation.

The recombination dynamic of minority carrier is one of the parameter that limits the efficiency of LED. In order to decrease the minority carriers life time, heterostructures are used to confine the excess charge carriers in a spatial region in order to increase the concentration. As the number of recombination increases, the number of photons emitted also increases. A more complete explanation of this phenomenon will be the purpose of the second section of this chapter.

2.2 PN-Junctions

2.2.1 Homojunctions Under Thermodynamic Equilibrium Conditions

In order to understand the recombination processes occurring at the junction between a p-doped semiconductor and a n-doped semiconductor, the knowledge of the physics behind this **PN-junction under thermodynamic equilibrium conditions** is required [23][10]. To begin, the case of homojunctions is first addressed. This kind of junction consists of an interface between two identical semiconducting materials doped differently. These ones have the same band gap energy but exhibit typically different types of doping.

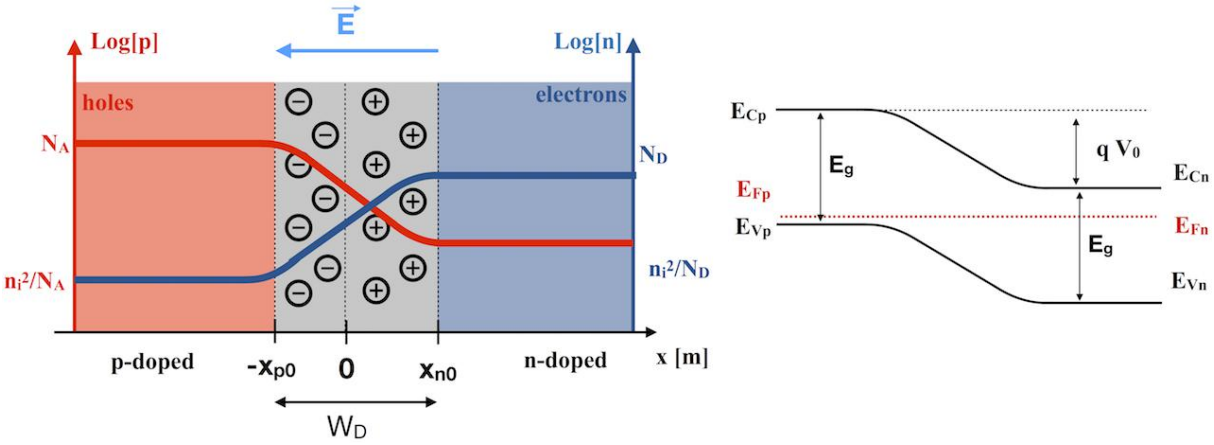

Fig. 2.8: Schematic representation of the PN-junction and the corresponding band structure under thermodynamic equilibrium conditions. In this representation the p-doped semiconductor is heavily-doped than the n-doped side. As consequence, the Fermi level on the p-side in closer to E_V than the Fermi level on the n-side to E_C. The bending in the band structure is induced by the alignment of the Fermi levels of each semiconductor leading to an energy barrier of height qV_0 between the n-side and the p-side.

As presented in Fig. 2.8, let's consider a p-doped semiconductor and a n-doped semiconductor which are brought together in order to from an interface between both. As explained in Section 2.1, the n-doped material has a large concentration of electrons and a low concentration of holes (cfr. Eq.(2.10) and (2.11)). When the junction is realised a gradient of concentration is established across the interface. In opposition to the p-doped material, the n-doped semiconductor has many electrons and few holes. Consequently, charge carriers diffusion occurs across the junction with current density relations given by Eq.(2.29) and (2.30). Electrons (resp. holes) diffuse from the n-side (resp. p-side) to the p-side (resp. n-side) with a diffusion coefficient given by D_n [m^2 s^{-1}] (resp. D_p).

$$J_{\text{diff},n}(x) = q\ D_n \frac{dn(x)}{dx} \qquad (2.29) \qquad \text{and} \qquad J_{\text{diff},p}(x) = -q\ D_p \frac{dp(x)}{dx} \qquad (2.30)$$

As shown in Fig. 2.9, diffused electrons (resp. holes) leave behind them ions charged positively N_D^+ (resp.N_A^-). As a result, in the vicinity of the interface, a negative space

[10]Cfr. Streetman reference [23]: Chapter 5: "Junctions".

charge is formed on the p-side and an positive one is created on the n-side resulting in the creation of en electric field $\mathbf{E}$ [V m^{-1}]. This one is related to the space derivative of the electric potential $\mathbf{E}= -\nabla V$. Then, the conversion from the space charge density ρ[11] to the electric field using the Poisson's equation (cfr. Eq(2.31)) which can be combined to the previous result:

$$\Delta V \;=\; \frac{-\rho}{\epsilon_0} \;= \nabla \cdot \mathbf{E} \tag{2.31}$$

As presented in Fig. 2.9c, V_0 [V] is the difference between the constant potential in the n-region V_n and the constant potential in the p-region V_p which is called the contact potential. The electric field is a non-zero value over a region W_d and is assumed to be zero in the neutral regions far from the interface as shown in Fig. 2.9b. The region of width W_d is called the depletion region in which a space charge due to uncompensated donor and acceptor ions is present. In Fig. 2.9a the assumption of full depletion is made regarding the charge carrier density. This approximation which gives rather good results consists in representing the charge carrier density variation as steps in contrast to the real exponential decay (in dashed line).

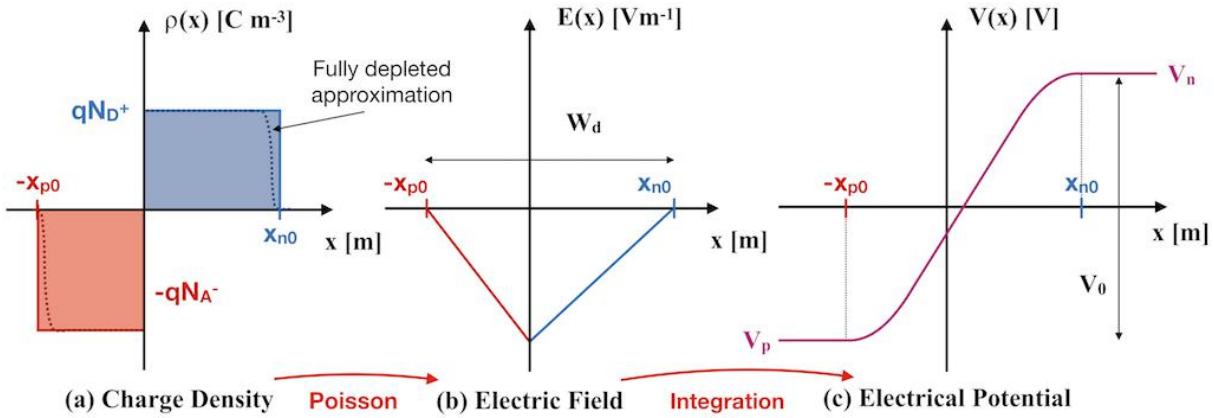

Fig. 2.9: (a) Charge density [C m^{-3}] in the fully depleted approximation. The charge density is assumed to be constant between in the depletion region and 0 in the neutral region. It is a good approximation of the exponential decay of the space charge density [23]. (b) The electric field [V m^{-1}] resulting from the integration of the charge density. (c) The electric potential [V] coming from $\mathbf{E}= -\nabla V$. All these quantities are presented over the depletion region W_d of a PN-junction under thermodynamic equilibrium conditions.

As shown in Fig. 2.8, this interface potential induces a bending of the valence band and conduction band in the band diagram over the depletion region. As result, an energy barrier, with height qV_0, is formed between the p-side and the n-side. This behaviour is a direct consequence of the Femi level alignment required at equilibrium. As a reminder, due to the doping gradient between both side of the junction the Fermi levels are not at the same position (cfr. Fig. 2.4). The depletion region width W_d is a function of the contact potential and the doping concentrations $(N_\mathrm{A}, N_\mathrm{D})$ (cfr. Eq.(2.32)) [23][12]. Indeed, the larger the doping concentration, the thinner the depletion region in the corresponding doping region. In consequence, in the schematic representation of Fig. 2.9, the n-doped

[11] In this Section 2.2, the notation ρ stands for the space charge density.
[12] Cfr. Streetman reference [23]: Chapter 5: "Junctions".

semiconductor as a depletion region W_d extending from $-x_{\mathrm{p}0}$ in the p-side and $x_{\mathrm{n}0}$ in the n-side. In Eq.(2.32), V_app corresponds to the bias applied on the junction. In the present part of the section, V_app is equal to 0, the case of a junction under applied bias is investigated in subsection 2.12.

$$W_\mathrm{d} = \sqrt{\frac{2\epsilon_0\epsilon_r}{q}\left(\frac{N_\mathrm{A}+N_\mathrm{D}}{N_\mathrm{A}N_\mathrm{D}}\right)(V_0 - V_\mathrm{app})} \tag{2.32}$$

The electric field induces a motion of carriers opposite to diffusion which is given respectively for n-carriers and p-carriers by Eq.(2.33) and (2.34).

$$J_{\mathrm{drift},n}(x) = -q\mu_n n(x)E(x) \tag{2.33}$$ and $$J_{\mathrm{drift},p}(x) = q\mu_p p(x)E(x) \tag{2.34}$$

Then, the charge carriers mobility μ_p for electrons and μ_p for holes in $[m^2V^{-1}s^{-1}]$ describe the charge carriers motion ease when these ones are subjected to an electric field. Indeed, the drift velocity of the carrier is related to the electric field via this physical quantity [27] (cfr. Eq.(2.35)). These ones are determined by the scattering with phonons, native defects and impurities (cfr. Eq (2.14)) and are related to the electrical resistivity through Eq.(2.36).

$$\mathbf{v}_\mathrm{drift} = \mu\mathbf{E} \tag{2.35}$$ and $$\mu = \frac{1}{qn\rho} \tag{2.36}$$

Under thermodynamic equilibrium, both electrons and holes currents have to be canceled. Indeed, the diffusion phenomenon implied as a result of the interface creation tends to increase the depletion region by inducing more space charge. In opposition, due to this space charge generation, the electric field generated is reenforced. As a consequence of the self-maintaining of these phenomena, the drift current resulting from this electric field in the depletion layer opposed and canceled the diffusive current. Consequently, the drift current densities and the diffusion current densities cancel each other (cfr. Eq.(2.37) and (2.38)) and a dynamic equilibrium is reached.

$$J_{\mathrm{drift},n}(x) + J_{\mathrm{diff},n}(x) = 0 \tag{2.37}$$ and $$J_{\mathrm{drift},p}(x) + J_{\mathrm{diff},p}(x) = 0 \tag{2.38}$$

Moreover, the ratio between the majority and minority carrier concentrations can be expressed as a function of the temperature and the contact potential (cfr. Eq.(2.39)) [23][13]. In this relation, the impact of charge carrier concentration on the electric potential at the interface of the PN-junction is highlighted.

$$p_p\ n_p = n_n\ p_n = n_i^2\ e^{qV_0/k_BT} \tag{2.39}$$

In this part, the behaviour of the PN-junctions under thermodynamic equilibrium conditions was studied. In the following part, the electroluminescence phenomenon is investigated through charge carriers injection into the PN-junction. In order to do so, an external voltage V_app [V] is applied onto the homojunction. As reference for the following reasonings, the p-side is considered as the mass and the n-side is biased by an external bias V_app.

[13]Cfr. Streetman reference [23]: Chapter 4: "Excess carriers in semiconductors".

2.2.2 Homojunctions Under Injected Current

For a **PN-junction out of thermodynamic equilibrium conditions**, for instance if an external voltage V_{app} is applied across the junction, the physical quantities which define the PN-junction such as the electric potential and the charge charge carrier concentrations will be impacted as a function of the position within the PN-jucntion [23][14]. This subsection aims the description of an homojunction under an external bias applied. The forward (resp. reverse) bias is defined for a negative (resp. positive) bias applied on the n-side of the junction.

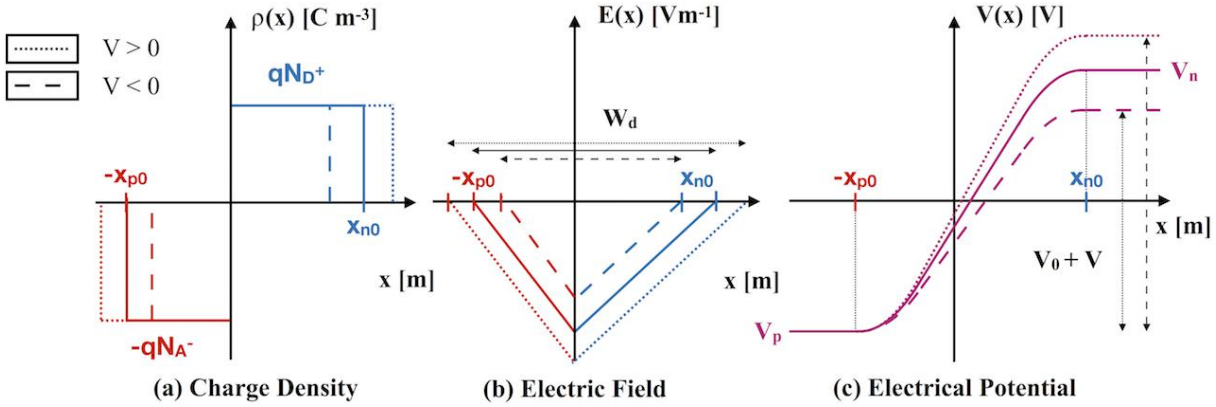

Fig. 2.10: (a) Charge density [C m^{-3}], (b) electric field [V m^{-1}] and (c) electric potential [V] over the depletion region W_{d} for a PN-junction under an external bias applied on the n-side. The p-side is set as the potential reference. A positive bias applied induces an increase of the potential barrier a decrease of the electric field due to a decrease of the total space charge density.

As shown in Fig. 2.10 for a forward (resp. reverse) bias applied the electrostatic potential at the interface is lowered (resp. increased). In consequence, the absolute value of the electric field in the depletion region decreases (resp. increases) for forward (resp. reverse) bias. As the electric field increases, the diffusion of charge carriers to the opposite doping region is reduced. Indeed, the electrons (resp. holes) approaching the interface are swept to the n-side (resp. p-side). As presented, the electric field is related to the space charge concentrations in the depletion region. The depletion region width W_{d} is directly impacted (cfr. Eq.(2.32)). Thus, the depletion region width decreases (resp. increases) under forward (resp. reverse) bias.

As presented in Fig. 2.8, under thermodynamic equilibrium conditions, the Fermi level of each doped semiconductor are aligned. Out of thermodynamic equilibrium conditions, quasi-Fermi levels can be associated to each semiconductor. These ones can be seen as the Fermi levels of each semiconductor taken independently in the neutral region far from the interface where thermodynamic equilibrium conditions can be assumed. These quasi-Fermi levels associated to each region are separated by an amount qV_{app} because the system is out of equilibrium. Then, as shown in Fig. 2.8, the energy bands separation is a function of the electrostatic potential at the interface qV_0. In an homojunction under thermodynamic equilibrium conditions, the energy barrier height at the interface (qV_0 becomes $q(V_0 - |V_{\text{app}}|)$ under forward bias and $q(V_0 + |V_{\text{app}}|)$ under reverse bias.

[14]Cfr. Streetman reference [23]: Chapter 5: "Junction".

Regarding the diffusion currents, under equilibrium conditions, some carriers have enough energy to overcome the barrier potential at the junction. Out of equilibrium, under forward bias, the lowered potential barrier allows an increasing diffusion current density. Under reverse bias, the barrier is so high that barely no charge carriers have the energy to overcome it. Then, the drift current densities are relatively insensitive to the barrier height. Indeed, the drift current depends on how many carriers are swept towards the barrier by the diffusion processes. If no charge carriers diffuse towards the interface, no carriers experience the electric field and consequently the drift current is zero. Every minority carrier approaching the barrier thanks to diffusion processes will be swept in the other region no matter the size of the barrier. These minority carriers which participate to the drift current are EHP thermally generated close to the interface, at a distance inferior to the diffusion length of the carriers.

Finally, under reverse bias, the total current is relatively small. Indeed, the diffusion current density is negligible regarding the potential barrier height. The only component is consequently the drift current density which is a function of the EHP generation rate $G_0(T)$. A saturation current I_S (cfr. Eq.(2.51)) is established across the PN-junction. Under forward bias, the majority carriers diffuse towards the opposite doped region giving rise to charge carrier excess concentration (cfr. Eq.(2.49) and (2.48)). Indeed, the drift component of the current is reduced due to the reduction of the electric field in the depletion region. As expressed in Eq.(2.39), the ratio of the minority charge carrier concentration and the majority charge carrier of one type depends on the electric potential at the PN-junction. Under a forward bias, the previous equation becomes:

$$p_n = p_p \; e^{-q(V_0 - V_{\text{app}})/k_B T} \qquad (2.40) \qquad \text{and} \qquad n_p = n_n \; e^{q(V_0 - V_{\text{app}})/k_B T} \qquad (2.41)$$

Regarding Eq.(2.40) and (2.41), the probability for a charge carrier to diffuse across the PN-junction is multiplied by $e^{V_{\text{app}}/k_B T}$ in comparison to the thermodynamic equilibrium conditions case. The excess of minority charge carrier concentration Δp_n and Δn_p at the junction is consequently given by:

$$\Delta p_n = p_{n,0}(e^{qV_{\text{app}}/k_B T} - 1) \quad (2.42) \qquad \text{and} \qquad \Delta n_p = n_{p,0}(e^{qV_{\text{app}}/k_B T} - 1) \quad (2.43)$$

Radiative and non-radiative recombinations occur on both side of the interface depending on the minority charge carrier diffusion lengths L_p and L_n which represent the mean distance the minority carriers diffuse before recombination. These diffusion lengths are related to the carrier life times presented in Eq.(2.23) and (2.24) and are given by:

$$L_n = \sqrt{D_n \tau_n} \qquad (2.44) \qquad \text{and} \qquad L_p = \sqrt{D_p \tau_p}\,, \qquad (2.45)$$

where D_n and D_n are respectively the electron and hole diffusion constants. A common way to acquire these constants is to measure the electron and hole mobilities for example by using the Hall effect has it will be described in Chapter 4. Indeed, these quantities are related through the Einstein relations (cfr. Eq.(2.46) and (2.47)).

$$D_n = \frac{k_B T}{q} \; \mu_n \qquad (2.46) \qquad \text{and} \qquad D_p = \frac{k_B T}{q} \; \mu_p \qquad (2.47)$$

As a result, The EHP recombinations occurring on a characteristic time, *i. e.* the mi-

nority charge carrier life time, and consequently a characteristic length, *i. e.* the diffusion length. dictate the minority charge carrier concentration evolution (cfr. Eq.(2.22)).Thus, the evolution of the holes Δp_n and electrons Δn_p concentrations as a function of the position within the opposite doping regions decrease exponentially with a characteristic diffusion length L_p and L_n (cfr. Eq.(2.48) and (2.49))[23][15]:

$$\delta n(x_p) = n_p(e^{qV_{\text{app}}/k_BT} - 1)\ e^{-x_p/L_n} \tag{2.48}$$

$$\delta p(x_n) = p_n(e^{qV_{\text{app}}/k_BT} - 1)\ e^{-x_n/L_p} \tag{2.49}$$

By substituting Eq.(2.29) and (2.30) in Eq.(2.48) and (2.49), the diffusion current associated to each charge carrier type is determined. Then by using Einstein equations: Eq.(2.46) and (2.47) in order to simplify the expression, the total current across the PN-junction of a cross section A is given by Eq.(2.50).

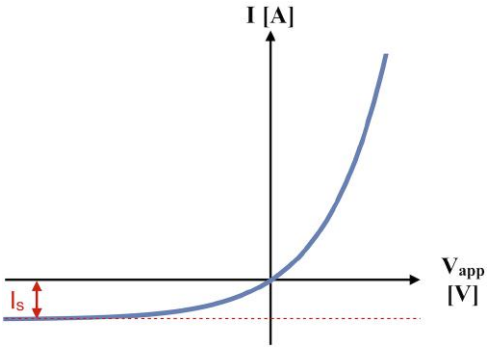

Fig. 2.11: Theoretical IV curve of an ideal PN-junction.

$$I = I_{\text{S}}\ (e^{qV_{\text{app}}/k_BT} - 1) \tag{2.50}$$

$$I_{\text{S}} = qA\left(\frac{D_p}{L_p}p_n + \frac{D_n}{L_n}n_p\right) \tag{2.51}$$

Equation (2.50) is known as the **Shockley diode equation** for which we assume that no generation and recombination takes place in the depletion region. However in real diodes, trap levels within the depletion region can make these recombinations and generations more likely to occur as mentionned in Section 2.1.3. The depletion region contains electrons and holes that cross the junction from one side to the other side. Unless W_{d} is small compared to the electrons and holes diffusion lengths, recombinations occur within the depletion region. In opposition, in the neutral regions recombinations are proportional to the minority carrier concentrations and to the applied voltage. In order to include the recombinations in the depletion region, an ideality factor n can be formally added to the previous Eq.(2.50) (cfr. Eq.(2.52)). This factor varies between 1 and 2 and tells us how the diode is different from the ideal diode characteristics.

$$I = I_{\text{S}}\ (e^{qV_{\text{app}}/nk_BT} - 1) \tag{2.52}$$

As shown on Fig. 2.12, for homojunctions, the minority carriers overcome the energy barrier at the interface of the PN-junction and the excess of minority carriers in the opposite doping regions depends on the bias applied at the junction (cfr. Eq.(2.48)

[15]Cfr. Streetman reference [23]: Chapter 5: "Junctions".

and (2.49)). These ones diffuse over a diffusion length L_n (resp. L_p) of the order of 10 μm before recombination occurs [16] [4][17]. Consequently, the minority carriers concentration decreases as the recombinations occur over a large region. However, as it has been presented in Section 2.1.3, the recombination rate of excess carrier is proportional to the excess of minority carriers concentration. Thus, the larger the diffusion length, the lower the carrier concentration for a given number of EHP and the lower the recombination rate. Consequently, homojunctions are not the more effective type of structure in order to realise high-intensity LEDs.

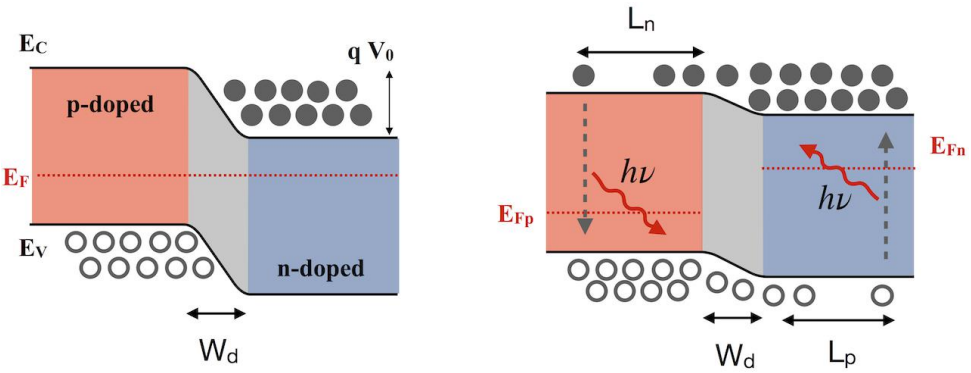

Fig. 2.12: Schematic representation of: (a) a homojunction under thermodynamic equilibrium conditions. minority carriers have to overcome an energy barrier qV_0 in order to diffuse in the opposite doping semiconductor, (b) a homojunction under forward bias: the energy barrier height as been lowered by the external bias applied. Electrons and holes diffuse in the opposite doping semiconductor over a diffusion length before undergoing recombination. EHP recombinations occur over a region of several micrometer which implies a low recombination rate due to a low minority carrier concentration.

Thanks to the study of the PN-junction, the electroluminescence phenomenon in a homojunction is now understood. In the next part of this section, heterojunctions are investigated. These heterojunctions are made of two different semiconducting materials. Therefore, the Fermi levels of the independent material are not at the same position and the energy band gaps are also different. By combining properly the independent properties of the semiconductors, the number of recombinations can be increased.

2.2.3 Heterojunctions

Heterojunctions are made of two different semiconductors, one with a large band gap and another one with a smaller one [23][18]. They consists in the two lattice-matched semiconductors with different band gap energy. As shown in Fig. 2.13, due to the difference between the semiconducting materials used, a specific band structure is obtained. First, in order to create the heterostructure, an interface between the two semiconductors have

[16]Using Eq.(2.45) and (2.44) with the minority carriers life times given in Section 2.1.3, the diffusion length for electrons in a p-doped GaAs is equal to 15 μm with a diffusion coefficient of 220×10^{-4} m^2 s^{-1} and an electron life time of 10^{-8} s

[17]Cfr. Schubert reference [4]: Chapter 4:"LEDs basics: electrical properties".

[18]Cfr. Streetman reference [23]: Chapter 1: "Crystal properties and growth of semiconductors".

to be created. In addition to a band gap difference, the electronic affinities χ of both semiconductors are different.

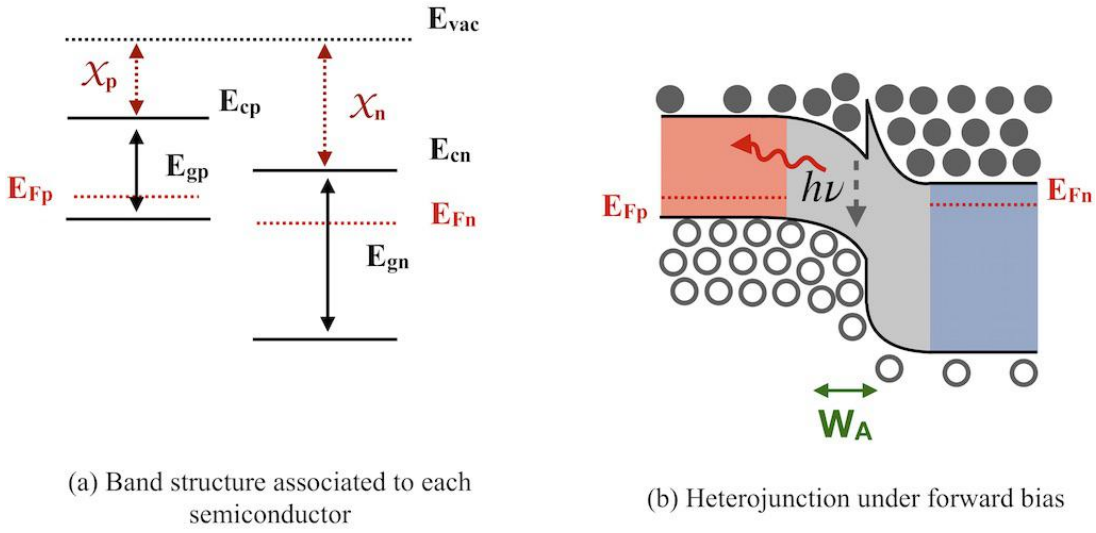

(a) Band structure associated to each semiconductor

(b) Heterojunction under forward bias

Fig. 2.13: Schematic representation of: (a) The independent band structure of two different semiconductors. (b) The heterostructure formed with these semiconductors under an external forward bias. Due to the different band gap and to the different quasi-Fermi level position, a confinement of the minority carrier take place in the structure. This confinement increases the minority carriers concentrations and improves the number of recombinations.

The electronic affinity of a material χ [eV] is defined as the energy difference between the the conduction band energy E_{C} and the vacuum level energy E_{vac} which is the energy at which an electron is free of the attractive potential of the material at an infinite distance. In order to build the band diagram of the heterostructure, the discontinuities in the conduction band ΔE_{C} and in the valence band ΔE_{C} are determined using the Anderson affinity rules:

$$\Delta E_{\mathrm{C}} \;=\; \chi_n - \chi_p \tag{2.53}$$

$$\Delta E_{\mathrm{V}} = (\chi_p + E_{\mathrm{g},p}) - (\chi_n + E_{\mathrm{g},n}), \tag{2.54}$$

where χ_n, $E_{g,n}$ and χ_p, $E_{g,p}$ are respectively the electronic affinities and the energy band gap of the n-doped semiconductor and of the p-doped semiconductor. Then, the Fermi levels associated to each semiconductor have to be aligned under thermodynamic equilibrium conditions implying the bending of the band diagram. The contact potential V_0 is divided between both semiconductors to align the Fermi levels. Then, the depletion region and the contact potential on each side of the interface are determined by resolving Eq.(2.31) with respect of the continuity of the electric displacement at the interface:

$$\epsilon_p \mathbf{E}_p \;=\; \epsilon_n \mathbf{E}_n, \tag{2.55}$$

where ϵ_p and ϵ_n are respectively the electrical permittivity of the p-doped and n-doped semiconductors. As a result asymmetries appear in the band diagram (cfr. Fig. 2.13b). The energy barrier seen from the p-side or from the n-side at the interface is not the

same for the charge carriers. Depending on the electronic affinities and on the band gap energies, the Anderson's rules, Eq.(2.53) and (2.54) give rise to 3 types of heterostructure. Type-1, where both electrons and holes charges carriers are traps, type-2 where only one charge carrier type is trapped and type-3 where charge transfer occurs with a built-in electric potential [28].

As shown in Fig. 2.13, the band diagram associated to the heterojunction allows a confinement of the electrons in the p-doped semiconductor. Indeed, electrons with the required thermal excitation energy can overcome the barrier height and diffuse to the p-side. However, on the other side of the barrier, electrons are confined and cannot spontaneously go back to the n-side of the heterostructure. Regarding the holes, the barrier height is higher than for a homojunction and few of them are able to diffuse in the n-doped semiconductor. By consequence, these heterojunctions allow a thinner active region. Indeed, the distance over which recombination occur corresponds to the width of the confinement and no more the diffusion length. This active region width is of the order of 0.01 to 1 micrometer [4][19].

The reduction of the region on which recombinations occur, the confinement region, the minority charge carrier concentration on the active region on the p-doped semiconductor is increased in comparison to homojunction implying an increase of the recombination rate (cfr. Eq.(2.19)). The recombination life time decreases thus, more recombinations occur and the LED is therefore more efficient in term of global efficiency as it will be presented in the following section. Radiative recombinations occur with an emission of a photon of energy $h\nu = E_g$ with E_g corresponding to the energy band gap of the p-doped semiconductor. Recombinations also occur in the n-doped semiconductor but the minority carrier concentration p_n is smaller than n_p due to the construction of the band structure and the confinement implying fewer recombinations on the n-side.

In a heterojunction, two different semiconducting materials are combined into a unique material system. These media do not necessarily have the same crystallographic properties. The lattice mismatch between the two materials can lead to undesired dislocations and defects in the crystal lattice acting as trap levels in the band gap and leading to non-radiative recombinations. The lattice constant of the heterostructure is determine based on the lattice constant of the semiconductors. As presented in Section 2.1, the band gap energy of the semiconductor is determined based on the lattice periodicity. In case of mismatch the lattice constant of the stacked layer is affected and consequently, the band gap energy of this one also. In case of mismatch the heterostructure is named a pseudomorphic heterostructure. In order to acquire the desire physical properties, the design of the heterostructure and the choice of the semiconducting material is important. This semiconductor research field is called band gap engineering.

In the final section of this chapter, the concept of electroluminescence in heterostructures is used in order to characterise the efficiency of the LED through different quantities. A macroscopic approach of the device and the requirements of TEDs are explained based on the theory of the semiconductor presented in Section 2.1.

[19] Cfr. Schubert reference [4]: Chapter 4:"LEDs basics: electrical properties".

2.3 Light-Emitting Diodes

The electroluminescence phenomenon depends on the band gap energy E_g. One common phenomenon used to acquire this information is the **optical absorption** of incident photons by the semiconductor material. Indeed, photons with energy higher than E_g are absorbed while photons with energy lower than E_g are transmits. Since the valence band contains many electrons and the conduction band many empty states, a photon with an energy $h\nu \geq E_g$ can promote electrons from the valence band to the conduction band. If the photon transfers an energy excess in the form of kinetic energy compared to E_g to the electron, this one will encounter some scattering events with the lattice (phonons) or with defects and finally reach the equilibrium thermal energy of other conduction electrons. However this excited electron is out of balance of the thermal equilibrium concentration of charge carrier. In order to minimise the system energy, this electron will recombine with a hole in the valence band. In opposition, photons with $h\nu < E_g$, are not able to promote an electron from the valence band to the conduction band. Furthermore, if a beam of photons with energy $h\nu \geq E_g$ illuminates a semiconductor material with an incident intensity I_0 in the x-direction, a certain amount of the photons will be absorbed and the rest will be transmitted depending on the thickness of the material and the intensity of the incident beam (cfr. Eq.(2.56)). The beam intensity exponential decay through the semiconducting material is dictated by the absorption coefficient α $[m^{-1}]$ which depends on the characteristics of the materials used. This equation is known as Beer-Lambert's law.

$$\mathcal{I}(x) = \mathcal{I}_0 \, e^{-\alpha x} \tag{2.56}$$

In LEDs, emission wavelength range is consequently fixed by the energy band gap or in case of indirect semiconductor by the position of the trap energy levels within the band gap by respect to the valence band energy.

For practical applications, the external quantum efficiency η_{ext}which consists in the product between the internal quantum efficiency η_{int} (cfr. Eq.(2.28)) and the extraction efficiency ξ_{ex} [29] (cfr. Eq.(2.57)) enable to characterise the LED.

$$\eta_{ext} = \eta_{\text{int}} \times \xi_{\text{ex}} \tag{2.57}$$

The efficiency of LEDs relies on the ration between radiative recombinations and undesired non-radiative recombination modulated by a factor ξ_{ex} which is the ratio between the number of photons generated and the number of photons leaving the LED device. Indeed at each material interface, the refractive index of the different layers are different. Reflection and interference phenomena can occur at each interface of the LED packaging. Therefore, the materials and the architecture of these ones play an important role in the extraction efficiency ξ_{ex}.

The last quantity used to describe the quality of the LED is the global efficiency η. This one is used in a more application point of view and is defined as the ratio between the light emitted power and the injected electrical power. Nevertheless, knowing all these efficiencies, the intensity of the light emitted by LED depends on the application field targeted.

In this master thesis, the LEDs manufactured aim the application field TEDs such as transparent flexible displays[20] such as the Organic Light Emitting Diode (OLED) displays presented in Fig. 2.14a and 2.14c or flexible tablet[21](cfr. Fig. 2.14b). The requirement to fabricate TEDs are a good transmittance $\mathcal{T}$ and a low electrical resistivity ρ.

(a) 77-inch transparent flexible OLED LG display **(b)** Samsung OLED flexible and transparent tablet concept. **(c)** LG transparent and flexible display

Fig. 2.14: TEDs concepts and prototypes.

However, as presented in Section 2.1, these properties are not easy to acquire at the same time in a same material. Indeed, transparent material are insulator which possess filled valence band and empty conduction band for which no photon are absorbed. While conductive materials have the Fermi level within the conduction band [30].

In order to acquire both properties, semiconductors used have degenerate doping [19]. This degenerate doping enables good conductivity thanks to high mobility due to the low effective mass of the charge carriers and a low photons absorption due to the low DOS in the conduction band. The degenerescence induces an increase of the energy band gap. With the Fermi level above the conduction band energy, the states in the conduction band below E_F are filled and consequently excitation of electron from the valence band to the conduction band can only occur with free states above E_F. Photons, in order to get absorbed must have an energy $E_\mathrm{g} + \Delta E$ where $\Delta E = E_\mathrm{F} - E_\mathrm{C}$ and is known as the Burstein-Moss shift [27]. In addition, the band gap energy is also doping-dependent. Indeed, as the doping concentration increases, distance between two impurities is reduced. Consequently, for degenerate semiconductor, the wavefunctions associated to electrons on different impurities can overlap each other. The wavefunctions overlapping lead to the formation of an energy band within the band gap rather then discrete defect levels (cfr. Section 2.1.2). If these trap levels are close to the conduction (resp. valence) band energy in the case of a high doped n-type (resp. p-type) semiconductor, the band energy can merge with the conduction (resp. valence) band and the whole process leads to a shrinking of the band gap. The Burstein-Moss shift and the shrinking of the bang gap are two opposite effects leading to a variation of the band gap energy E_g. These effects depends on the value of N_C (resp. N_V). Indeed in Eq.(2.7) (resp. Eq.(2.8)), the value of N_C (resp. N_V), fix the energy for which the carrier concentration induces a Fermi level equals to the conduction (resp. valence) band energy. Consequently, if N_C (resp. N_V)

[20] `http://www.lgdisplay.com/eng/product/technology/flexibleDisplay` consulted on 10/04/2018.

[21] `https://pid.samsungdisplay.com/en/digital-signage/transparent-displays` consulted on 10/04/2018.

is important, for a high doping, a shrinking effect is observed while in the case of a low N_C (resp. N_V), the degenerescence is reached and the Burstein-Moss shift is observed [27].

In Chapter 5, the numerical resolution of the PN-junction is performed using specific materials properties. A particular attention is given to the doping concentration of the semiconductors. Indeed, a numerical simulation assumption is the non-degenerescence of the semiconducting materials. In order to remain in the hypotheses of the numerical code, an optimisation of the doping is required in order to approach the experimental parameters within the numerical limitations.

In the next chapter (cfr. Chapter 3), the theoretical background of this master thesis is completed with a description of the thin film growth mechanisms. The specific deposition technique used in the experimental part of this work is presented and described and finally and state-of-the-art of the AZO and Cu_2O:Mg TCO is realised.

Chapter 3

Thin Film Deposition

This chapter focuses on the fabrication process of PN-junctions which is divided in two steps. First the deposition parameters optimisation of the independent Cu_2O:Mg and ZnO:Al thin films is performed in order to acquire the highest transmittance $\mathcal{T}$ and the lowest electrical resistivity ρ of the layers. This, in order to realise the most efficient TED as explained in Chapter 2. The second part consists in the formation of the junction. The first section of this chapter (cfr. Section 3.1) aims at the description of the different mechanisms which are involved in the thin film growth [31]. The second section (cfr. Section 3.2) focuses on the Physical Vapor Deposition (PVD) technique called Radio Frequency (RF) magnetron sputtering used in this work. The last section (cfr. Section 3.3) consists in a state-of-the-art section which provides the reader a good insight of what has already been performed with Cu_2O:Mg and ZnO:Al thin films.

Main results and concepts presented and explained in this chapter:

- The thermally-driven motion of the atoms is a key parameter in the thin film growth. Energy-enhanced deposition technique increases the number of adsorbed atoms and increases the crystallinity. Parameters like the impurity concentration, the ambient gas flow rate and the substrate temperature define the structure-zone of the thin film deposited.
- Radio frequency magnetron sputtering deposition techniques is used in this work due to the dielectric behaviour of the AZO and Cu_2O:Mg deposited layers. Depositing parameters like, the substrate temperature T_S [°C], the chamber pressure P [Torr], the power $\mathcal{P}$ [W/m^2] and the argon pressure P_{Ar} are the ones which need to be optimised in the following part of this work.
- Concerning the scientific literature results, the optimal TCO properties are obtained with the lowest chamber pressure P [Torr], the maximum sputtering power $\mathcal{P}$ [W/m^2] (leading to a maximum deposition rate). An experimental study of substrate temperature T_S [°C] combined with a low Ar pressure P_{Ar} with constant flux rate will be performed for both Cu_2O:Mg and ZnO:Al thin films in order to determine the temperature which will provide the most efficient TCO. A 150nm-thick layer will be deposited on a glass substrate, this one providing a high transmittance in the visible and infrared spectrum over 300 nm.

3.1 Thin Film Growth Mechanisms

This section is dedicated to the presentation of the different concepts and physical mechanisms underlying the growth of a thin film. A thin film can be defined as a material manufactured by increasing one by one the atomic species (cluster of atoms) composing the solid film on a substrate [32]. The theory presented here bleow aims at the understanding of the crystallinity and of the morphological properties of the thin films obtained through the complex agglomeration of atoms one by one on a substrate [31]. The thin film growth deposition process can be divided in four parts:

Atom adsorption. The impiging atoms have to be adsorbed on the substrate surface. As shown in Fig. 3.1a, incoming atoms first interact with the surface through Van der Waals (VdW) interactions. These interactions become non-negligible at few atomic distances and are balanced by nuclei repulsion at closer distance. Attracted atoms are consequently in a local potential well created by the substrate surface (cfr. Fig. 3.1b). At this stage incoming atoms are within a certain probability δ_{ads} weakly trapped in a physical-adsorption state (physisorption). Note that in this early-stage of the thin film growth, the only interaction considered is the interaction between incoming atoms and the substrate atoms. When a first layer is deposited, the nature of the interactions is still the same; however, the atomic species in presence are changed. Then, depending on the thermal energy of the substrate surface T_{S}, adsorbed atoms are able to create bonds with atoms of the substrate. T_{S} is a quantity which relies on the kinetic energy of the incoming atoms on the substrate surface. As shown in Fig. 3.1, atoms in physisorption states with a binding energy E_{phys} can jump from one energy configuration to another energy configuration and end in a chemisorption state with a binding energy E_{chem} if the kinetic energy provided by the substrate temperature is large enough to overcome the energy barriers between both energy configurations. If the substrate temperature or the kinetic energy of the incoming atoms are too low, these ones are not able to move from one local minimum to a global minimum. However, if the substrate temperature is too high, the thermal motion is too important and re-evaporation occurs. These chemical bonds consist in the second adsorption state named chemisorption state. This chemical bonding is much stronger but with a lower interacting range than Van der Waals physical interactions (cfr Fig. 3.1a). The probability for an incoming atom to be in a chemisorption state onto the substrate is notated ξ_{c}. Finally, the chemically adsorbed flux J_{r} [$\mathrm{m^{-2}s^{-1}}$] which is the number of incoming atoms adsorbed onto the substrate per unit of time and unit of surface result from a competition between two terms (cfr. Eq.(3.2)).

$$J_{\mathrm{r}}(T_{\mathrm{S}}) = R_{\mathrm{r}}(T_{\mathrm{S}}) - J_{\mathrm{v}}(T_{\mathrm{S}}) \tag{3.1}$$

$$R_{\mathrm{r}} = J_{\mathrm{i}}\ \xi_{\mathrm{c}}(T_{\mathrm{S}}) \tag{3.2}$$

The chemisorption rate R_{r} [$\mathrm{m^{-2}s^{-1}}$] which relies on the number of incoming atoms chemisorbed and the re-evaporation flux J_{v} [$\mathrm{m^{-2}s^{-1}}$] both depending on the substrate temperature. The chemisorption rate depending on J_{i} [$\mathrm{m^{-2}s^{-1}}$], the incident atomic flux. The rate is consequently dominated by the degree of interaction with

the substrate surface. Depending on the deposition technique used, high kinetic energy can be given to the incoming atoms in the form of thermal energy.These energy-enhanced deposition processes enable incoming atoms to have sufficient energy to overcome potential barriers in order to create bonds and enter into chemisorption states. Figures 3.1a and 3.1b present respectively a typical potential barrier landscape generated by one substate atom and by a collection of atoms which form the substrate. This thermal energy provided by the technique used also impact the chemically adsorbed flux.

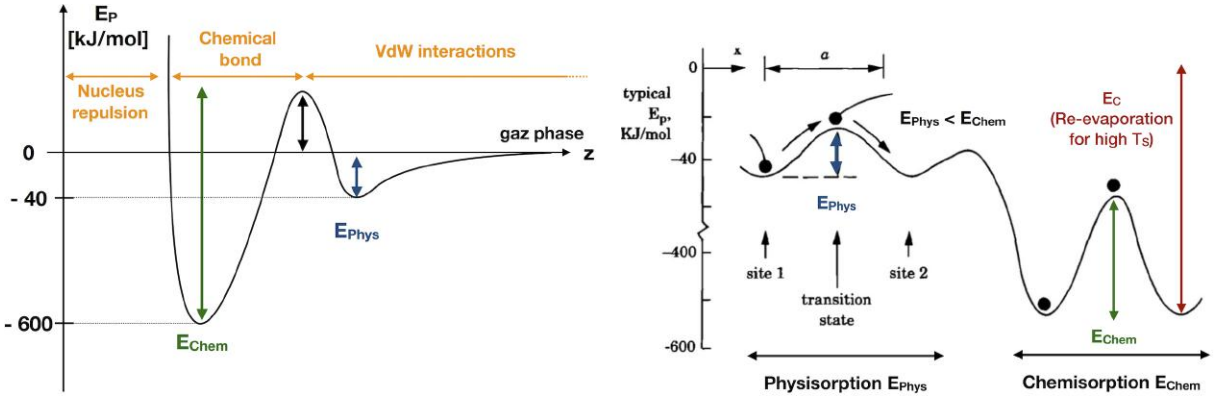

(a) Energetic landscape experienced by an incoming atom and generated by one atom of the substrate material. Domination of the weak VdW interactions at long range which are overcome at few atomic distances chemical bondings with a deeper attracting potential.

(b) Energetic landscape experienced by an incoming atom and generated by the substrate atoms. Depending on the thermal motion enabled by the substrate temperature T_S, atomic diffusions can take place at the surface. If the substrate temperature is too high reevaporation occurs.

Fig. 3.1: Energetic landscape experienced by an incoming atom at the pre-stage of the thin film growth and generated by (a) one or (b) a set of atoms composing the substrate. Reprinted from [31]

Surface diffusion. Due to their thermal energy, the adsorbed atoms are able to diffuse over a certain length before getting incorporated to the film. Concerning the interaction nature atoms are either chemioadsorbed or physioadsorbed. This diffusion process is important in order to minimise the atom energy within the solid in formation. In order to diffuse, atoms have to overcome chemical E_{chem} or physical E_{phys} potential barriers which represent the bonds with the substrate atoms. The rate of barrier overcoming per unit of area and unit of time R_s [m^{-2} s^{-1}] is given by Eq.(3.3) [31][1].

$$R_s = n_s \left(\frac{k_B T_S}{h}\right) e^{-E_S/RT_S} = n_s \, k_s(E_S), \tag{3.3}$$

with E_S the activation energy for surface diffusion which can be seen as the barrier energy according to the site (E_{chem} or E_{phys}) as shwown in Fig. 3.1b and R = $\mathcal{N}_A k_B$. The concentration of atoms in adsorption sites is given by n_s. The rate of barrier overcoming can consequently be expressed as n_s times a function k_s which depends on the activation energy E_S. The diffusion consequently decreases exponentially

[1]Cfr. Reference Smith [31]: Chapter 5:"Deposition"

with the potential barrier height and increases exponentially with the substrate temperature. Furthermore, this atomic diffusion has no privileged direction. Atoms diffuses in both planar directions at the surface of the solid in formation in order to minimise the total energy of the system. The diffusion length is expressed by Eq.(3.4). Where $\mathcal{D}$ is the distance between two adsorption sites and t the time between adsorption and burial by the following deposited layer [2]. Concerning the temperature two regimes can be distinguished, the burial regime where Λ decreases with T_S at low temperature and the desorption regime where Λ increases with T_S at high temperature.

$$\Lambda = \mathcal{D}\sqrt{k_s t}, \tag{3.4}$$

Film nucleation. This third process consists in the initial gathering of the atoms in nucleation centers from which the film growth takes place. Nucleation process depends on the energetic difference between atoms at the surface and atoms within the film.

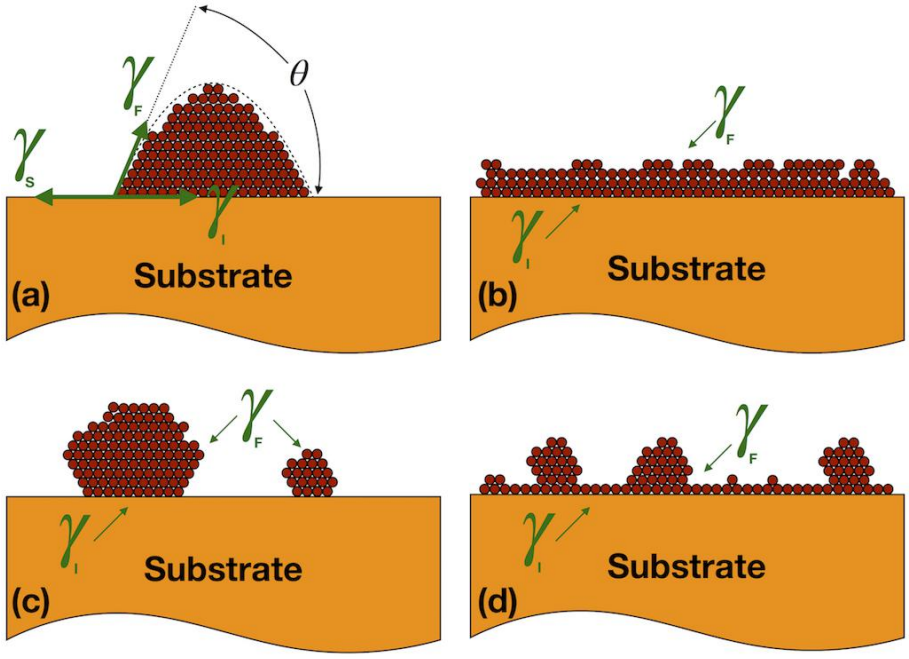

Fig. 3.2: (a) Schematic representation of the different surface energy (film, substrate and film-substrate interface) between clusters of deposited atoms and the substrate. Three types of growth can take place depending on Eq.(3.5) and (3.6). (b) A 2D nucleation occurs when the surface energy decreases with the wetting (Frank-Van der Merwe film growth mode). And (c) a 3D nucleation occurs when the surface energy increases with the wetting (Volmer-Weber film growth mode). (d) The last growth mode is the Stranski-Krastanov which consists in a change in the growth behaviour between 2D and 3D nucleation when first layers are deposited [31].

When an atom is surrounded by others in each direction, its energy is lower than the one at the surface. This energy difference is named the surface energy. In order to create the surface, bonds have to be broken and atoms at this surface are consequently less satisfied than atoms within the solid layers. In addition, this removal

[2]For T_S = 500 K, E_S = 20 kJ/mol (physioadsorbed), a = 0.3 nm and t = 1 ms, $\Lambda = 2.759\ \mu m$

of bonds implies an energy input. Consequently an atom at the surface has a higher potential energy than an atom within the film. The surface energy $\gamma\mathcal{A}$ has to be minimized thanks to atomic motions for instance. $\mathcal{A}$ is the surface area [m^2] and γ the surface tension expressed in [N m^{-1}]. In thin film growth both γ and $\mathcal{A}$ can vary. γ depends on different parameters such as the crystallographic orientation and the chemical composition [31][3], while $\mathcal{A}$ depends on the topography of the surface.

In the case of low diffusion length $\Lambda < \mathcal{D}$, the atoms stick where they land and the growth is said to be quenched [4]. This growth type will be described in the next paragraph. In opposition, as shown in Fig. 3.2 for important diffusion length $\Lambda \gg \mathcal{D}$, atoms can move over a large distance in order to rearrange themselves in the minima of the potential landscape. In this case of $\Lambda \gg \mathcal{D}$ either a 3-dimensional nucleation (cfr. Eq.(3.5) and Fig. 3.2c) or a 2-dimensional (cfr. Eq.(3.6)) and Fig. 3.2b) nucleation occur. The nucleation type is γ-dependent. Furthermore, we need to consider the γ of the substrate γ_S, of the substrate-film interface γ_I and of the film γ_F.

$$\gamma_F + \gamma_I = \gamma_S \qquad (3.5) \qquad \text{and} \qquad \gamma_F + \gamma_I < \gamma_S \qquad (3.6)$$

Consequently, the greater J_r, the more important the nucleation. For Eq.(3.5), the energy surface increases with the wetting. This means that the layers do not stack themselves in a smooth way. In order to reduce the surface energy, the film stops wetting the substrate and forms 3D shapes called islands (cfr. Fig. 3.2c). This type of nucleation, called Volmer-Weber film growth mode is usually undesired because it induces surface roughness. In opposition, Eq.(3.6) treats the case of a "wet" surface, in means that the surface energy is lower for a wetted surface than for a bare one. The thin film growth is consequently quite smooth and the layers deposit themselves one by one (cfr. Fig. 3.2b). This growth type is known as the Frank-Van der Merwe film growth mode. Finally, the Stranski-Krastanov film growth mode tackle the behaviour changing between 2D and 3D nucleation when the first layers are deposited (cfr. Fig. 3.2b). One way to tune the nucleation type is to tune γ_I which decreases with stronger substrate-film bonding. Energy-enhanced deposition provides the activation energy required to create pass from physorbed sites into chemisorbed sites (cfr. Fig3.1) and consequently to reduce γ_I in order to increase the wetting.

Structure development. The last step is about the film growth from nucleation sites. Indeed, atoms gather and rearrange themselves in order to obtain a solid structure. The structure depends drastically on the temperature and more precisely on the thermal motion which takes place during the film growth. As presented, surface diffusion depends on the kinetic energy of the impinging. If this energy is large, surface diffusion, surface energy of the solid in formation is reduced and the crystallinity improved. The thermal motion of the impinging atoms is the chaotic, the brownian motion of atoms occurring at the surface and imply by the temperature. It represents a measure of the kinetic energy of the atoms which diffuse at the solid' surface.

[3] Cfr. Reference Smith [31]: Chapter 5:"Deposition"

[4] Quenched means that incoming atoms do not have the possibility to diffuse at the surface of the substrate due to the low temperature inducing an immobilisation of the atoms where they land.

In 1958, a structure-zone model has been presented by John A. Thornton [33] in which the influence of the substrate temperature on the structure growth was described. The observation of the structure-zone model can be performed in two steps: the growth structure (columnar or layered structure) of the thin film which depends on the nucleation mechanisms and the microstructure of the thin film within these growth structures.

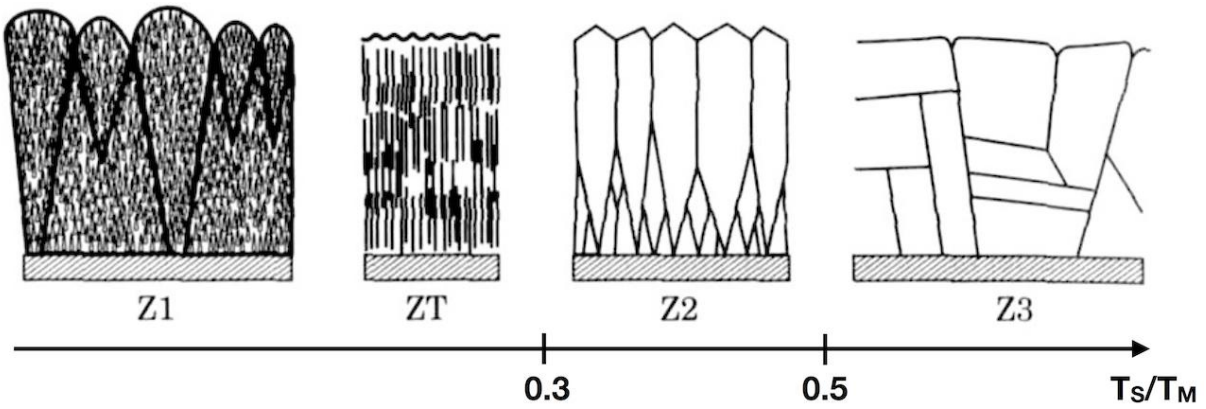

Fig. 3.3: Thornton' structure-zone model of thin films. Impact of the substrate temperature T_S on the crystallinity of the thin film. Thermal motion allows atomic surface diffusion resulting in improved thin film crystallinity. The size of the grains in the polycrystalline structure increases with the substrate temperature [33].

As it can be seen in Fig. 3.3, the diagram is structured in four zones (Z1, ZT, Z2 and Z3) which depend on the reduced temperature T which is the ratio between the substrate temperature T_S and the melting temperature of the deposited material T_M.

- In Z1, the reduce temperature T is low and it induces a small surface diffusion ($\Lambda < \mathcal{D}$) the crystaline structure consist in thin columns width of tens of nm. These ones are generally amorphous and separated by voids with a droplet like shape. The size of these ones increases as the film becomes thicker. The surface roughness of these films is quite important and present alveolar shapes.
- In ZT, the same columnar structure is observed. However there is no void. This absence is due to the energy-enhanced processes. Indeed, thanks to these types of deposition techniques, the impinging atoms have a higher energy than non-enhanced processes. This additional energy allows a surface diffusion occurring on a larger distance Λ. As a result, the surface energy is minimized, the voids are filled and the thin film crystallinity is improved. Energy-enhanced deposition processes allows a higher surface diffusion without increasing the substrate temperature.
- In Z2, $T_\mathrm{S}/T_\mathrm{M}$ is higher than 0.3. In this structure-zone, the surface diffusion becomes meaningful thanks to the increasing substrate temperature and the structure consists of columns with thin grain boundaries between them. The diameter of these columns increases with the reduce temperature and the crystallinity of these ones are better than in Z1 and ZT zones.

- In Z3, thermal motion is high enough to allow diffusion processes within the layers during the deposition in which the atoms rearrange themselves in order to improve the crystallinity. This zone is usually more isotropic concerning the crystallinity.

The Z1 and ZT zones correspond to the quenched growth while Z2 and Z3 correspond to the thermally reactivated rearrangement. This Thornton' structure-zone model is the result of examinations of thin films using SEM and Tunneling Electron Miscroscope (TEM) imagining combined with computer simulations. This model developed in the 20th century is meant to be used as a guideline in order to select the proper deposition parameter to acquire the desired crystallinity. It is not used to acquire quantitative measurement. Indeed, the Thornton' structure-zone model presented in Fig. 3.3 is realised first for the deposition of metallic thin films as a function of the parameter of a specific deposition process. As explained, this one aim the characterisation of the thin film morphology in two steps. The growth structure and the intrinsic microstructure.

In the next section, the deposition process used in this work to synthesize the thin film is presented. The influence of the deposition parameters on the crystallinity is described and these parameters are studied independently.

3.2 Experimental Thin Film Deposition Process

Over the past two hundreds years, thin film deposition processes ongoing a great interest in the field of condensed matter physics. Moreover, electronic devices and optical coatings have been manufactured over the past fifty years by the used of different deposition techniques which are still in constant development nowadays [32]. In the first part of this section, a brief review of deposition techniques will be performed. The goal of this review is to provide an insight of the different techniques available.

Nowadays the deposition processes can be classified in two different categories depending on the principles responsible for the deposition. The first class is the Chemical Vapour Deposition (CVD) techniques. This class of deposition techniques include chemical reactions or decompositions between different vapour-phase precursors on a substrate in order to achieve the deposition. CVD processes include reactions initiated by heat (thermal CVD), by high-frequency radiation (photo-assisted CVD) or by a plasma (plasma-enhanced CVD) [34].

The second class consists in the Physical Vapor Deposition (PVD) techniques in which we will be interested in this work [35, 36]. PVD depositions include thermal evaporation processes, sublimation processes or sputtering processes. These processes are performed in a vacuum environment and the deposition can be summarised in four steps:

- First, the gaseous phase is formed which can be performed using a high energy source such as a resistive heating or an electron beam bombardment in evaporation processes. The vapour phase can also be done using ions bombardment which is the basic principle of sputtering processes. Concerning the deposited material, electron beam bombardment can also implies sublimation of the targeted material. Typically high vacuum is reached for PVD deposition.
- Then, the vaporised atoms spread into the vacuumed chamber. As presented in Tab.3.1, the mean free path of the vaporised atoms depends on the level of vacuum reached.

Vacuum level	**Pressure range** [Torr]	**Mean Free Path** [m]
Medium Vacuum	25 - 10^{-3}	10^{-6} - 10^{-2}
High Vacuum	10^{-3} - 10^{-9}	10^{-2} - 10^{2}
Ultra High Vacuum	10^{-9} - 10^{-12}	10^{2} - 10^{4}

Tab. 3.1: Evolution of the mean free path of the particle as a function of the level of vacuum reached at 300 K [37].

- The third step consists in the reaction with a gas present in the chamber. This step is used in reactive magnetron sputtering deposition technique which allows deposition of material with a tuneable stoichiometry depending on the gas flux injected into the deposition chamber. For non-reactive process, the vaporised atoms travel trough the deposition chamber and the stoichiometry of the deposited thin film depends only on the stoichiometry of the materials evaporated.

- Finally, the vaporised atoms condense on the substrate and sustain the thin film growth at a fixed rate depending on the sputtering power $\mathcal{P}$ and the chamber pressure reached.

Thermal evaporation process can be performed by using a resistance in order to evaporate a material by Joule heating, or by using an electron beam bombardment onto the targeted material. However, these techniques have some drawbacks like in situ precleaning lack, difficulty to evaporate high melting temperature elements and difficulty to evaporate non-conducting elements [36]. That is why the sputtering PVD deposition technique is used in this work. In addition, the sputtering process PVD is by its functioning, an PVD technique providing a large amount of energy to the vapourised atoms. This one could be compared to the energy-enhanced deposition technique with all the consequences presented in Section 3.1 in terms of thin film crystallinity improvement.

The following part of this section is dedicated to the description and the explanation of the **RF Magnetron Sputtering** deposition technique used in this work. The pre-deposition processes consisting in the cleaving and cleaning of the substrate are also described. And finally, the RTA post-deposition process is presented in order to understand the deposition parameters presented in Section 3.3.

3.2.1 Radio Frequency Magnetron Sputtering

In order to achieve the ZnO:Al and Cu_2O:Mg thin film depositions, the RF magnetron sputtering method was used. This method consists in the bombardment of a solid material target by positive ions in order to initiate the erosion and the sputtering of the targeted material. The atoms are ejected from the surface and it creates a vapour of the targeted material used for the thin film deposition. This deposition technique creates a high energetic atomic vapour. Due to the high kinetic energy of the vapour atoms, this technique is one of the energy-enhanced technique evoked in Section 3.1. The atoms then travel to the substrate and supply the growing film. J.K. Robertson observed in 1933 the first metallic sputtering induces by high-frequency currents [38].

Let's now focus on the **Sputtering** process itself [31][5]. In order to perform a correct sputtering deposition, vacuum has to be performed in the deposition chamber. The lower the vacuum, the lower the contaminant concentration in the chamber and the better the crystallinity of the thin film (cfr. Fig. 3.4). In this work, contaminant stands for undesired species of molecule or atom presents in the deposition chamber such as water vapour, air, dust, remains of previous depositions etc. Indeed, in order to perform a clean deposition of the material unwilling condensation of contaminant on the substrate must be prevented. The main contaminant which can condense onto the substrate is the water vapour presents in the air. The Hertz-Knudsen equation (cfr. Eq.(3.7)) [39, 40] gives the residual gas flow N [m^{-2} s^{-1}] per unit of time and area. An estimation of the H_2O monolayer which deposits onto the substrate according to the pressure P [Torr] and the temperature T [K] of the depositing chamber can be obtained, M is the molecular weight of the remaining gas species [g/mol] [41].

$$N = 3.53 \times 10^{26} \frac{P}{\sqrt{MT}} \tag{3.7}$$

[5]Cfr. Reference Smith [31]: Chapter 5:"Energy beams"

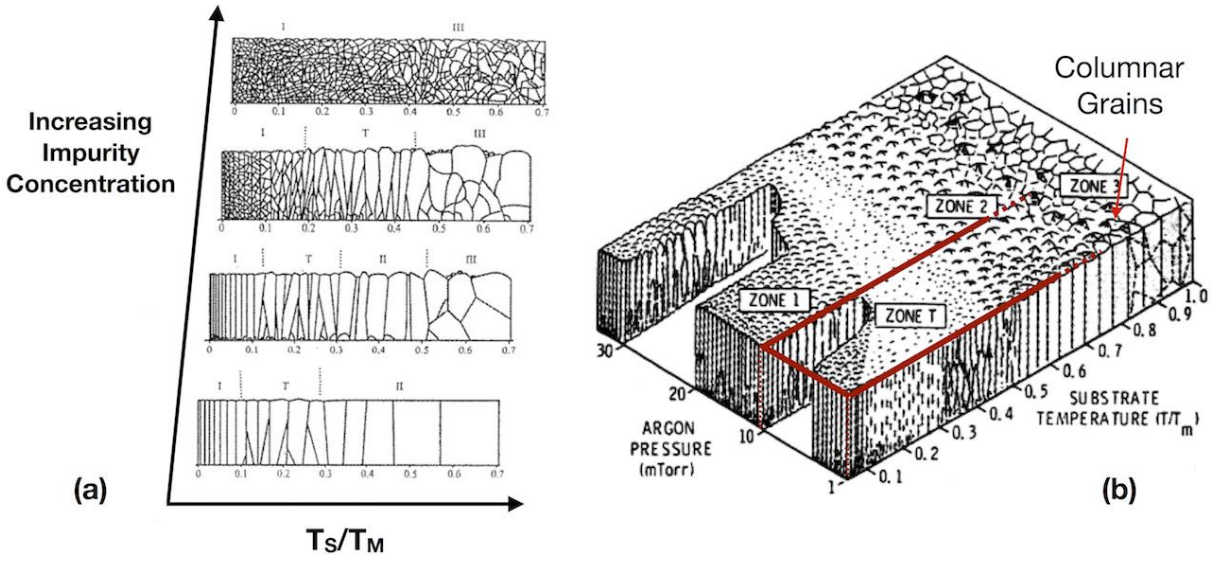

Fig. 3.4: Thornton' structure-zone model. Evolution of the crystallographic structure of the thin film concerning the reduce temperature (T_S/T_M), the argon pressure P_{Ar} and the impurity concentration. The size of the grains composing the polycrystalline structure as the voids within the structure evolve depending on these parameters. The thin film properties consequently depends on the deposition parameters (T_S, P_{Ar} and P)

There is a linear dependance between the number of contaminants and the remaining pressure in the chamber.The pressure parameter must consequently be as low as possible. Moreover, as shown in Fig. 3.4a, the size of the grains composing the polycrystalline structure decreases as the impurity concentration increases. In order to improve thin film purity by avoiding the contaminants impinging during the deposition, the chamber pressure before deposition P [Torr] must be as low as possible.

Illustration of the experimental aspects of sputtering are shown in Fig. 3.5. The targeted material (cfr. Fig. 3.5c) (in brown in the schematic representation Fig. 3.5b) is placed in the vacuum chamber and the substrate is placed at the top of the deposition chamber. Once the chamber pressure P [Torr] reaches 10^{-6}-10^{-7} Torr using a vacuum turbo pump, the chamber is backfilled with a high purity inert gas. Argon gas is usually used because it is a noble gas which does not react with the material deposited. Furthermore, its relative mass and ability to transport kinetic energy upon impact make it a good candidate for the ion gas in RF magnetron sputtering deposition [31][6]. Then, as the chamber is filled with argon, electrically neutral argon atoms are ionised and shift into a plasma state. The ionisation occurs by collisions of electrically neutral argon atoms on the surface of the cathode which consists in the negatively biased support of the targeted material. A plasma mixture of ions and electrons is formed in the chamber. Moreover, the plasma formation is a dynamic process in an equilibrium state, the ions composing the plasma capture electrons from the cathode and these excited electrons emit light in order for the argon atoms to return in their ground state (cfr. Fig. 3.5a).The pressure P_{Ar} [Torr] and the flow rate f_{Ar} expressed in Standard Cubic Centimeter per Minute (sccm) of the Ar gas injected in the chamber can be tuned. The argon pressure must be high enough in order to sustain the plasma present in the chamber. An increase of the Ar

[6]Cfr. Reference Smith [31]: Chapter 5:"Energy beams"

pressure increases the sputtering rate but a too high Ar pressure also leads to a reduction of the mean free path of the particle in the chamber which is undesired in the deposition process. A pressure of 5 to 10 mTorr is usually used. Concerning the flow rate, this one allows a continuous renew of the unionised Ar atoms. In our experiment, this one is fixed around 20 sccm. As shown in Fig. 3.4b, the size of the grains in the polycrystalline structure of the thin film depends on the argon pressure. However, the impact of the Ar pressure on the crystalline quality of the film seems less important than the impurity concentration and the substrate temperature. The argon pressure accessible using the sputtering deposition technique in the SPIN research group is between 1 to 10 mTorr. Consequently, depending on the substrate temperature, structure-zone for the thin film is between ZT, Z2 and Z3 (cfr Fig. 3.4 and Section 3.1).

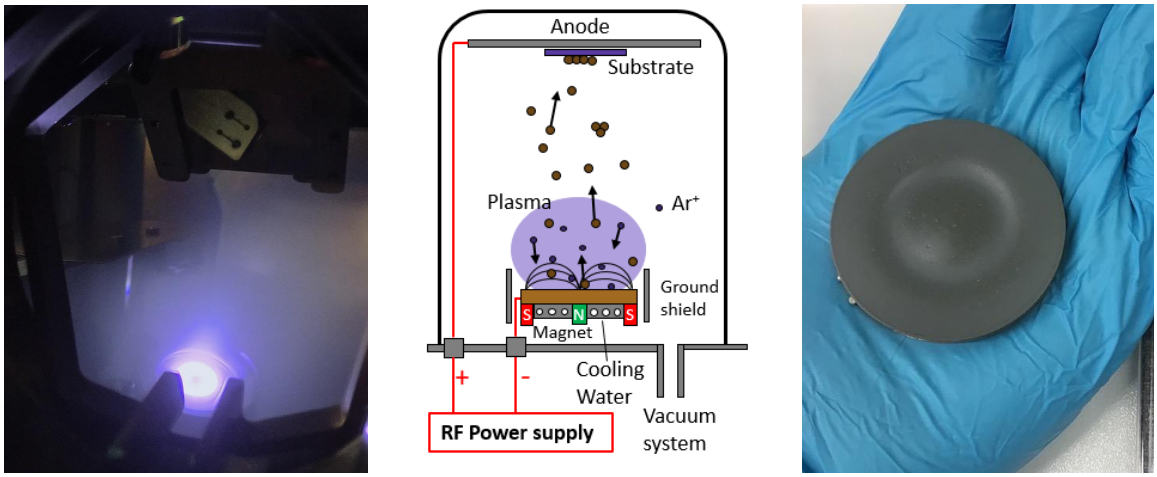

(a) (b) (c)

Fig. 3.5: (a) Photography of the argon plasma. (b) Schematic representation of the RF magnetron sputtering deposition process. First, the vacuum is performed in the deposition chamber until 10^{-6}-10^{-7} Torr. Inert agron gas is injected into the chamber ($P_{\mathrm{Ar}} = 1 - 10$ mTorr) and is ionised by the negatively biased support of the targeted material (cathode). Confinement of the charged particles (electrons and ions) occurs thanks to magnets placed below the targeted material in order to increase the sputtering rate. Ionised argon atoms forming the plasma state are accelerated by the external bias applied in order to initiate the sputtering of the target. A gaseous phase of the targeted material is formed in the vicinity of the substrate and condensation at the surface of this one occurs. AC bias is applied in order to avoid the charge build up of the target. (c) AZO sputtering target.

The point from which electrons enter into the system in order to ionise the argon atoms is the cathode, the negatively biased targeted material holder (cfr. Fig. 3.5b). In the case of conductive targeted materials, the target itself is biased. In the case of dielectric or less conductive material like AZO and Cu_2O:Mg, a conductive material like copper is sticked to the target material (cfr. Fig. 3.5c). At this stage, an argon plasma state is achieved. The use of magnets located behind the targeted material allows a confinement of the charged particles (electrons and ions) which improve the formation of the ionised gas. This confinement allows the improvement of the sputtering rate. This sputtering rate is the number of argon ions hitting the substrate surface per unit of surface and unit

of time. This deposition configuration is called **Magnetron Sputtering**.

The ionised argon atoms are accelerated via the bias applied and they collide with the targeted material which leads to the erosion of this one if the energy transferred by the collision is sufficient. The energy of the Ar atoms must be higher than the binding energy of the targeted atoms. Targeted atoms are thus sputtered and form a gaseous state in the chamber. These ones spread into the chamber and finally condense onto the chamber walls and onto the substrate. The whole process leads to the presence of targeted material vapour in the vicinity of the substrate. In this work, an AC radio frequency electrical bias is applied over a DC bias electrical bias in order the avoid the charge build up by the positive ions collisions on the targeted materials, leading to a secession of the sputtering atoms. Indeed arcing and contamination of the targeted material is avoided using this radio frequency AC electrical current. The frequency used is 13,56 MHz as fixed by international standard for thin film sputtering. At this stage, the deposition technique is called **Radio Frequency Magnetron Sputtering**. The deposition rate [Å/s] can also be tuned by modulation of the bias applied at the cathode. This bias control the energy and the number of Ar ions which impact the targeted material (sputtering rate). Moreover, the higher the sputtering rate, the higher the deposition rate. The power $\mathcal{P}$ [W/m^2] applied is also related to the deposition rate. It is also important to note that a too high power can lead to the melting of the material. In order to prevent this unwilling change of state, a cooling water system is used.

As it has been introduced in the previous section, the substrate temperature T_S [°C] can also be tuned in order to modulate the deposited layers properties. Nevertheless, it is important to keep in mind that with a deposition on a former deposited material substrate, a high T_S leads also to in-situ annealing during the deposition. This one can induce atomic diffusion between both layers and leads to an indistinct interface between both layers. For this work, the distinct interface is however required in order to acquire a rectifying PN-junction. In order to highlight this effect, the deposition order of the layer is studied in this work concerning the optimum deposition temperature of both AZO and Cu_2O:Mg layers.

In this work, RF magnetron sputtering depositions are performed using a "Nexdep" PVD system from Angstrom Engineering [7]. In the experimental protocol used for the depositions, the vacuum is performed in the chamber as low as possible, as motivated before. A layer of several nanometers of titanium is deposited into the chamber[8] in order to stick a portion of the remaining impurities on the chamber walls. The titanium is used due to its high reactive potential which allows the chamber pressure reduction from 10^{-7} Torr to 10^{-8} Torr. Indeed, the titanium high reactivity with oxygen and consequently water vapour, allows to capture a part of the remaining molecules in the chamber and to stick them onto the chamber wall. Then, a pre-sputtering of the target is performed in order to clean this one by removing the first contaminated layers. Finally, the deposition is performed. In the following parts of this section, the pre-deposition and post-deposition processes are presented.

[7] Further information on the device can be found in the following reference: `https://angstromengineering.com/products/nexdep/` consulted on March 20, 2018.

[8] During this pre-deposition process, the substrate is protected thanks to mechanic shutters.

3.2.2 Pre-Deposition Process

Before each deposition the substrate must be cleaved and cleaned. These operations are realised in a chemical room under an extractor hood in order to protect the operators when using chemical compounds and also to avoid any unwilling particles on the substrate. The wafer used for our samples is made of a 2mm-thick glass coated with 300 nm of fluorine-doped tin oxide (FTO[9]) which is a good electrical conductor with a sheet resistance of $15\Omega/\square$ widely used in transparent opto-electronic devices.

First, the glass wafer is cleaved using dedicated tools and sprayed using an nitrogen gun to remove the largest waste particles resulting of the cleaving. Then a chemical cleaning of the substrate is performed. The sample is first placed for 10 minutes in an ultrasonic bath of an organic solvent at 55°C. The solvent used is the acetone[10] C_3H_6O which removes and cleans oils and organic residues. However the acetone also leaves its own residues on the sample. It is by consequence required to use a second cleaning method. After removing the sample from the acetone bath, the air-pistol is used to avoid the drying of the acetone on the sample in order to minimise the acetone residue. Finally the sample is submerged in an ultrasonic bath of isopropanol[11] (Isopropanol (IPA)) C_3H_8O for 5 minutes at room temperature. The IPA is an alcohol which is a good trace remover. Finally, the sample is rinsed using deionised water, blowed using the nitrogen pistol and placed in a transport sample box.

Note that along all the processes in the experimental part of this work involving the manipulation of the sample, gloves are used in order to avoid the deposition of unwilling organic wastes on the sample and this one is meticulously manipulated using plastic or metallic pliers.

3.2.3 Post-Deposition Process

After the deposition, the material layer can be annealed using a Rapid Thermal Annealing (RTA) in order to increase the crystallinity of the thin film. This ex-situ post-deposition procedure can be classified as the fifth point of the thin film growth process established in Section 3.1. Indeed, during the post-annealing, atomic diffusions happen within the layers of the deposited thin film. These atoms rearrangements allow to improve the crystallinity of the layer thus consequently to reduce the number of defects in the structure and consequently concerning Eq.(2.14) to reduce the resistivity. However, concerning the slope of the annealing, the annealing time and the annealing temperature different processes such as atomic diffusions with the substrate (like mentioned in Section 3.2.1) or melting can occur and lead to undesired changes of the thin film properties.

As it can be seen in Fig. 3.6, the annealing device used in the SPIN group research

[9]The substrate used can be found at the following reference: `https://www.sigmaaldrich.com/materials-science/material-science-products.html?TablePage=106837645` consulted on March 15, 2018.

[10]The material safety data sheet for acetone can be found at the following reference: `http://www.sciencelab.com/msds.php?msdsId=9927062` consulted on March 15, 2018.

[11]The material safety data sheet for isopropanol can be found at the following reference: `http://www.sciencelab.com/msds.php?msdsId=9924412` consulted on March 15, 2018.

lab is a "Mini Lamp Annealer MILA-5000 series" from Advance Riko, Inc [12].

Fig. 3.6: Photography of the "Mini Lamp Annealer MILA-5000 serires" from Advance Riko, Inc.

This machine uses a heating system composed of an infrared lamp and paraboloic reflectors. This one is placed on a quartz glass tube in order to perform a clean heating without gas emission from the lamp. The sample is placed in the furnace chamber. When this latter is sealed, a continuous flow of nitrogen gases is introduced in the chamber all along the annealing. A nitrogen atmosphere is established in order to avoid water vapour presents in the air to interact with the sample and to oxidise it during the annealing. Furthermore, an excessive pressure of N_2 compare to the atmospheric pressure is established in the chamber to avoid any penetration of the external air. Finally, a water circuit is used to cool down the chamber until room temperature. This device allows thermal treatment until 1200°C with a maximum slope of 50°C per second.

In the next section a specific attention is paid to Transparent Conducting Oxide (TCO). First, a quick review of these materials is presented and the choice of Cu_2O:Mg and ZnO:Al is explained. Finally, the state of the art of the deposition parameters used for the deposition of Cu_2O:Mg and ZnO:Al thin films using RF magnetron sputtering deposition technique is presented in order to provide the reader a good understanding of the choice of the deposition parameters used in this work. The experimental section concerning the thin films growth and the junction formation is presented in Chapter 6.

[12]Further information on the device can be found in the following reference: `https://advance-riko.com/en/products/mila-5000/` consulted on March 15, 2018.

3.3 State of the Art: Cu_2O:Mg and ZnO:Al Thin Film Growth

This section is dedicated to a description of the TCOs: Cu_2O:Mg and ZnO:Al used to fabricate the junction. First, a brief presentation of these materials is performed within the motivation behind their choice. Then, an independent state of the art of both materials is provided. This presentation aims the impact of the deposition parameters on the electrical, optical, and morphological properties of the thin films deposited. Indeed, as presented in Sections 3.1, the electrical and optical properties of the thin films are closely related to the crystallinity of these ones. The parameters studied in the scientific literature are presented in order to acquire the knowledge required to understand the investigation performed in Chapter 6 in which the optimisation of the deposition parameters studied in this work is presented.

As described in Chapter 1, Aluminium-doped Zinc Oxide (AZO) and magnesium-doped cuprous oxide Cu_2O:Mg are the two TCOs used in this work. The most commonly used n-type TCO is the ITO due to its high electrical conductivity and transmittance characteristics [15]. However, the scarcity of this material and the high cost of fabrication represent some drawbacks in the actual expanding TEDs market. AZO, a n-type semiconductor, has emerged as a good candidate as TCO thanks to its low fabrication cost and its optimal electrical and optical properties comparable to ITO [42]. As it has been previously presented, this degenerate semiconductor has been widely studied over the past few years (cfr. Fig. 1.2b). ZnO is an inorganic II-V semiconductor crystallizing in a a polycristalline wurtzite structure as presented in Fig. 3.7a [43]. It is a direct band gap semiconducting material with an energy band gap of 3.37 eV at 300 K allowing a high transparency in the visible wavelength range.

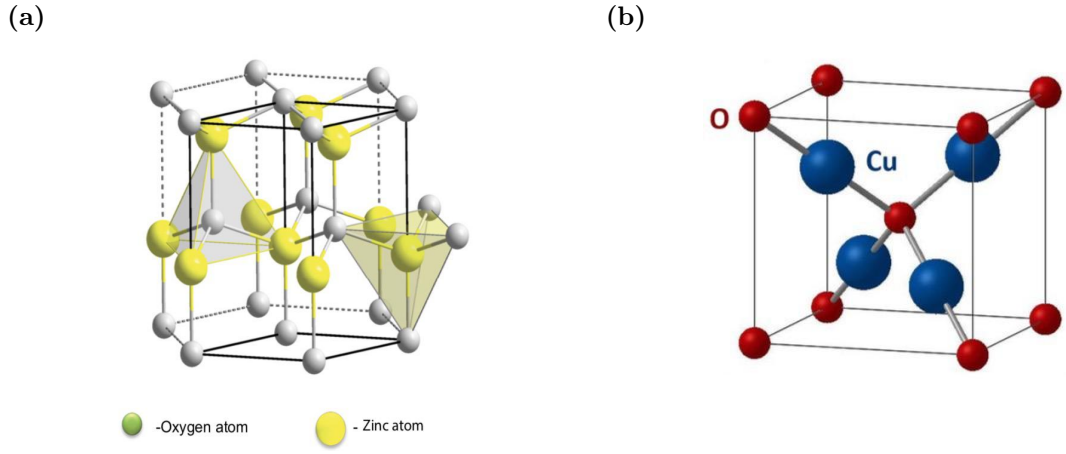

Fig. 3.7: Schematic representation of (a) the ZnO wurtzite crystalline structure and (b) the body centred cubic (BBC) crystalline structure of Cu_2O. Reprinted from [43] and [18]

The p-type semiconductor used in this work, is the magnesium-doped cuprous oxide. As presented in Chapter 1 (cfr. Fig. 1.2b), the research focusing on Cu_2O:Mg as p-type TCO is actually quite poor. Nevertheless, the good electrical characteristic and the fabrication ease of Cu_2O:Mg make this material a promising p-type inorganic semiconducting

materials for TED applications. Cuprous oxide crystallize in a body centred cubic crystalline structure as presented in Fig. 3.7b. In addition, its direct band gap band structure with a band gap energy width of 2.09 eV at room temperature [18] provides the band gap energy required in the emission of light in the visible wavelength range.

3.3.1 Cu_2O:Mg Thin Film Growth

In this part, we focus on the RF magnetron sputtering deposition parameters studied in the literature concerning magnesium cuprous oxide thin films. The goal is to highlight the impact of these parameters on the electrical resistivity ρ (free carriers mobility μ_p and free carriers concentrations p), on the optical characteristic and on the crystallinity of the deposited layer.

As presented previously, the RF magnetron sputtering deposition of Cu_2O:Mg has been poorly investigated. Consequently, the optimisation of the deposition parameters and post-deposition treatment are mainly based on the results obtained by the SPIN research group from the University of Liège [44, 45]. The interest in this magnesium-doped cuprous oxide material comes from R. Frerichs *et al.* 1958's article [46] reporting the observation of the electroluminescence phenomenon in a rectifying interface of bulk cuprous oxide with a metallic materials.

Concerning the RFmagnetron sputtering deposition parameters impact on the Cu_2O:Mg thin film properties, the substrate temperature T_S is likely one of the most relevant parameter within the argon pressure P_{Ar} as presented in Section 3.1. The impact of the substrate temperature has been highlighted by [44] which has observed a one order of magnitude increase in the electrical resistivity, from 4×10^2 to 4×10^2 Ωcm between T_S=40°C T_S=400°C. The increase of the substrate temperature also induces an increasing of the transmittance in the visible wavelength range and a band gap energy reduction from 2.64 eV to 2.54 eV. He also observed thanks to SEM imaging than an increasing substrate temperature lead to an increasing of the porosity and the presence of out growth structure at the thin film's surface.

3.3.2 ZnO:Al Thin Film Growth

In this part, we focus on the RF magnetron sputtering deposition parameters studied in the literature concerning AZO thin film depositions. The goal is to highlight the impact of these parameters on the electrical resistivity ρ (free carriers mobility μ_n and free carriers concentrations n), on the optical characteristic and on the crystallinity of Al-doped zinc oxide thin film.

First of all, concerning **the deposition chamber pressure** P [Torr], the lower the deposition pressure the better the thin film morphological properties. As presented in Section 3.2, the decrease of the deposition pressure in order to avoid any contaminations of the deposited layers as described in Eq.(3.7) [31][13].

Several studies were performed concerning **the sputtering power** $\mathcal{P}$ [W/cm^2]. Nunes *et al.* [47] highlighted the fact that an increasing deposition power from 2.54 to 7.64

[13]Cfr. reference [31]: Chapter 5: "Deposition"

W/cm^2 leads to a decreasing of the electrical resistance of nearly one order of magnitude due to both an increasing of the carrier mobility and carriers concentration. An increasing of the absorption coefficient is also observed in the visible region. Concerning the resistivity, the same observation was performed by Chun *et al.* [48] and by J.F. Chang *et al.* [49]: a resistivity decrease is observed when the power is increased due to a better crystallinity. Band gap energy ranging from 3.3 to 3.6 eV were reported. Spadoni *et al.* [50] also observed that an increasing power from 1.32 to 2.63 W/cm^2 leads to an increasing deposition rate DR [Ås^{-1}] from 0.83 to 3.16 Å/s and a decrease of the resistivity of one order of magnitude. Nearly no impact on the transmittance in the visible region were observed and an increasing of the band gap energy from 3.44 to 3.51 eV is shown. The same trend was observed by Y. Igasaki *et al.* [51] concerning the relation between the deposition rate and the sputtering power.

Then, several studies of **the substrate temperature** T_S [°C] were also performed. Y.H. Kim [52] experimentally observed that an increasing substrate temperature from 150°C to 450°C leads to an increasing resistivity of nearly one order of magnitude from 4×10^{-4} to 2×10^{-3} Ωcm due to both a decreasing of the carriers mobility and the carriers concentrations. The transmittance does not seem to be impacted by the substrate temperature and is around 85% in the visible range. Nevertheless, the absorption coefficient decreases of nearly one order of magnitude from RT to 450°C. The optimal substrate temperature both for the resistivity corresponding to a maximum of the carrier mobility and concentration and for the crystallinity was reach with T_S = 150°C. Concerning the impact of T_S on thin film characteristic, Jahed *et al.* [53] observed a decrease of the electrical resistivity from 10^{-3} to 10^{-4} Ωcm for an increasing substrate temperature from 25 to 250°C. A transmittance of 80% in the visible wavelength range is obtained and nearly no impact of T_S is observed. Finally, Jahed *et al.* also reported a slightly increasing of the crystallinity with an increasing crystal size from 11.92 to 12.94 nm between T_S from room temperature to 250°C. Then, Cornelius *et al.* [54] observed a minimum of the electrical resistivity of at 350°C due to both a maximum of the electron mobility and carrier concentration. However in this paper the deposition study was performed using a flow of O_2 in the chamber. Concerning the electrical resistivity, the same trends were established by Minami T. *et al.* [55] in 1989.

Concerning the **argon pressure** P_{Ar}, Deok Kyu Kim *et al.* [56] highlighted that at room temperature, an increasing Ar pressure from 1 to 2 mTorr leads to an electrical resistivity increasing from 3.5×10^{-3} to 8.5×10^{-3} Ωcm, an increasing band gap energy from 3.403 to 3.537 eV and a red shift in the transmittance measurement is observed. Moreover, both the RMS roughness and the average crystallite size increase respectively from 1.5 to 2.3 nm and 25 to 28.5 nm. However, Nunes *et al.* [47] observed the opposite trend concerning the electrical resistivity. A major difference of one order of magnitude in sputtering power (0.54 W/cm^2 for Kim and 5.09 W/cm^2 for Nunes) in the two different studies has to be taken into account. Finally, Jahed *et al.* [53], experimentally observed a change of the behaviour of the resistivity as a function of the deposited power for different values of the argon pressure. The lowest resistivity was obtained at 0.5 mTorr using a sputtering power of 150 W.

The impact of the **deposition thickness t** [nm] was also investigated by Man Nie *et al.* [57]. They observed a decreasing of the electrical resistivity of one order of magnitude

followed by a saturation of this one at 7.5×10^{-4} Ω cm for thickness higher than 55 nm. The deacresing of the resistivity as the thickness increases is due to an improvement of the crystallinity as the film grow. The RMS roughness of the thin film also increases of two order of magnitudes (0.1 nm to 10 nm) with the thickness increasing (33 to 550 nm). Rahamane *et al.* [42] also performed a complete investigation of the thickness impact on the thin film physical properties. A saturation of the resistivity and the band gap energy E_g respectively at 10^{-3} Ωcm and 3.33 eV is observed over 50 nm. Moreover, an increasing of the thickness leads to a decreasing of the mechanical stress due to the deposition on the substrate which improve the crystallinity. In the visible wavelength range, the transmittance measurements were over 90 %. However, as the thickness increases, the opacity of the films also increases in the infrared region. High argon pressure deposition could lead to an increasing of the resistivity due to diffusion of atmospheric oxygen in the AZO layers.

The impact of **the aluminium oxide Al_2O_3 percentage** [%] within the zinc oxide semiconductor material was also studied by Cornelius [54] *et al.* and by J.F. Chang *et al.* [49]. Cornelius observed an decreasing of the resistivity from 20 to 2×10^{-4} Ωcm due to mainly an increasing of the free carrier mobility from 7 to 46.6 [$cm^2V^{-1}s^{-1}$] when the Al_2O_3 percentage decreases from 8.7 to 1.7 %. The same observation was performed by S.H. Jeong *et al.* [58] at room temperature. However, for higher deposition temperature, the behaviour of the resistivity as a function of the Al_2O_3 percentage changes and a minimum of this one is found at 6 %. The transmittance is not clearly impacted by the Al_2O_3 concentration and the energy band gap increases as the concentration increases. Consequently, a percentage of 2 % of Al_2O_3 seems appropriate for the AZO deposition.

Some experimental research groups such as Cornelius *et al.* and Jeong *et al.* [54, 59] also studied the influence of the **proportion of oxygen O_2** [%] compare to the argon proportion. Cornelius highlighted the fact that an increasing of the oxygen pressure from 4.5×10^{-2} mTorr to 6.75×10^{-2} mTorr leads first to a slight decrease of the order of 10^{-4} Ωcm and then to an increase of the electrical resistivity. The proportion of oxygen O_2 does not seem to play an important role in the electrical properties of the AZO deposited layer.

Finally, **post-annealing process** such as RTA were performed by J.F. Chang *et al.* [49] on the previously deposited AZO layers. The post-thermal treatment in vacuum atmosphere seems to reduce the electrical resistivity of the layer as a function of the annealing temperature. The higher the temperature the lower the resistivity. Concerning the annealing time, a saturation of the resistivity occurs after 20 minutes. Concerning these information, a thermal treatment of the pre-deposited layers could be performed. However, a special attention has to be given to the annealing atmosphere and the thermal energy released to the layer. Indeed, Tong *et al.* [60] performed a comparative study of the post-deposition RTA depending on the atmosphere used. They observed an improvement of the thin film conductivity for RTA in hydrogen atmosphere and a degradation of the electrical properties for nitrogen and air atmosphere.

Chapter 4

Tools and Methodology

In this chapter, the tools and the protocols used to characterise the thin films and the junction determined are presented and described. The full study of the physical properties requires an electrical (cfr. Section 4.1) and an optical (cfr. Section 4.2) characterization of the layers as well as of the device elaborated. For each experimental technique, the theoretical background is presented in order to provide the reader a description of the physics behind the experimental measurement. The experimental protocols used for each characterization are developed and the choices of the parameters used for each measurement are presented and justified.

Main results and concepts presented and explained in this chapter:

- The electrical characterization of Cu_2O:Mg and ZnO:Al independent thin films allows to determine the majority carrier concentration n, p [cm^{-3}], the resistivity ρ [Ωcm] and the charge carriers mobility μ_n, μ_p [$m^2V^{-1}s^{-1}$] related to these majority carriers thanks to the VdP and Hall measurement methods [61, 62]. Then the rectifying behaviour of the junction is studied via a current-voltage measurement of the PN-junction.
- The optical characterization of Cu_2O:Mg and ZnO:Al independent thin films allows to determine a quantitative measurement of the transparence of the thin films. The measurement of the transmittance $\mathcal{T}$ [%] in the visible spectrum [200-2000 nm] allows to check the validity of the layer as TED. The band gap energy of each semiconducting layer is also determined thanks to calculation of the absorption coefficient α [cm^{-1}] (cfr. Chapter 2) based on the transmittance. Finally the energy measurement of the emitted spectrum is performed to quantify the efficiency and the intensity of the LED.
- The morphological characterization of the thin films is performed using a SEM (cfr. Section A.1). This one allows particularly to obtain high magnification and resolution images in order to observe the crystallinity of the layers in comparison to the Thornton' structure zone-model presented in Chapter 3. Then, using a profilometry measurement the thickness of the film is determined and used in the absorption coefficient and electrical resistivity calculations.

4.1 Electrical Characterization

In order to obtain the electrical characteristics of the thin films fabricated thanks to the PVD deposition process presented in Chapter 3 two measurement methods are realised. The Van der Paw (VdP) measurement established by L.J. Van der Paw (VdP) in 1958 [61] combined with a Hall effect measurement discovered in 1879 by Edwin Herbert Hall [62] are performed. These measurements allow to determine the electrical resistivity ρ of the majority carriers, the doping type of semiconductor, the sheet carrier densities n_S (resp. p_S) of the majority carriers and the majority carriers mobility μ_n (resp. μ_p) in the n-type (resp. p-type) deposited layer. The knowledge of these physical quantities are required in order to select the optimum deposition parameters which will be used for the fabrication of the PN-junction.

Finally the electrical characterization of the PN-junction, the current density-voltage characteristic of the heterostructure is determined in order to confirm the rectifying behaviour of the junction.

4.1.1 Van der Paw and Hall Measurements

VdP and Hall measurements are two independent procedures used in the same experimental protocol to electrically characterize a thin film. First of all, the resistivity ρ of the semiconducting material is determined by measuring the sheet resistance of the layer R_{sheet} using a four-points measurement method. The sheet resistance can be defined as the resistance of a layer which has an uniform thickness t. The term sheet resistance refers to a resistance of a two-dimensional system. In other words, the current lines are assumed to travel only in a planar direction and not in the perpendicular direction of the film surface.

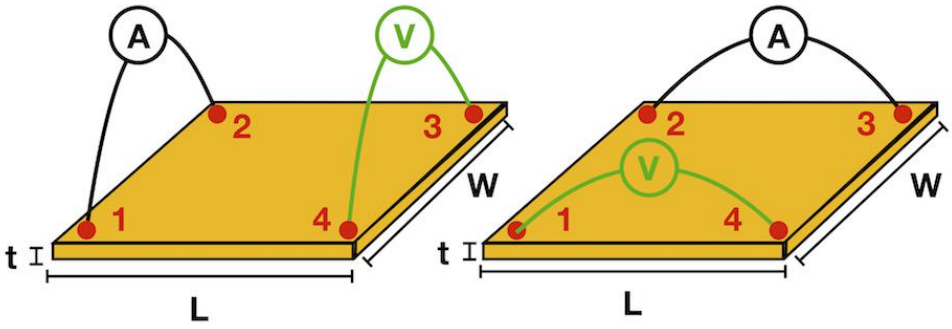

Fig. 4.1: Representation of the VdP measurement technique used in order to determine the sheet resistance R_{sheet}. This technique consists in a four points measurement by successive measurements of the voltage potential and the injected current at interchanging corner points of the thin film.

As represented in Fig. 4.1, a current is injected between two points at the corner of the sample and the voltage is measured at the two opposite points. Using Ohm's law, Eq.(4.1) and (4.2) are obtained.

$$R_{12,34} = \frac{V_{34}}{I_{12}} \qquad (4.1) \qquad \text{and} \qquad R_{23,41} = \frac{V_{23}}{I_{41}}, \qquad (4.2)$$

where $R_{12,34}$ corresponds to the resistance measured when a current I_{12} [A] is injected between corners number 1 and 2 and the potential drop V_{34} is measured between corners 3 and 4 as represented in the schematic illustrations of the measurement in Fig. 4.1. Then, in his 1958's paper [61] VdP established a relation between the resistance measured using the four-points measurement and the sheet resistance of the thin film (cfr. Eq.(4.3)).

$$e^{-\pi R_{12,34}/R_{\text{sheet}}} + e^{-\pi R_{23,41}/R_{\text{sheet}}} = 1 \qquad (4.3)$$

Using this relation, the sheet resistance of the thin film is extracted and the resistivity of the material is calculated as the sheet resistance multiplied by the thickness of the thin film (cfr. Eq.(4.4)). The resistivity determined is an intrinsic property of the studied material. Indeed the resistivity does not depends on the geometrical parameters involved in the resistance calculation (cfr. Eq.(4.5)).

$$\rho = R_{\text{sheet}}\ t \qquad (4.4) \qquad \text{and} \qquad R = \rho\ \frac{L}{Wt}, \qquad (4.5)$$

where L and W are respectively the length and the width in the planar direction of the studied sample (cfr. Fig. 4.1).

In order to realise this measurement, the sample is placed on a support (cfr. Fig. 4.1c) where thin wires with a low resistivity (10^{-5} Ωcm) are placed on the four contacts available at the corner of the support. Then, the sample is placed at the centre of four points and metallic contacts are realised onto the end corners of the sample by applying a meticulously a small point of silver paste in order to unify the platinum filament with the sample' surface. After this operation, the silver paste is left drying 15 minutes in order to have a solid contact. Several precautions have to be taken into account in order to realise a good measurement:

- The sample must have an uniform thickness. Indeed the resistivity is determined by dividing the sheet resistance by the thickness which is assumed to be constant overall the thin film.

- The contact must be small at least one order of magnitude smaller than the sample size. In order to obtain a perfect measurement, the metallic contacts should be infinitely small. The error induces by the contact size vary has the diameter of the contact over the distance between two contacts in the measurement.

- A consequence of the previous point is that the contacts must be placed at a equidistant distance at the extreme corners of the sample. These ones must also have the same shape.

In order to perform an accurate VdP measurement, an optimum current has to be found. The higher the resistance of the film, the lower the injected current. Finally, the advantage of this four-probe measurement compare to a classical two-probes measurements is the exclusion of the contact resistance which are generally unknown and can lead to experimental issues.

Once the intrinsic electrical resistivity of the semiconducting material is measured, the Hall measurement is performed. This one is based on the Hall effect phenomenon in which a voltage difference appears between the sides of the samples due to the influence of the combined effect provided by a magnetic field applied perpendicularly to the direction of the injected current.

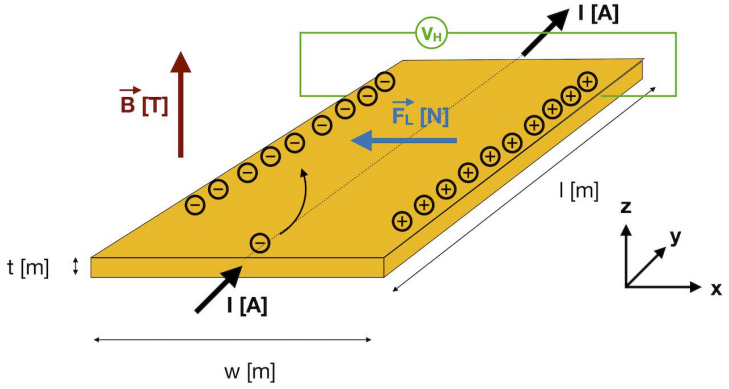

Fig. 4.2: Schematic representation of the Hall effect phenomenon. The magnetic field **B** and the injected current I induce a Lorentz force $\mathbf{F_L}$ in the left direction (for electron) which lead to the generation of a Hall voltage V_{H}.

As it can be seen in the Fig. 4.2, when the magnetic field **B** is applied along the z-axis, charge carriers injected in the materials experienced a Lorentz force $\mathbf{F}_L$ given by Eq.(4.10):

$$\mathbf{F_L} = q\ (\mathbf{E} + \mathbf{v} \wedge \mathbf{B}), \tag{4.6}$$

where **E** is the resulting electric field applied on the system which has a component along the y-axis due to the current injection *et al.*ong the x-axis due to the electric field induced. By reworking the current density equation (cfr. Eq.(4.7)), the charge carrier velocity can be determined (cfr. Eq.(4.8)). Then the electrostatic force resulting of the Hall potential is given by the charge of the carrier times the Hall potential divided by the length on which the voltage drop takes place which is equal to the elementary charge times the induced electric field E_x (cfr. Eq.(4.8)).

$$J_{\mathrm{drift},y} = \frac{I_y}{wt} = q\ v_{\mathrm{drift},y}\ n \tag{4.7}$$

$$\leftrightarrow v_{\mathrm{drift},y} = \frac{I_y}{nqwt} \tag{4.8}$$

and

$$F_{e,x} = \frac{q\ V_{\mathrm{H}}}{w} = -q\ E_x \tag{4.9}$$

By inserting Eq.(4.8) and (4.9) into the Lorentz force equation (cfr. Eq.(4.10)), under steady-state conditions along the x-axis as described in Fig. 4.2:

$$\frac{V_{\mathrm{H}}}{w} = v_y B_z \tag{4.10}$$

The Hall voltage can be deduced by replacing the drift velocity along the y-axis (cfr. Eq.(4.11)). In this equation, all the physical quantities are known except the majority

charge carrier concentration. Indeed, the current I is measured, the magnetic field applied is equal to 0.6 T, q is the elementary charge and the thickness of the film is previously measured. Consequently, the majority carrier concentration in the doped semiconductor layer is obtained using Eq.(4.11).

$$V_{\mathrm{H}} = \frac{I_y \; B_z}{n \; q \; t} \tag{4.11}$$

In order to determine the information about the doping type of the semiconductor, the Hall coefficient R_{Hall} is determined according to Eq.(4.12) in which $R_{13,24,B_z>0}$ and $R_{13,24,B_z<0}$ have the same signification than the measurements established in Eq.(4.1) and (4.2) respectively for a positive value of the magnetic field along z ($B_z>0$) and a negative value of the magnetic field along z ($B_z<0$). If the Hall coefficient is greater (resp. lower) than 0, it is a n-type doped semiconductor (resp. p-type doped). Indeed, the sign of the Hall coefficient indicates if the charge carriers are negatively charged in the case of electrons as majority carriers or positively charged in the case of holes (absence of electrons) as majority charge carriers.

$$R_{\mathrm{Hall}} = \frac{1}{n \; q} = \frac{t \; [R_{13,24,B_z>0} - R_{13,24,B_z<0}] \; B_z}{2} \tag{4.12}$$

Finally, the majority carrier mobility is determined using the majority carrier concentration with the definition of the resistivity determined in the VdP measurement (cfr. Eq.(4.13)).

$$\rho = \frac{1}{\mu \; n \; q} \tag{4.13}$$

The VdP and Hall measurements are performed using a Phys Tech Hall measurement system RH 2035[1]. The theoretical limits of the electronic facilities are an electrical resistivity between 10^{-5} to 10^{7} $\Omega\mathrm{cm}^{-1}$ and a concentration between 10^{7} to 10^{20} cm^{-3} for a sample thickness of 1 μm. In order to check the reproducibility of the results determined, several measurements are performed on a same sample at the contact points and then by changing them. Thanks to the VdP and Hall measurements, the electrical characterization of the thin film is performed. In the following part of this section, the electrical characterization of the junction is described.

4.1.2 Current Density-Voltage Characteristic

This last part is dedicated to the characterization of the PN-junction fabricated. In order to check the rectifying behaviour of this one, a measurement of the total current density J [A m^{-2}] as a function of the bias applied is realised at room temperature using a two-points measurement protocol. In order to get rid off the geometry of the device, the current density J is used over the current itself. To do so, as it can be seen in Fig. 4.3, metallic contacts are deposited at the top of the heterostructure to ensure a low interface resistance between the tin wires of the sample holder and the junction. Nevertheless, the behaviour of the interface metallic contact/semiconductor could lead to a Schottky contact [23][2]. In this work, all interfaces other than the semiconductors

[1]Further information on the device can be found at the following reference: `http://www.phystech.de/products/hall/hl2035.pdf` consulted on April 12, 2018.

[2]Cfr. Streetman reference [23]: Chapter 5: "Junctions".

interface (FTO/semiconductor and metallic contact/semiconductor) are expected to be ohmic ones. The current-voltage curve determined is then post-treated by dividing the current by the surface of the metallic contact.

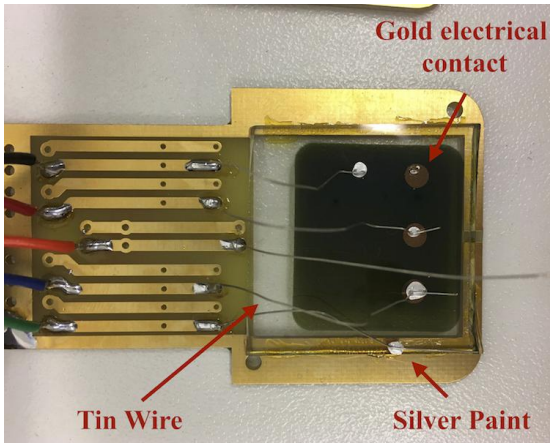

Fig. 4.3: Photography of the PN-junction holder realised in order to characterize electrically this one.

In addition, several effects can lead to a deviation of the ideal I-V characteristic presented in Chapter 2 [4]. First, the interface between both semiconductors can be modelled by a diode electrical circuit. Then, the current composed of free charge carriers travelling through the neutral region within the semiconducting materials encounter scattering events which can be modelled by an additional series resistance to the diode electrical circuit (cfr. Fig. 4.4a). This series resistance lead to a linear behaviour of the I-V characteristic for high applied bias. The leakage currents due to conductive channel through the depletion region can be modelled by a additional parallel resistance (cfr. Fig. 4.4b). These effects can be auditioned to each other (cfr. Fig. 4.4c).

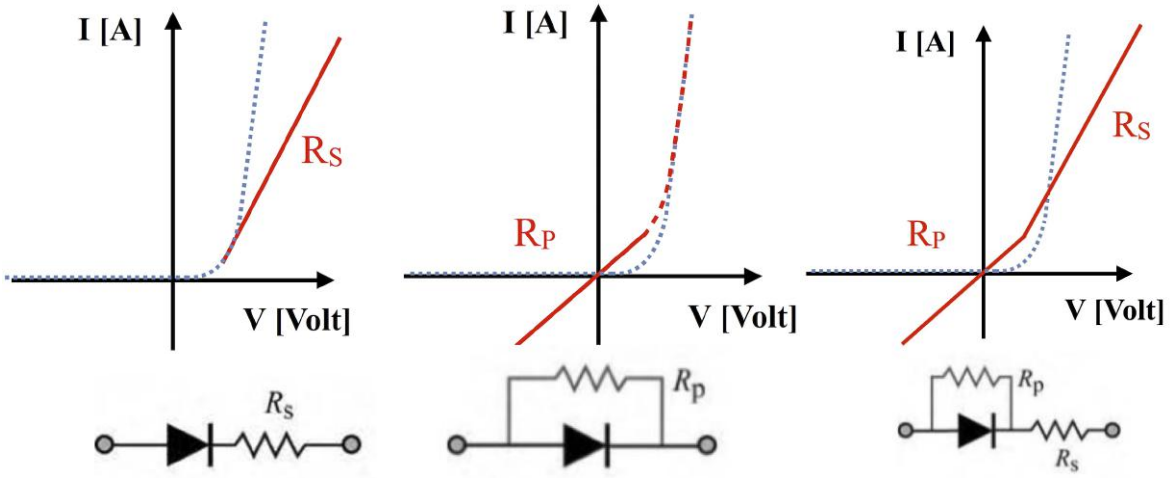

(a) IV-curve effect of series resistance R_S

(b) IV-curve effect of leakage resistance R_P

(c) IV-curve effect of leakage and and series resistances

Fig. 4.4: Non-ideality I-V characteristics due to the resistance experienced by the charge carriers in the semiconducting neutral regions of the PN-junction R_S and due to leakage current R_P.

4.2 Optical Characterization

This section is dedicated to first the optical characterization of the independent Cu_2O:Mg and ZnO:Al thin films determined in order to select the optimum deposition parameters. And secondly to the optical characterization of the heterostructure realised.

The entire optical characterization of the layers and of the heterostructure is performed using the UV-3600 Shimadzu photospectrometer[3] (cfr. Fig. 4.5a). This photospectrometer is made of three different detectors consisting of different materials with an optimum efficiency in a specific wavelength range (cfr. Fig. 4.5b).

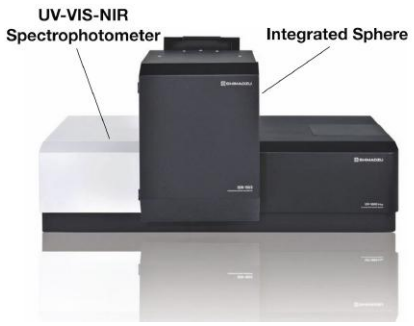

(a) UV-3600 UV-VIS-NIR Shimadzu photospectrometer.

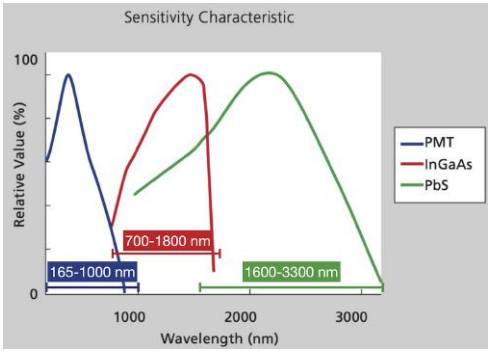

(b) Efficiency of the UV-3600 Shimadzu photospectrometer three detectors as a function of the wavelength.

Fig. 4.5: (a) Photography of the UV-3600 Shimadzu photospectrometer and the integrated sphere used in the SPIN research group. (b) Efficiency of the UV-3600 Shimadzu photospectrometer three detectors (Photomultiplier (PMT), InGaAS and PbS) as a function of the wavelength.

4.2.1 Transmittance Measurement

As presented in Fig. 4.6, the transmittance measurement is a direct measurement method. The sample incident light beam impact orthogonally the sample. The photospectrometer is made of a lamp compartment from which the incident beam is emitted by a lamp source. The beam first go through a slit of adjustable width W_{slit}. Then, the light is reflected onto a reflective blazed diffraction grating which selects the wavelength of the incident beam. Thanks to an accurate mechanical system, the wavelength step can be selected. Finally, the beam go through an exit slit and enter into the sample compartment. The incident beam interact with the sample and the transmitted beam is captured by the most efficient detector based on the wavelength range studied (cfr. Fig. 4.5b). The scanning speed consisting in the detection time for a particular wavelength can also be fixed.

[3]Further information on the device can be found at the following reference: `https://www.shimadzu.com/an/molecular_spectro/uv/uv-3600plus.html` consulted on April 12, 2018.

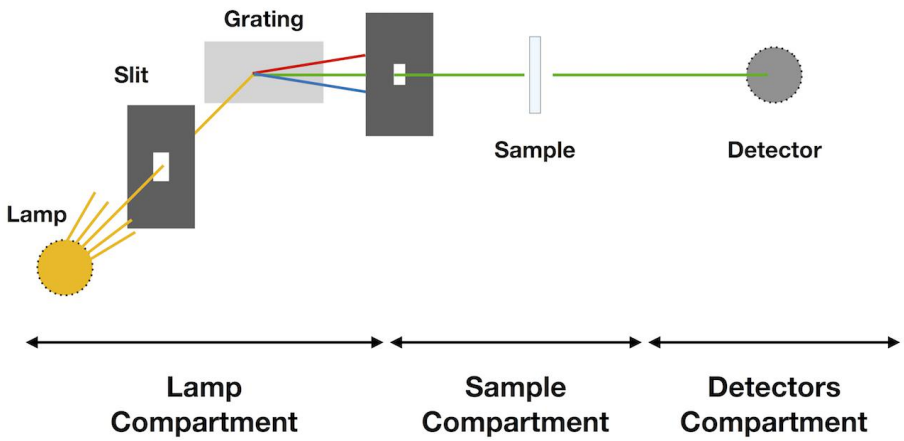

Fig. 4.6: Simplified scheme representing a direct measurement method perform using the UV3600 Shimadzu photospectrometer.

Before each measurement, the baseline is performed by placing the mechanical mask in the sample compartment at the exact position of the measurement. The baseline is taken as reference for the measure to come. Then, a glass substrate is measured and compare to literature results. The glass transmittance over 300 nm is around 92% (4% of reflectance at each interface air/glass). If the glass measurement is conclusive, thin film measurements are performed. For each film, the transmittance measurement is taken several times at the same location on the sample and several times for different samples locations. The experimental parameters are presented in Tab.4.1.

Transmittance Measurement Parameters	**Value/Expression**
Scanning speed	Medium
Wavelength step	2 nm
Wavelength range	[200 nm ; 2000 nm]
Measurement Mode	Direct
Detector Gain	0
Slit Width	3 nm

Tab. 4.1: Experimental parameters used in order to determine the transmittance of the thin films deposited.

Regarding the direct measurement of the transmittance, the sample is placed in the sample compartment and an incident beam of intensity $\mathcal{I}_{\prime}$ is generated by the lamp source of the machine. The beam goes through the sample. One part of the incident light beam is reflected (reflectance $\mathcal{R}$), another one is absorbed (absorptance $\mathcal{A}_{\text{abs}}$) and the last part is transmitted (transmittance $\mathcal{T}$) (cfr. Eq.(4.14)).

$$1 = \mathcal{R} + \mathcal{A}_{abs} + \mathcal{T} \tag{4.14}$$

As described in Eq.(4.15), the transmittance $\mathcal{T}$ is defined as the ratio between the intensity of the incident light beam $\mathcal{I}_0$ known by the photospectrometer and the intensity of

the transmitted light beam $\mathcal{I}$ arriving to the detector as described in the Beer-Lambert's law (cfr. Eq.(2.56)).

$$\mathcal{T} = \frac{\mathcal{I}}{\mathcal{I}_0} \qquad (4.15) \qquad \text{and} \qquad \mathcal{A} = \log_{10} \frac{1-\mathcal{R}}{\mathcal{T}} \qquad (4.16)$$

Then, as expressed in Eq.(4.16), the absorptance is a logarithmic transformation of the one minus the reflectance times the inverse of the transmittance. The reflectance is calculated using the refractive index of the thin film studied and the refractive index of the experimental environment (cfr. Eq.(4.17)). In our case n_0 is the refractive index of the air equals to 1.

$$\mathcal{R} = \left(\frac{n-n_0}{n+n_0}\right)^2 \qquad (4.17) \qquad \text{and} \qquad \alpha = \frac{1}{\log_{10} e} \frac{\mathcal{A}}{t} \qquad (4.18)$$

For thin films, the absorption coefficient is defined by Eq.(4.19). Where t is the thickness of the deposited film. The band gap energy is finally determined by plotting the square of the absorption coefficient α^2 as function of the energy [eV]. Indeed, as explained in Chapter 2 the absorption coefficient one is directly related to photon absorption and consequently to the band gap energy E_g (cfr. Eq.(2.56)).

$$\alpha = A_{SC} \sqrt{E - E_g}, \qquad (4.19)$$

where A_{SC} is a constant related on the semiconducting material. At this point, the optical characterization is completed. The transmittance and the bang gap energy of the thin films are determined. The next part of this section focus on the characterization of the PN-junction thanks to an energy measurement of the emission spectrum.

4.2.2 Emission Spectrum Energy Measurement

The optical characterization of the PN-junction manufactured implies the energy measurement of the emission spectrum. This energy measurement protocol is divided in two steps. First, the total energy of the radiation emitted by the LED fabricated is performed using the ISR-1503/ISR-1503F large integrating sphere[4] from Shimadzu (cfr. Fig. 4.5a). The integration sphere presents a Spectralon[5] coating enabling the energy measurement.

In order to perform this first measurement, the LED is placed at the top of the integration sphere in the sample compartment and the measure is performed without the grating (this one is located before the sample compartment). This step allows the acquisition of the total energy emitted by the forward bias PN-Junction.

The second measurement is performed by placing the LED in the lamp compartment. The lamp source of the photospectrometer is switched off and the incident light beam entering the sample compartment comes consequently from the LED biased with an external potential V_{app}. Thanks to this second measurement in a direct mode, the

[4]Further information on the device can be found at the following reference: `https://www.shimadzu.com/an/molecular_spectro/uv/uv-3600plus.html` consulted on April 12, 2018.

[5]Further information on the device can be found at the following reference: `https://www.labsphere.com/labsphere-products-solutions/materials-coatings-2/targets-standards/diffuse-reflectance-standards/diffuse-reflectance-standards/` consulted on April 12, 2018.

energy spectrum is determined. The experimental parameters used to realise this second measurement are presented in Tab.4.2.

Energy Measurement Parameters	**Value/Expression**
Scanning speed	Slow
Wavelength step	1
Wavelength range	[500 nm ; 620 nm]
Measurement Mode	Direct
Detector Gain	7
Slit Width	3 nm

Tab. 4.2: Experimental parameters used in order to determine the transmittance of the thin films deposited.

However, due to the fact experimental limitation of the photospectrometer, the integrated sphere and the grating cannot be used for the same measurement. In order to determine a good insight of the emission spectrum determined, the emission spectrum measured at the second step of this protocol is integrated over the wavelength range measured. This value is divided by the total energy measured at the first step of this protocol in order to determine a ratio. Finally, the emission spectrum curve is divided by this ratio. Consequently, the integration of the emission spectrum match with the total energy determined.

Chapter 5

ZnO:Al/Cu_2O:Mg Heterostructure: Numerical Simulations

This chapter is dedicated to the numerical simulation of the PN-junction structure by solving the basic semiconductor equations with specific materials inputs related to Cu_2O:Mg and ZnO:Al semiconductors physical properties. The results of the numerical simulations such as the band diagram, the charge carrier concentrations, the current density-voltage curve and the emission spectrum are presented, interpreted and discussed by taking into account the numerical errors and limitations.

Main results and concepts presented and explained in this chapter:

- The presentation of the numerical code implemented to solve the problem of a PN-junction under an external bias V_{app}. Using the basic semiconductor equations, a spatial discretisation of the system is performed and the equations are first linearised. An iterative refinement of the solution is performed until the targeted precision is achieved or the maximum number of iterations is reached. The initial solution named as a guess solution under thermodynamic equilibrium conditions is initially used based on the boundary conditions applied on the system. The numerical resolution is performed under an external bias V_{app} within -2 V to 3.5 V. The convergence is improved by taking the solution of the resolution of the k^{th}-1 bias applied on the system as guess solution for the resolution of the PN-Junction under the k^{th} value of the external bias.

- First the optimisation of the input parameters such as the doping concentrations in order to satisfy Maxwell-Boltzmann (MB) approximation performed in Chapter 2 corresponding to non-degenerate semiconductors. The analysis of the band diagrams as a function of the applied external bias corroborates the theory of the PN-junction (cfr. Section 2.12). The recombination rates determined confirm the theoretical prediction presented in Section 2.1.3 and the minority charge carrier accumulation due to the heterojunction highlights the improvement of the recombination rate as presented in Section 2.13. The emission spectrum determined gives a luminosity of the order of the candela with an external efficiency of 1% [27] in order to consider the impact of the defects and the extraction efficiency.

5.1 Numerical Resolution

5.1.1 Basic Semiconductor Equations

In this section the semiconductor equations used to numerically simulate the Cu_2O:Mg/AZO PN-junction are presented and briefly described. This section goal is to describe the physics behind the numerical code without developing any equations or presenting any demonstrations. For further information, the development of these ones can be found in [22]. The equations presented in this section compose the "basic semiconductor equations" derived from the Maxwell's equations. They can be applied with any semiconductor materials without any specific hypothesis.

$$\nabla \cdot (\epsilon \ \nabla V) = q \ (p + N_D - n - N_A - N_{\mathrm{T}}) \tag{5.1}$$

First of all, Eq.(5.1) is the **Poisson's equation**. This one is used to describe the relation between the electric potential and the electric charge density distribution. The charge density contributions can be free charge carriers such as electrons, holes or space charges such as donor or acceptor dopant atoms. The presence of electrons or holes on trap levels within the band gap also participate to the total charge density. This relation is modulated by the electric permittivity of the material $\epsilon = \epsilon_0 \ \epsilon_{\mathrm{r}}$ which can be defined as a measure of the ease to create an electric field in a particular medium. $\epsilon_0 = 8.85 \times 10^{-12}$ F m^{-1} is the vacuum permittivity and ϵ_r the relative permittivity of the medium.

$$\frac{\partial n}{\partial t} = \frac{1}{q} \ \nabla \cdot \mathbf{J_n} - c_{\mathrm{n}} n (N_{\mathrm{T}} - n_{\mathrm{T}}) + e_{\mathrm{n}} n_{\mathrm{T}} + B(np - n_{\mathrm{i}}^2) = 0 \tag{5.2}$$

$$\frac{\partial p}{\partial t} = \frac{-1}{q} \ \nabla \cdot \mathbf{J_p} - c_{\mathrm{p}} p n_{\mathrm{T}} + e_{\mathrm{n}} (N_{\mathrm{T}} - n_{\mathrm{T}}) + B(np - n_{\mathrm{i}}^2) = 0 \tag{5.3}$$

$$\frac{\partial n_{\mathrm{T}}}{\partial t} = c_{\mathrm{n}} (N_{\mathrm{T}} - n_{\mathrm{T}}) - e_{\mathrm{n}} n_{\mathrm{T}} - c_{\mathrm{p}} p n_{\mathrm{T}} + e_{\mathrm{n}} (N_{\mathrm{T}} - n_{\mathrm{T}}) = 0 \tag{5.4}$$

Equations (5.2), (5.3) and (5.4) are respectively the **continuity equations** for electrons, holes and electrons on trap levels. In these equations, c_{n} and c_{p} corresponds respectively to the capture coefficient for electrons and holes which are defined as the product of the capture cross section for electron and holes σ_n and σ_p and their respective thermal velocities $v_{\mathrm{th},n}$ and $v_{\mathrm{th},p}$. e_{n} and e_{p} corresponds respectively to the emission rate [m^{-3} s^{-1}] for electrons and holes. B is the bimolecular rate described in Chapter 2. These equations are solved in the stationary case and they come directly from the charge conservation equation which expresses the fact that a modification of the charge carrier density at a given point in the system induces a motion of charge carriers $\nabla.\mathbf{J}$ (cfr. Eq.(5.5)). In addition to this term, recombination with traps with a rate c_n for electron (resp. c_{p} for holes) depending on the thermal velocity and the capture cross section are considered. Thermal emissions from trap levels with a rate e_n are also taken into account. And $B(np - n_{\mathrm{i}}^2)$ is the radiative recombination term developed in the previous chapter (cfr. Eq.(2.20)).

$$\nabla \cdot \mathbf{J} + \frac{\partial \rho}{\partial t} = 0 \tag{5.5}$$

Equations (5.6) and (5.7) are respectively the **transport equations** for electrons and holes. These equations are deduced from the Boltzmann's transport equation [22]. The charge carrier current density can be induced by an electric field (drift current density seen in Section 2.2.1) resulting of the electric potential created by an electric charge density (cfr. Poisson Eq.(5.1)). Or it can be induced by a gradient of charge carrier concentration which induces charge carriers diffusion (diffusion current density seen in Section 2.2.1).

$$\mathbf{J_n} = qn\mu_n\mathbf{E} + qD_n\nabla n \tag{5.6}$$

$$\mathbf{J_p} = qp\mu_p\mathbf{E} - qD_p\nabla p \tag{5.7}$$

In the next section, a succinct description of the numerical approach used to modelize the heterostructure is performed. Furthermore, in order to simulate the semiconductor with the previous equations in a simple model, several assumptions are performed such as non-degenerate semiconductor (reasonable doping), constant temperature overall the lattice, harmonic approximation of the energy band for effective masses and the PN-junction is assumed to be infinitely large.

5.1.2 Discretisation, Scaling and Iterative Scheme

The problem is solved in a one-dimensional system. In order to do so, a geometrical discretisation is performed using a 1D-mesh with a discrete number of points. The distance between two points of the mesh is defined as h_i and depends on the point. Indeed the mesh is not uniform in order to increase the resolution of the solution at some interest points. For instance, the refinement of the mesh increase gradually close to the interface between the p-type and n-type semiconductors (as shown in Fig. 5.1) because in this region, the variation of the unknown function at different position changes drastically. This discretisation is done in order to approach the system behaviour of a continuous one with a reasonable calculation time. Once this geometrical discretisation is performed, the resolution of the problem take place at each point of the mesh which corresponds to a position along the x-axis in the PN-junction.

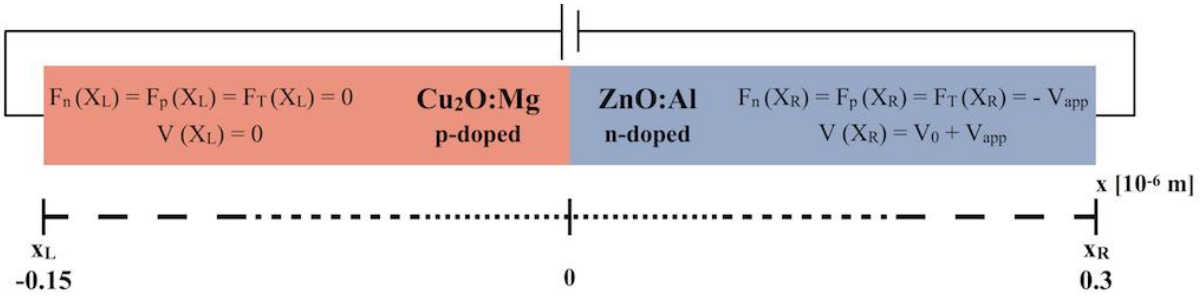

Fig. 5.1: Schematic representation of the PN-junction numerical problem. The refinement of the mesh increases gradually close to the interface due to a drastic change of the solution close to the junction. All variables parameters (V, F_n, F_p, F_T) are set to 0 at x_L and depends on the applied external bias V_app on x_R.

The resolution used the equations presented in Section 5.1.1. Injecting the transport equations (cfr. Eq.(5.6) and (5.7)) in the continuity equations (cfr. Eq.5.2 and (5.3)) additionally to the Poisson equation (cfr. Eq.(5.1)) leads to a system of four coupled non-linear partial differential equations. The one-dimensional configuration implies that all partial derivatives perpendicular to the x-axis are equal to zero.

Furthermore, these equations couple four functions of space and time: the electric potential V, the concentration in electrons n, the concentration of holes p and the concentration of electrons located in trap levels n_{T}. Using relations (2.7) and (2.8), n, p and n_{T} can be reexpressed by respectively, the quasi-Fermi level corresponding to each physical quantities and the conduction band energy E_{C}, the valence band energy E_{V} and the trap levels energy E_{T} (cfr. Eq.(5.8), (5.9) and (5.10))

$$n = N_{\mathrm{C}}\ e^{\frac{-E_{\mathrm{C}}-F_{\mathrm{n}}}{k_B T}} \tag{5.8}$$

$$p = N_{\mathrm{V}}\ e^{\frac{F_{\mathrm{p}}-E_{\mathrm{V}}}{k_B T}} \tag{5.9}$$

$$n_T = \frac{N_t}{1\ +\ g_T\ e^{\frac{E_T-F_T}{k_B T}}} \tag{5.10}$$

Note that in Eq.(2.7), (2.8) the quasi-Fermi levels for the holes, electrons and electrons on trap levels are aligned. Indeed it is the case under thermodynamic equilibrium conditions.

When an external bias is applied V_{app} on the system, this one is consequently out of equilibrium and quasi-Fermi levels must be defined for each quantity. These ones corresponds to the Fermi levels of the independent semiconductors of the system considering as if they were under thermodynamic equilibrium conditions. The dependent parameters are consequently (V, F_{n}, F_{p}, F_T) [22].

Finally, a scaling of the physical parameters is performed in order to improve the numerical behaviour of the resolution. This manipulation is nothing else than a mathematical trick which is corrected when the results are written in the output files. For instance, all distance are set in meter, the scaling divide each one of them by a factor 10^6 and is propagated to all related physical quantities. The inverse operation is performed in order to obtain the final values.

The last step consists in the linearisation of the non-linear system and the iterative refinement of the solution. The approach used is the finite-difference method. In this method, the differential equations are approximated by performing the difference between two nearest points in the discretizing mesh. In order to do so, an initial guess value of the solution is required. This one is taken as the boundary conditions applied on the system as shown in Fig. 5.1.

It is assumed that the quasi-Fermi levels F_{n}, F_{p} and F_T take their equilibrium values

and are consequently equal far from the junction[1]. However, depending on the diffusion length of the charge carrier, the electric field and the charge concentrations, the quasi-Fermi levels may not have reached their equilibrium yet. The electric potential at the left boundary is considered as the ground and the electric potential at the right boundary is taken as $\mathrm{V}(x_{\mathrm{R}}) = \mathrm{V}_0 + V_{\mathrm{app}}$. This particular guess solution is used when $V_{\mathrm{app}} = 0$. For an non-zero applied external bias on the system, the guess solution in order to resolve the PN-junction numerical problem is the solution of the problem at the previous iteration of the bias applied. This method allows to decreases the number of iterations before reaching the convergence.

According to this initial solution, the iterative resolution of the problem takes place. A final solution is achieved if one of the two conditions is fulfilled:

- The targeted accuracy is reached and in this case, the difference between the solution at the step k and the step k+1 is lower than the setting accuracy tolerance.
- The maximum of iterative steps have been reached. In this case, it is considered that the converged solution will not be achieved.

In the following section, the numerical results determined using the method described here are presented and interpreted based on the theoretical background determined in Chapter 2.

[1]Here "far" from the junction is taken as the distance for which the electric potential becomes constant over the position.

5.2 Numerical Results

In this section, the numerical inputs used to resolve the problem of the PN-junction are presented. Then, the numerical convergences are analysed and the numerical results are explained and interpreted based in the theoretical background determined in Chapter 2. Table. 5.1 shows the numerical inputs used in order to solve the problem of the PN-junction without considering defects levels within the band gap. This resolution is performed for an applied external bias V_{app} between -2V to 3.5V with a step of 0.5V.

Side	n [cm^{-3}]	p [cm^{-3}]	μ_n [$\text{cm}^2\text{V}^{-1}\text{s}^{-1}$]	μ_p [$\text{cm}^2\text{V}^{-1}\text{s}^{-1}$]	$m_n^\star/m_\text{e}$	$m_h^\star/m_\text{e}$
Cu_2O:Mg	10^{10}	5.52×10^{17}	0.39	0.19	0.99	0.58
ZnO:Al	1.46×10^{17}	10^{10}	0.39	0.19	0.24	0.58
Side	E_g [eV]	N_T [cm^{-3}]	$\text{N}_{\text{T,int}}$ [cm^{-3}]	σ [cm^2]	B [cm^3s^{-1}]	ϵ_r
Cu_2O:Mg	2.09	10^9	10^9	10^{-21}	2×10^{-11}	16.3
ZnO:Al	3.39	10^9	10^9	10^{-21}	2×10^{-11}	16.3

Tab. 5.1: Input parameters of the PN-junction numerical simulation without considering defect levels within the band gap.

In the framework of the one-dimensional numerical resolution of the PN-junction, the first input parameter is the charge carrier concentrations n_n, n_p, p_p and p_n under thermodynamic equilibrium conditions at 300 K. As motivated in Section 2.3, doping levels in TCO must be sufficiently high in order to obtain low electrical resistivity. As a consequence, the resulting semiconductor media are often degenerate. However, one of the assumptions of this numerical simulations is the non-degenerescence of the semiconducting materials. Therefore, to work with a numerical model as close as possible of a real device, the charge carrier concentration are chosen in order to get the Fermi level at $3\text{k}_B\text{T} = 0.0734$ eV of the conduction band energy E_C (resp. of the valence band energy E_V) for the n-side (resp. p-side)[2]. Indeed, carrier concentrations are linked to these energy differences by Eq.(2.7) and (2.8). The first step to determine the maximum charge carrier concentration which can be used within the MB approximation, is to calculate N_C and N_V for a given value of the electrons and holes effective masses in both sides (cfr. Eq.(2.7) and (2.8)) . According to [63], experimental values of electrons effective mass $m_n^\star$ and holes effective mass $m_h^\star$ in Cu_2O are respectively 0.99 m_e and 0.58 m_e. While according to [64], in ZnO, $m_n^\star$ and $m_h^\star$ are 0.24 m_e and 0.58 m_e, with $\text{m}_e = 9.109\ 10^{-31}$ kg, the free electron mass. Using these values, in zinc oxide, $N_\text{C} = 2.95\ 10^{18}\ cm^{-3}$ and $N_\text{V} = 1.11\ 10^{19}\ cm^{-3}$ and in cuprous oxide, $N_\text{C} = 2.47\ 10^{19}\ cm^{-3}$ and $N_\text{V} = 1.11\ 10^{19}\ cm^{-3}$ for a temperature T of 300 K. Using these quantities, the maximum doping concentration in order to stay within the Maxwell-Boltzmann approximation assumed in Chapter 2 are given respectively for AZO and Cu_2O:Mg by Eq.(5.11) and (5.12).

$$n_0 = N_\text{C}\ e^{-(E_\text{C}-E_\text{F})/k_BT} = 1.46 \times 10^{17}\ \text{cm}^{-3} \tag{5.11}$$

[2]The simulation is realized at a temperature of 300°C.

$$p_0 = N_V \, e^{E_F - E_V/k_B T} = 5.52 \times 10^{17} \text{ cm}^{-3} \tag{5.12}$$

The intrinsic concentration in both materials can also be determined using Eq.(2.9) by taking into account the temperature-dependance of the energy band gap. This band gap variation is described by an empirical formula proposed by Varshni [63] (cfr. Eq.(5.13)).

$$E_g(T) = E_g(0) - \frac{A_{fit} T^2}{T + B_{fit}}, \tag{5.13}$$

where A_{fit} and B_{fit} two fitting parameters. The band gap energy of AZO and Cu_2O:Mg at 0 K are respectively 3.43 eV and 2.17 eV [63]. The band gap energy depends on temperature due to the electron phonon coupling. Indeed, as the temperature increases, the vibration of each atom around its equilibrium position is amplified. The interactions between electrons and the lattice are thus temperature-dependent and an increasing temperature leads to a decrease of the energy band gap. For AZO and Cu_2O:Mg, the band gap energies at 300 K.

$$E_{g,AZO}(300) = 3.43 - \frac{5.05 \times 10^{-4} \times 300^2}{300 + 900} = 3.39 \text{ eV} \tag{5.14}$$

$$E_{g,Cu_2O:Mg}(300) = 2.17 - \frac{4.8 \times 10^{-4} \times 300^2}{300 + 275} = 2.09 \text{ eV} \tag{5.15}$$

The band gap energy values of the semiconductors considered here are quite high in comparison to the band gap energy of the silicon (1.14 eV). Indeed, these oxide semiconductors can be considered as insulating materials without doping. For applications purposes of these semiconducting materials as TCOs, high doping levels have to be achieved. Related to these band gap energy values, the intrinsic concentration of both materials at 300 K are:

$$n_{i,AZO} = \sqrt{N_C N_V} \, e^{-E_g/2k_B T} = 1.89 \times 10^{-10} \text{ cm}^{-3} \tag{5.16}$$

$$n_{i,Cu_2O:Mg} = \sqrt{N_C N_V} \, e^{-E_g/2k_B T} = 4.77 \times 10^{1} \text{ cm}^{-3} \tag{5.17}$$

As shown, the values of the intrinsic concentration are definitely in the low range due to the large band gap of these semiconductors. These oxide semiconducting materials are naturally found with impurities atoms, due to their fabrication process, which increase drastically the charge carrier concentration. The intrinsic concentration given in Eq.(5.16) and (5.17) correspond to the intrinsic concentration for pure semiconductors. Regarding, the cuprous oxide, the intrinsic concentration is comparable to the one calculated by Biccari [63].

The simulation of the PN-junction is performed without considering defect levels within the neutral regions or at the interface in order to determine the behaviour of a perfect PN-junction. Nevertheless, the concentrations of electron traps at the interface $N_{T,int}$ [cm^{-3}] and in the neutral regions N_T [cm^{-3}] are set to 10^9 cm^{-3} in order to avoid

any numerical convergence issues implies by setting these ones to 0. These ones are not incorporated into the study but their concentrations are set to negligible values compared to the doping and intrinsic concentrations. For the sake of the study, all recombinations are considered as radiative recombinations. As explained in Section 2.1.3, this assumption is too otpimistic. Indeed, real PN-junctions contain defects which induce additional trap levels within the band gap. Then, the bimolecular rate used in this numerical resolution is based on several values of well-known semiconductors bimolecular rates and is set to 2 10^{-11} cm^3 s^{-1} [27][3]. A capture cross section σ of 10^{-21} cm^2 has been used and electrons and holes mobilities have been respectively set to 0.39 cm^2 V^{-1} s^{-1} and 0.19 cm^2 V^{-1} s^{-1} in both semiconducting materials [22].

We will now focus on the description of the numerical results. As a reminder, the end of the p-side of the junction is set to the ground (cfr. Fig. 5.1) and the bias is applied on the n-side of the junction. As a consequence, a negative bias corresponds to a forward biased junction and a positive bias corresponds to a reverse biased junction. In order to avoid interpretation ambiguities, the following results are presented with a convention where a positive bias corresponds to a forward biased junction and a negative bias, a reverse biased junction. First, we address the quality of the convergence of the iterative process.:

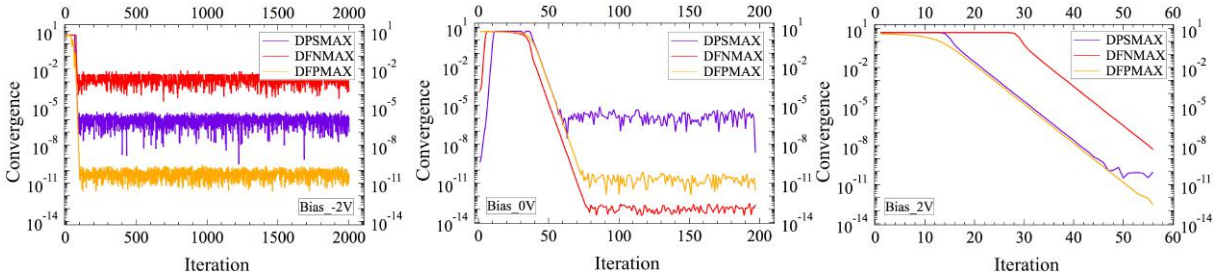

(a) V_{app} = -2 V **(b)** V_{app} = 0 V **(c)** V_{app} = 2 V

Fig. 5.2: PN-junction numerical resolution convergences without considering defect levels within the band gap for an external bias of -2, 0 and 2 V.

In Figure 5.2, the numerical simulations convergences as a function of the number of iterations for an external bias V_{app} of -2, 0 and 2 V are presented. In each graph, the convergences for the quasi-Fermi levels of the holes (DFPMAX), the quasi-Fermi levels of the electrons (DFNMAX) and the electric potential (DPSMAX) are represented. In this numerical resolution the convergence for each physical quantity is calculated as a ratio between the solution at the iteration k and the solution at iteration k-1. In addition, the solution is a table of three unknown functions which all have to converge. For the thermodynamic equilibrium case (V_{app}=0V), the guessed value used is the one presented in Section 5.1, while under an applied external bias, the solution obtained after convergence at the previous bias value is used as the initial guess solution. As shown in Fig. 5.2b, around the 60th iteration, oscillations in the convergences start to appear. This observation shows that no improvement of the numerical resolution occurred over a total number of 140 iterations. Finally, the convergence was achieved after 200 iterations

[3]Bimolecular rates of AlAs, InP, InAs, etc. given in Table 10.1 of Section 10.2: Band-band Recombination.

when the process reached the tolerance value imposed (10^{-8}). In Figure 5.2c, the guessed value used is the solution of the PN-junction problem under an external bias of 1.5 V. As demonstrated in Fig. 5.2c, after several iterations, the tolerance is reached and the convergence is performed within 60 iterations. This case is a good example of the efficiency of this technique in order to ensure the good convergence of the numerical simulation. In the case of calculations for negative bias values, oscillations in the residue start to appear after 100 iterations. It is relevant to note that, the convergence of the quasi-Fermi level associated to the holes and the convergence of the electric potential could be reached while the convergence of the quasi-Fermi level associated to the electrons was more challenging. As described in Section 5.1, the maximum number of iterations is set to 2000. As a result if the tolerance value is not reached, the numerical simulation solutions for the last iteration are consequently used. In the following results, a particular attention has to be brought to the interpretation of the negative biased PN-junction solution. As pointed out previously, at 0 and 2 V, the solution reaches the convergence threshold imposed while at -2 V, the electrons, holes and electric potential convergences are respectively of the order of 10^{-3}, 10^{-10} and 10^{-6}.

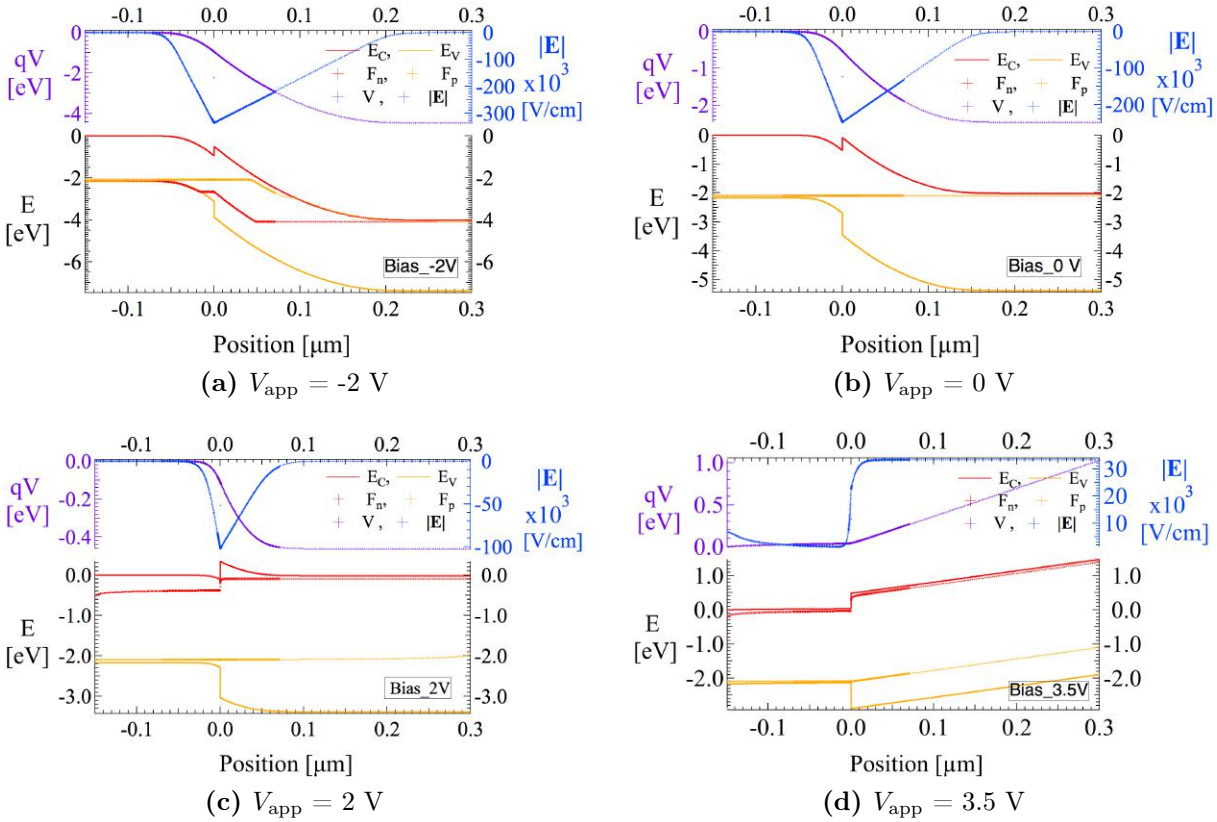

(a) V_{app} = -2 V **(b)** V_{app} = 0 V

(c) V_{app} = 2 V **(d)** V_{app} = 3.5 V

Fig. 5.3: Band diagrams of the PN-junction structure without considering defect levels within the band gap for an applied external bias of -2, 0, 2 and 3.5 V. In those band diagrams, q is equal to -1.602×10^{-19} C.

In Fig. 5.3, band diagrams for an applied external bias of -2, 0, 2 and 3.5 V are presented. In these figures, the electric potential (V) as well as the electric field |**E**| are plotted with independent axes as a function of the position in the PN-junction. The band diagram consists of the traces of the conduction band edge E_{C}, the valence band edge

E_V, the quasi-Fermi levels associated to each semiconductor F_n and F_p as a function of the position in he PN-junction. The whole band diagrams representation as a function of the external potential can be found in Annexe B.

As presented in Fig. 5.3b, the n-side of the junction was extended to a distance of 300 nm from the interface position in order to ensure that bulk-like solutions can be recovered within the computation domain. Indeed, due to both the difference of the electronic affinities[4] and the band gap energies in Cu_2O:Mg and AZO, a jump in the valence band and in the conduction band can be seen. As explained in Chapter 2, this feature leads to a confinement zone for electrons. Indeed, electrons on the n-side have a lower energy than on the p-side where they represent the minority charge carriers. Nevertheless, electrons in this well have to acquire a sufficient amount of energy in order to overcome the energy barrier seen from the p-side. Minority charge carriers are consequently stuck in this confinement zone, which is associated to an increase of their concentration and consequently an increase of the recombination rate (cfr. Eq.(2.19)). Under thermodynamic equilibrium conditions, quasi-Fermi levels are aligned and constant over the entire junction.

The shift between E_C (resp. E_V) and E_F (cfr. Eq.(5.11) and (5.12)) depends directly on the electron concentration in the corresponding material. As presented in Chapter 2, for a n-type (resp. p-type) semiconductor, the Fermi level is shifted towards the conduction (resp. valence) band. Then, the formation of the interface between both semiconductor leads to the bending of the conduction band energy. This bending results from the diffusion of charge carriers in the opposite doping side leading to the variation of the electric potential and consequently to an electric field resulting of the space charge within the depletion region. A negative electric field is observed at 0 V. This one is is directed from the n-side towards the p-side and is responsible for the drift current density leading to the motion of electrons (resp. holes) to the n-side (resp. p-side). Under thermodynamic equilibrium conditions, the contribution of the diffusion and the drift current densities are equal and no net current is observed in the PN-junction.

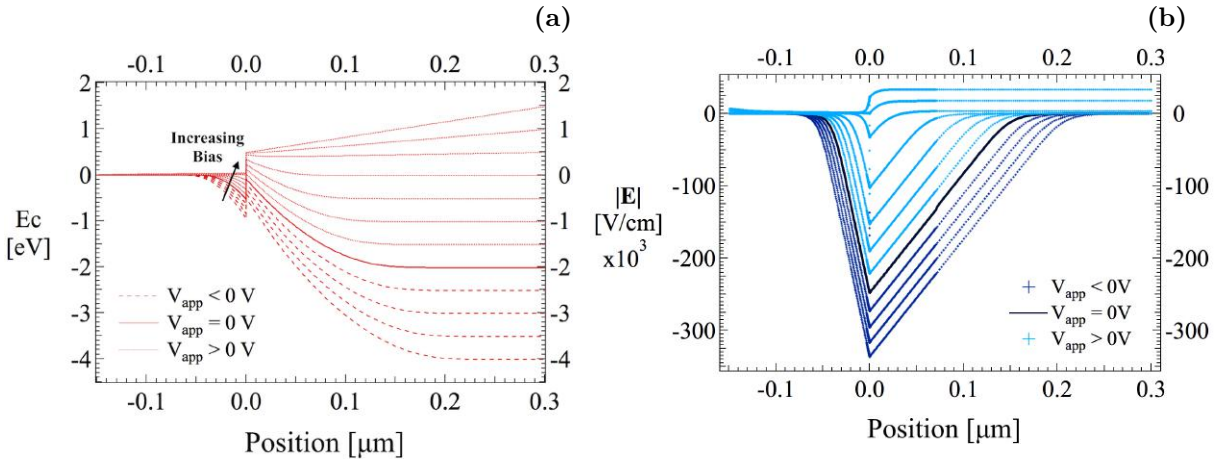

Fig. 5.4: (a) Evolution of the conduction band energy E_C and (b) the electric field $\vec{E}$ as a function of the position for an applied external bias V_{app} between -2V and 3.5V

[4]The electronic affinity difference in term of percentage is determined as 37.23%.

In Fig. 5.4a, the evolution of the conduction band energy as a function of the position for an applied external bias ranging from -2 to 3.5 V is presented. As the bias applied decreases, the slope of the conduction band increases and the confinement region also increases. As observed in Fig. 5.4b, a decreasing external bias leads to an increasing absolute value of the electric field within the depletion width oriented towards the p-side. As a consequence, electrons which diffuse from the n-side towards the p-side are directly swept by the electric field towards the n-side. The minority charge carrier concentration within the p-side consequently decreases. For a positive applied external bias, the conduction band energy value at the edge of the n-side increases and consequently, the slope near the interface is reduced. At V_{app}= 1.3 V, the conduction band edge on the p-side is at the same height as the conduction band edge on the n-side within the neutral regions. The height of the bump at the interface is equal to the band gap energy difference between both materials. For larger value of the external bias, the well in the conduction band at the interface disappear and the n-side becomes positive. Then, above V_{app}= 1.3V, the electric field value above becomes positive. This behaviour indicates an electric field oriented from the p-side to the n-side leading to a high injection of electrons (resp. holes) in the p-side (resp. n-side). Moreover, as presented in Fig. 5.3d, for a large positive applied external bias, the external electric field overcomes the intrinsic electric field created at the junction due to contact potential (cfr. Chapter 2).

In Fig. 5.5a, the charge carriers concentrations are presented as functions of the position in the PN-junction for different values of the external voltage within the range [-2,2] V with a step of 0.5 V.

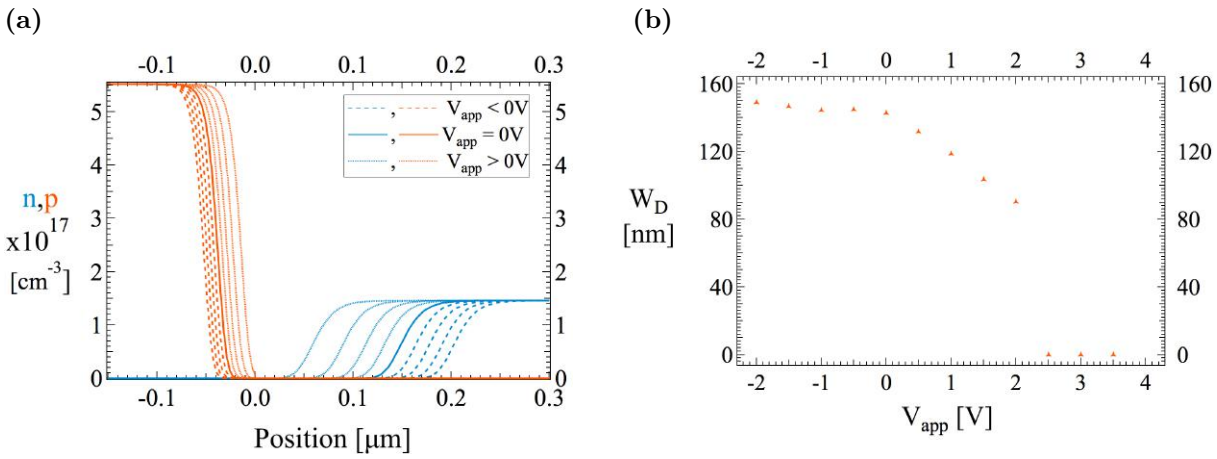

Fig. 5.5: (a) Charge carrier concentrations as functions of the position for the PN-junction without considering defect levels within the band gap, for an applied external bias within -2;2 V with a step of 0.5V. (b) Evolution of the depletion width as a function of the applied external bias between -2 and 3.5 V.

The result shows that in the neutral region on the n-side (resp. p-side), the charge carrier concentration is equal to the doping concentration which is 1.46×10^{17} cm^{-3} (resp. 4.77×10^{17} cm^{-3}, a value that is several orders of magnitude higher than the intrinsic concentration (cfr. Eq.(5.16) and (5.17)). Then, as the charge carrier concentration curves gets closer to the interface, a drop is observed, leading to a free charge carrier zone at the interface, the depletion region. On the p-side (resp. n-side), the hole (resp.

electron) concentration is the intrinsic concentrations under thermodynamic equilibrium. Consequently, they act like minority charge carriers with a concentration that is several orders of magnitude lower than the majority charge carrier concentration. As explained in Chapter 2, the depletion region is a volume in the material that is void of charge carriers, where the dopant atoms are fully ionised. Figure 5.5b shows the depletion width as a function of the potential applied. In this case the depletion width has been computed as the width between the position for which the $n < n_i$ and the position for which $p < p_i$. As presented in Fig. 5.5a, the depletion width on the p-side is shorter than that on the n-side. This observation is in good agreement with the theoretical prediction that a heavier doping concentration leads to a thinner depletion width within the semiconductor. In agreement with Eq.(2.32), the increase of the depletion width as function of the applied bias follows a square-root like trend. Moreover, results for large negative biases demonstrate *a posteriori* the need to extend the computation domain to 300 nm for the n-side. Indeed, as shown by the calculations, the neutral region starts at distances beyond 250 nm at that side. It is useful to note again that non degenerate semiconductors are assumed in the numerical model. In the experimental part, the charge carrier concentrations are higher and, as a consequence, the depletion width is thinner.

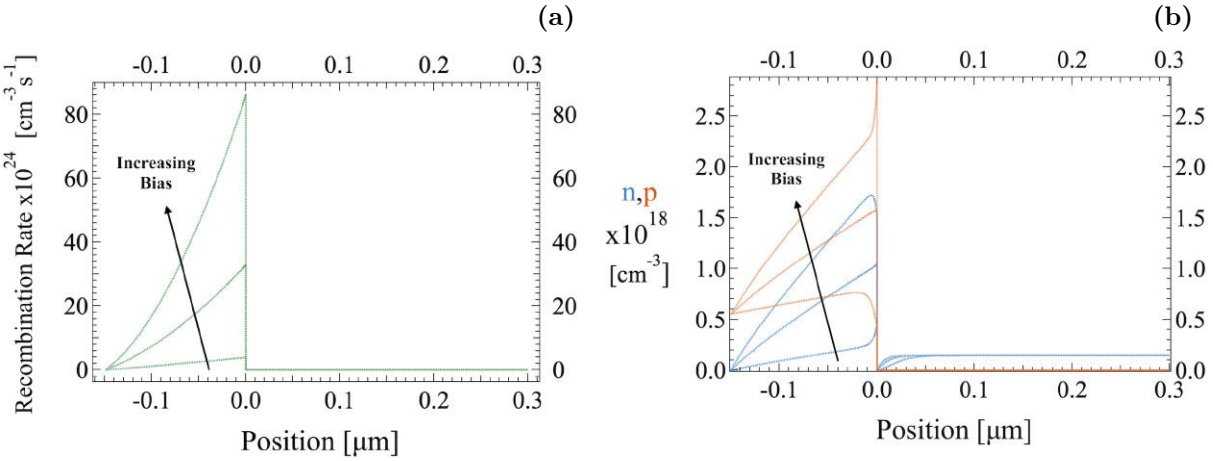

Fig. 5.6: (a) Recombinations rate and (b) charge carrier densities functions of the position for the PN-junction without considering defect levels within the band gap for an bias applied of 2.5, 3 and 3.5V.

In Figure 5.6, the recombination rate as a function of the position in the PN-junction is presented (cfr. Fig. 5.6a) along with the charge carrier concentration for a large external applied voltage (cfr. Fig. 5.6b). The recombination rate presented takes into account the band to band radiative recombinations. Consequently, each EHP recombination leads to the emission of a photon at the energy of the band gap. As shown in Fig. 5.6a, recombinations occur in the p-side of the heterojunctions. This process results from the combination of the injection of minority carriers and the landscape of the electric potential in the vicinity of the junction interface.

As presented in Fig. 5.3 there is an asymmetry in the barrier height seen by the holes bound to travel into the n-side and the barrier height seen by the electron bound to enter the p-side due to the band gap and electron affinity differences between both

semiconductors. As a consequence of this lower barrier height for electrons, with an applied external bias, electrons can overcome this barrier and travel to the p-side where they become minority charge carriers. Therefore, EHP recombinations start to occur at the interface on the p-side, with a rate that decreases with the distance in the p-type semiconductor from the metallurgical interface. This observation confirms the theoretical prediction of Eq.(2.25). Indeed, the recombination rate is limited by the minority charge carrier concentration. This concentration decreases exponentially with a characteristic time given by the minority charge carrier life time. In addition, as presented in Eq.(2.48), the excess of charge carrier concentration at a given point in the p-side decreases with a characteristic length L_n which gives the mean free path travelled by an electron in the p-side before recombination with a hole. In addition, as the applied bias increases, the excess of charge carrier at the interface increases and as a result, the total number of recombinations increases.

Concerning the charge carrier densities for a large (over 2.5 V) values, as it can be seen in Fig. 5.6b, an accumulation region take place in the p-side close to the interface between both semiconductors. Furthermore, as the recombination rate depends on the minority charge carrier concentrations, the increasing of the concentration explains the increase in the recombination rate observed for an increasing applied bias.

In Fig. 5.7, the current density-voltage characteristic of the PN-junction is presented for an applied bias between -7.5 and 7.5V.

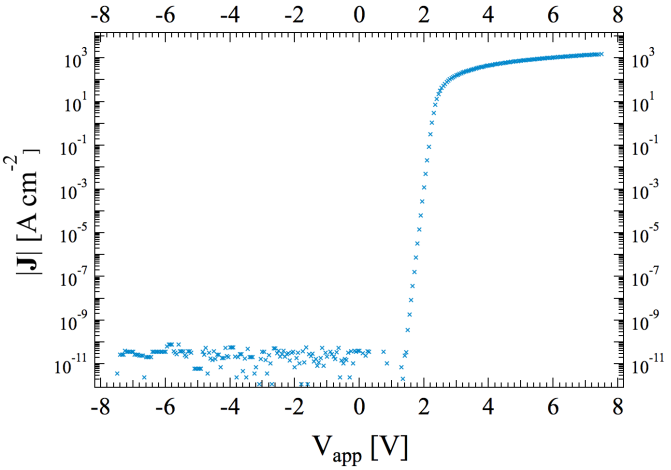

Fig. 5.7: Current density voltage characteristic of the PN-junction as obtained from numerical simulations.

For a bias applied below 0 V, a saturation density current of 3×10^{-10} A cm^{-2} is reported. In the reverse bias regime, the non-convergence of the numerical simulations (cfr. Fig. 5.2) with a tolerance factor of 10^{-8} is responsible for the lower accuracy in the result for the current density. A more refined mesh would then be required and a lower tolerance factor should be used to improve the accuracy of the numerical simulations in the reverse bias regime. In comparison with the ideal IV curve presented in Fig. 2.11, the rise of the current takes place at a positive threshold voltage of 1.3 V. This value corresponds exactly to the band gap difference between the two semiconductors. Indeed, as explained previously, the bump in the conduction band created at the interface and resulting from

the band gap difference has to be overcomes by the external voltage applied in order to inject majority charge carriers in the opposite region. Once the external voltage applied overcome this threshold voltage V_t [V], an exponential increase of the current density is observed. The corresponding Schokley diode equation is expressed by:

$$J = J_S \ (e^{q(V_{app}-V_t)/nk_BT} - 1) \tag{5.18}$$

For $V_{app} > V_t$, the exponential term becomes important in comparison to 1 and the previous equation can be approximated by:

$$J \simeq J_S \ e^{q(V_{app}-V_t)/nk_BT} \tag{5.19}$$

$$\Leftrightarrow \ln J \simeq \ln J_S + \frac{q(V_{app} - V_t)}{nk_BT} \tag{5.20}$$

$$\Leftrightarrow \ln J \simeq \left(\ln J_S - \frac{V_t}{nk_BT}\right) + \frac{qV_{app}}{nk_BT} \tag{5.21}$$

Consequently, by performing a linear fitting ($\ln J = a + b\ V_{app}$) in the linear region, the saturation density current J_S and ideality factor n of the diode can be determined. The linear fitting coefficient determined are a =-55.331 $\pm$ 0.447 and b = 28.802 $\pm$ 0.23. The calculated ideality factor is 1.34 and the saturation current density is equal to 1.04 10^{-9} A cm^{-2}. An ideality factor of 1 is associated to recombinations occurring only within the depletion region while an ideality factor of 2 is related to recombinations occurring outside the depletion layer, in the neutral regions. Furthermore, an ideality factor close to 1 is related to radiative recombinations while an ideality factor close to 2 is related to non-radiative recombinations [27] [5].

In the voltage range [1.2V-2V], the current density is limited by the depletion region and the energy barrier is present at the interface. Beyond V_{app} = 2V, the current density reaches levels around 10^3 A cm^{-2}. Multiplying this quantity by the area of the metallic contact used in the experimental fabrication process[6], the resulting current is of the order of 76.8 A. This high value of the current can be explained by the fact that in the numerical simulation assumes a perfect PN-junction, without any impact from impurities, interface quality or contact resistances. However, in real devices, these contact resistances are several orders of magnitude higher than the bulk resistances of the materials measured. They contribute in an important way to the device electrical resistance.

In addition, over V_{app} = 2 V, the current density is no longer limited by the PN-junction behaviour but by the series resistance of the neutral region in both semiconductors. Based on the charge carrier mobilities and concentrations, these series resistances associated to each layer can be predicted.

$$\rho = \frac{1}{qn\mu} \tag{5.22}$$

[5] Described in Chapter 18: Diodes.

[6] An area of 0.07068 cm^2 is taken here in order to fit the results with the metallic contact area of the fabricated PN-junction

Indeed, the electrical resistivity of the layers can be calculated with Eq.(5.22). The obtained values are respectively, for Cu_2O:Mg layer and AZO layer equal to 58.85 Ω cm and 109.62 Ω cm.

As presented in Fig. 5.8, in the case of degenerate semiconductors, the expected value of the expected electrical resistivity is several orders of magnitude lower than the one used for non-degenerate semiconductors in our numerical simulations.

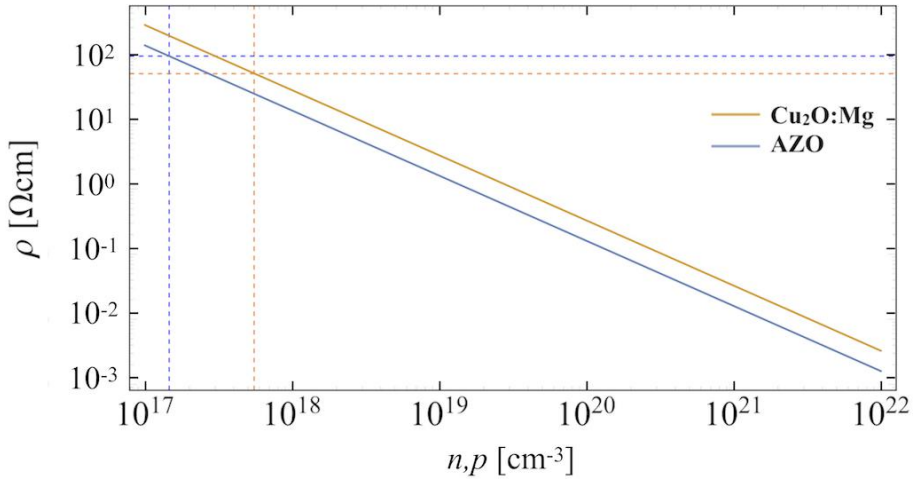

Fig. 5.8: Evolution of the electrical resistivity as a function the charge carrier concentration in a double logarithmic scale.

$$R_S = \rho \frac{l}{A} \tag{5.23}$$

Using Pouillet's law (cfr. Eq.(5.23)), the series resistance is calculated using the length of the neutral zone in the respective semiconductor and the area of the contact. These quantities depend on the neutral region thicknesses which vary as a function of the applied external bias as shown in Fig. 5.5. However, for a large applied bias, the depletion region vanishes and the dominance of the series resistance appears. As a consequence, the neutral regions correspond to the whole semiconductor lengths.

In addition, the evolution of the series resistance as a function of the bias can be calculated (cfr. Eq.(5.24)) using the variation of the neutral zone as a function of V_{app} in the region limited by the behaviour of the PN-junction. As shown in Fig. 5.9, for an external applied voltage between -2 to 2.5V, the increasing behaviour corresponds to the evolution of the thicknesses of the neutral region in each part of the junction. In this region, the depletion region dominates the behaviour of the PN-junction. Above $V_{\text{app}} =$ 2.5V, the depletion region vanishes, the neutral regions corresponds to the whole semiconductors and the ohmic behaviour appears. In this region, the series resistance dominates the behaviour of the PN-junction.

$$R_S = R_S^{Cu_2O:Mg} + R_S^{AZO} = 1.25 \times 10^{-2} + 4.65 \times 10^{-2} = 5.9 \times 10^{-2}\ \Omega \tag{5.24}$$

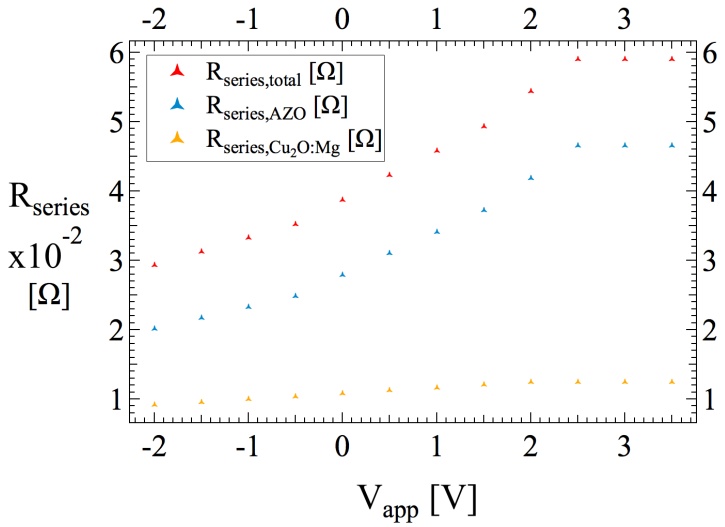

Fig. 5.9: Evolution of the series resistances associated to the independent Cu_2O:Mg, AZO semiconductor layers as well as of the total series resistance as a function of the applied external bias V_{app}.

In addition, the series resistance can also be determined from the JV curve characteristic (cfr. Fig. 5.7). By plotting the current-voltage curve in the ohmic region, the inverse of the slope yields the series resistance accordingly to Ohm's law. The obtained value is equal to 4.75×10^{-2} Ω.

The numerical simulation of the PN junction finally enables the calculation of the emission spectrum (cfr. Fig. 5.10). This one is computed owing to the recombination rate R determined for an applied external bias V_{app} of 2.5, 3 and 3.5 V (cfr. Fig. 5.6). This region corresponds to the ohmic behaviour of the PN-junction. Based on these results, the frequency of recombination is determined by integrating the recombination rate over the cuprous oxide thickness t (cfr. Fig. 5.6), as follows:

$$\nu_R = S \int_0^t R(x)dx \qquad (5.25) \qquad \text{and} \qquad \mathcal{P}_R = q\ E_g\ \nu_R, \qquad (5.26)$$

where S is the surface on which the external bias V_{app} is applied. The radiative power $\mathcal{P}_R$ [Watt] is defined as the number of photons emitted at the band gap energy of the cuprous oxide per unit time (cfr. Eq.(5.26)). In order to convert the radiative power in Lumen, the SI unit for the light flux, the radiative power is weighted accordingly to the sensitivity of the human eye. Then, the emission is expressed in candela by dividing the radiative power expressed in Lumen by the solid angle of the emission. This one is equal to 12.531 [st] which corresponds to the integration solid angle of the device used in the experimental measurement. As explained in Section 2.3, in order to quantify the emission, several efficiencies have to be taken into account. First the internal quantum efficiency and secondly the extraction coefficient. In the perspective of enabling a possible comparison with manufactured LEDs, the external quantum efficiency is taken as 1% [27][7]. Finally, in order to obtain the shape of the emission spectrum presented in Section 2.1.3,

[7] According to Grund *et al.* (Chapter 20: Electricity-to-light conversion), a manufactured GaAs LED exhibits an external efficiency around 2.7%.

the luminous flux per steradian [cd] is multiplied by the behaviour of DOS according to the energy for a spectral range within $E_g = 2.09$ and $2.09+k_B T/2$ eV. This one evolves as the square root of the energy. And multiplied by the Maxwell-Boltzmann distribution for a spectral range within $2.09+k_B T/2$ and $+\infty$ eV.

In the emission spectra shown in Fig. 5.10, the radiation intensity in the dominant wavelength range is of the order of a few candela's. In order to get an appreciation of the result, one candela corresponds approximately to the luminosity of one candle. As is can be seen here, the theoretical luminosity of the PN-junction under an applied external bias $V_{app} = 3.5$ V reaches a maximum value of the order of 3 cd.

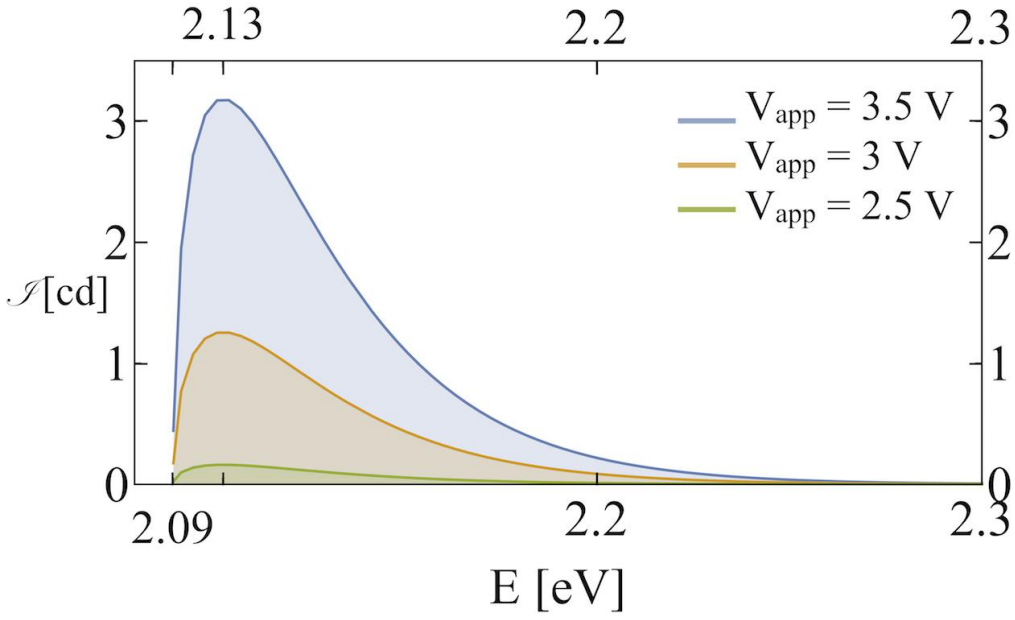

Fig. 5.10: Emission spectrum resulting from the numerical simulation of the PN-Junction without considering defect levels within the band gap. The radiative intensity is calculated from the recombination rate determined respectively for an applied external bias of 2.5, 3 and 3.5 V by taking into account an external quantum efficiency η_{ext} of 1%.

Experimentally, a lower value of the luminosity is expected due to the following factors:

- The presence of defects and impurities which are for on part taken into account in the external quantum efficiency that was applied but on the other hand, radiative recombinations through defects levels within the band gap are associated to photon emission with a smaller energy than E_g. Consequently, the presence of defects in the PN-junction reduces the ideality of the heterojunction and involves emission peaks at lower energies.

- By taking into account the contact resistances, the current density is reduced and consequently the number of minority carriers injected in the p-side is also reduced. Such a weaker minority charge carrier concentration leads to a reduction of the recombination rate and of the radiation intensity.

The next chapter deals with the results of the experimental part of the thesis work.

Chapter 6

ZnO:Al/Cu_2O:Mg Heterostructure: Growth and Characterization

I this chapter, we present the experimental results based on the theoretical background developed in Chapter 2 and Chapter 3. These results were obtained using the different characterization techniques presented in Chapter 4. The first Sections (cfr. Sections 6.1 and 6.2) present respectively the optimisation of the resistivity and the transmittance of Cu_2O:Mg and AZO thin films with respect to the deposition temperature T_S [°C] and the post-annealing treatment. Finally, Section 6.3 focus on the fabrication of the PN-junction based on the results obtained in the two previous sections.

Main results and concepts presented and explained in this chapter:

- Cu_2O:Mg thin film lowest resistivity (16.32 Ωcm) is obtained with a deposition temperature of RT (181.8 Ωcm for 200°C). At this deposition temperature the transmittance of the film in the visible wavelength range (21.06 %) decreases by an average amount of 23.37% compared to the deposition at $T_S = 200$°C. The band gap energy at RT is 2.32 eV and an increasing band gap energy of 2.52 and 2.47 eV is observed for 200°C and 350°C deposition temperatures. An optimal temperature of RT is identified for the purpose of junction fabrication.
- AZO lowest resistivity (9.644×10^{-4} Ωcm) is obtained at the highest deposition temperature $T_S = 300$°C without annealing. Above $T_S = 200$°C, there is no benefit from RTA in terms of electrical behaviour. The average transmittance is around 70 % for all deposited temperature. An improvement of the crystal quality is observed as T_S increases. The most efficient TCO thin film is obtained at $T_S = 250$°C with an energy band gap of 3.53 eV.
- Two PN-junctions were fabricated based by successive depositions of AZO deposited at 250°c and Cu_2O:Mg deposited at RT and 200°C based on the previous optimisation substrate temperature. Both junctions present a rectifying behaviour. A improvement of the rectifying behaviour was observed for the AZO-250/Cu_2O:Mg-200 junction. In order to measure the emission spectrum of the junction a thorough investigation of the electrical contact is required to tackle the issue of leakage currents within the junction.

6.1 Cu_2O:Mg Thin Film Growth and Characterization

This section is focused on the electrical, optical and morphological characterization of Cu_2O:Mg thin films grown by RF magnetron sputtering. The evolution of the thin film properties are studied as function of the deposition parameters.

6.1.1 Cu_2O:Mg Thin Films Deposition

As described in Chapter 3 (cfr. Section 3.3), the optimal electrical and optical properties of Cu_2O:Mg are obtained with the lowest chamber base pressure P and with the highest power $\mathcal{P}$. Nevertheless, in order to avoid experimental issues like the deterioration of the target base plate due to melting of the seals. The sputtering power is limited to 22%. Despite this limitation, it was possible to reach a maximal power of 66 W applied on a target with a surface of 20.268 cm^2. Consequently, acceptable deposition rate were reached and the quality of the crystallinity of the films was not impacted. For the depositions, a pure Cu_2O target containing 17% of Mg per unit of weight was used (99.99% purity). As presented in Tab. 6.1, 2 different sets of Cu_2O:Mg thin films samples were deposited. Half of the samples are deposited on FTO-coated glass substrates (S1) and the other half on glass substrate (S2) in order to characterize electrically and optically the thin film itself. Indeed, the presence of the FTO coating on the glass substrate, which is required to obtain an operating junction, prevents the independent thin film characterization due to the low resistivity of the FTO could lead to a short-circuit in the structure. In order to extract the transmittance and the resistivity of the film itself, samples deposited on glass were then characterized. For the junction elaboration, the Cu_2O:Mg thin film is deposited on a substrate of made of glass coated with a 350nm-thick FTO film. These samples are morphologically characterized using SEM, including an assessment of the film crystallinity. These characterizations allow us to extract optical and electrical properties of the films themselves and also to evaluate the impact of the crystallinity of Cu_2O:Mg thin films on these properties.

Sample ID	T_S [°C]	P [Torr]	$\mathcal{P}$ [W]	DR [Ås^{-1}]	P_{Ar} [mTorr]	t_{quartz} [nm]	Substrate
Cu_2O:Mg-S1-1	RT	1.40×10^{-7}	51.6	0.3	5	151.81	Glass/FTO
Cu_2O:Mg-S1-2	200	2.50×10^{-7}	53.1	0.3	5	151.84	Glass/FTO
Cu_2O:Mg-S1-3	350	1.49×10^{-7}	51.3	0.3	5	151.88	Glass/FTO
Cu_2O:Mg-S2-1	RT	7.03×10^{-8}	52.8	0.3	5	151.12	Glass
Cu_2O:Mg-S2-2	200	1.83×10^{-7}	52.5	0.3	5	151.91	Glass
Cu_2O:Mg-S2-3	350	8.70×10^{-8}	53.7	0.3	5	150.34	Glass

Tab. 6.1: Deposition parameters used for two sets of Cu_2O:Mg thin films. S1 samples deposited on FTO-coated glass substrate and S2 samples deposited on glass substrates.

In Table 6.1, the parameter studied for the deposition of Cu_2O:Mg thin films is the substrate temperature T_S. As explained in Chapter 3 (cfr. Section 3.3), the optimisation of this parameter is the most relevant taste which needs to be carried out in terms of junction fabrication. As consequence, three depositions temperatures were performed, one at RT, a second one at 200°C and the last one at 350°C. These temperatures are notably chosen with the motivation of completing the experimental data obtained by Malier [44]. The

depositions were performed with a chamber pressure within the range [0.703;2.5] 10^{-7} Torr. This accidental chamber pressure variations between the different deposition can lead to additional variations of the thin films properties. The depositions are performed with a sputtering power around 52 W leading to a deposition rate of about 0.3 $Å s^{-1}$. In order to compensate for the reduced sputtering power compared to a previous work [44], the argon pressure is increased by 40% in order to have the same deposition rate. Finally, the aimed thickness and the argon flux rate are set respectively to 150 nm and 20 sccm. The thicknesses presented in Tab. 6.1, are values measured by the quartz crystal present monitoring system in the deposition chamber. Nevertheless, this piezoelectric material is configured with the mass of undoped Cu_2O molecules. However, the number of doped atoms within the bulk materials is low and consequently, the induced mass variation due to the doping can be neglected [1].

(a) T_S = RT **(b)** T_S = 200°C **(c)** T_S = 350°C

Fig. 6.1: Cu_2O:Mg samples photographies concerning the deposition temperature T_S of (a) RT=40°C, (b) 200°C and (c) 350°C.

Photographs of the samples, presented in Fig. 6.1, show that for T_S = RT, the layer is more opaque than the others exhibiting a brown colour. As the substrate temperature increases, the deposited film becomes yellowish and the transparency seems to be improved.

6.1.2 Cu_2O:Mg Thin Films Geometrical Characterization

In order to obtain a measurement of the thickness of the films, a step height measurement is performed as presented in Tab. 6.2 which summarises the results obtained for the Cu_2O:Mg thin films characterization. These ones are presented and interpreted throughout this section.

Sample ID	T_S [°C]	t_{Dektak} [nm]	ρ [Ωcm]	$\mathcal{T}_{vis}$ [%]	E_g [eV]
370	RT	78	16.3	21.06	2.32
366	200	50	181.8	44.43	2.52
372	350	120	365.8	46.08	2.47

Tab. 6.2: Cu_2O:Mg thin films resistivity and average transmittance in the visible wavelength range [400-800] nm.

[1] In Cu_2O, the number of atoms per cubic centimetre is 2.52×10^{22}. The doping concentrations are consequently several orders of magnitude below this value.

The Dektak measurement consists in a profilometry of the deposited thin film performed from the bare substrate. The sample's surface height is spatially measured from the bare substrate to the top of the deposited film and a step-like curve is obtained. The height of the step corresponding to the thickness of the deposited thin film (cfr. Fig. 6.2). A complement of information about the Dektak measurement can be found in Annexe A. Since the thickness is used in the electrical characterization and in the calculation of the absorption coefficient α of the thin film, the knowledge of the information is critical.

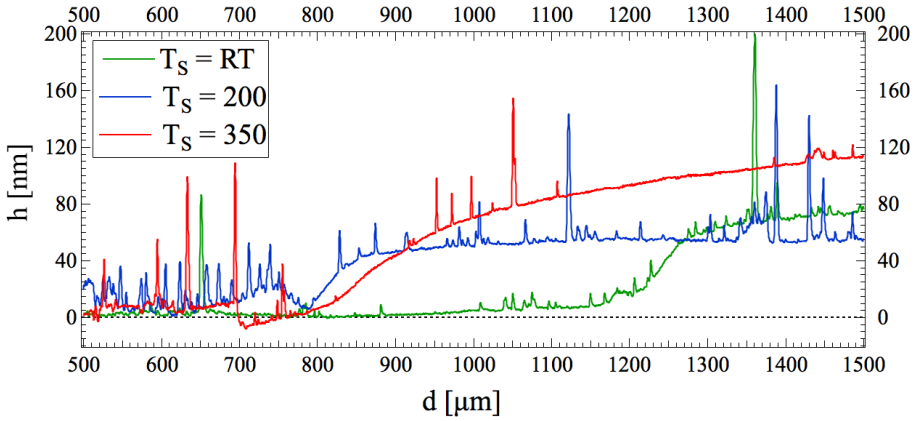

Fig. 6.2: Profilometry of the samples with Cu_2O:Mg thin films deposited at RT, 200°C and 350 °C. d corresponds to the distance covered on the sample and h is the recorded vertical position of the profilometer tip in physical contact with the sample surface. h=0 corresponding to the substrate' surface height taken as reference for the measurement.

As presented in Fig. 6.2, the thicknesses of the samples are all below 150 nm. As explained in Chapter 4, the standard deviation on the thickness measurement is 7.84%. Furthermore, the macroscopic roughness of the sample can be evaluated using this measurement technique. The large peaks present in the thickness measurements corresponds to dust and waste particles present on the thin film due to manual handing. The difference between the thicknesses given by the quartz crystal t_{quartz} and the ones measured ranges from 20 to 66 %. The investigation of this thickness variation led to the study of the thin film thickness as a function of the position of the sample on the substrate holder during the deposition in order to avoid this thickness variation for the deposition of the thin films in the heterojunction fabrication (cfr. Section 6.3). A first deposition is performed without rotation by placing 5 samples on the substrate holder in the same direction than the sputtering target as presented in Fig. 6.3a.

As shown in Fig. 6.3a, there is an angle between the substrate holder orientation and the sputtering target orientation. This angle induces a non-uniform thickness of deposition depending on the sample position. In order to mitigate this effect, rotation was applied on the substrate holder of with a speed of 2.5 Round Per Minute (rpm) during deposition. As shown in Fig. 6.4a, the rotation solves the antisymmetric behaviour of the thickness concerning the sample position with respect to the sample holder centre (cfr. Fig. 6.3b). The behaviour of the thickness as a function of the sample position on the substrate holder presented in Fig. 6.4a can be explained by looking at the target used. Indeed, this one is worned due to the important number of depositions performed with it. By looking at the photography of the target (cfr. Fig. 6.4b), a circular shape

is observed as well as pits due to erosion. This curvature of the target induces a non uniform plasma at the surface of this one during the deposition process. In consequence, due to the large mean free path of electron [2] compare to the target-sample distance, the shape of the target impresses itself on the substrate holder leading to non-uniformity of the deposited thickness (cfr. Fig. 6.4a).

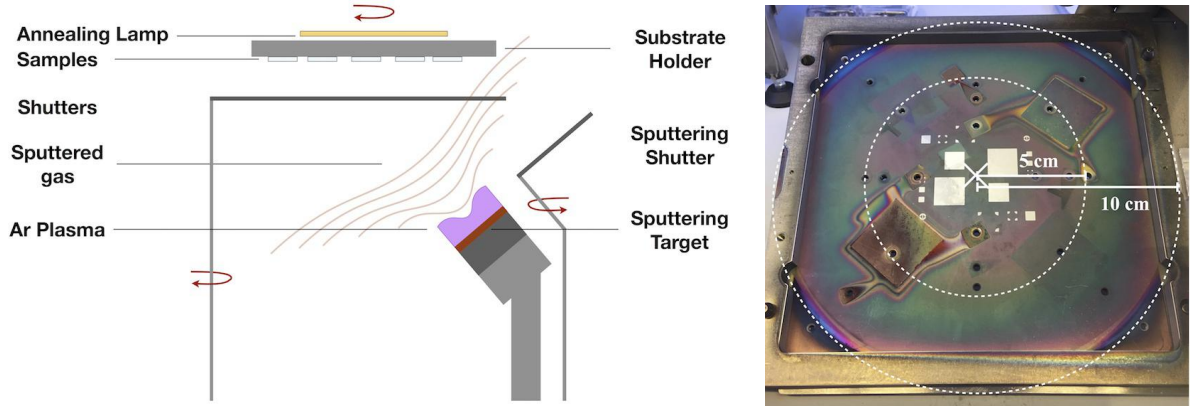

Fig. 6.3: (a) Schematic representation of the sputtering deposition. Highlight of the angle between the sputtering target and the substrate holder. (b) Annotated photograph of the substrate holder used. The centre of this one taken as reference for the sample position measurement.

In order to obtain a uniform thickness for the samples of a same deposition, the thickness of the samples placed at 5 cm of the substrate holder samples is measured. Then, the deposition time is adjusted in order to get the desired thickness. The information obtained in this part was used in the PN-junction fabrication (cfr. Section 6.3)

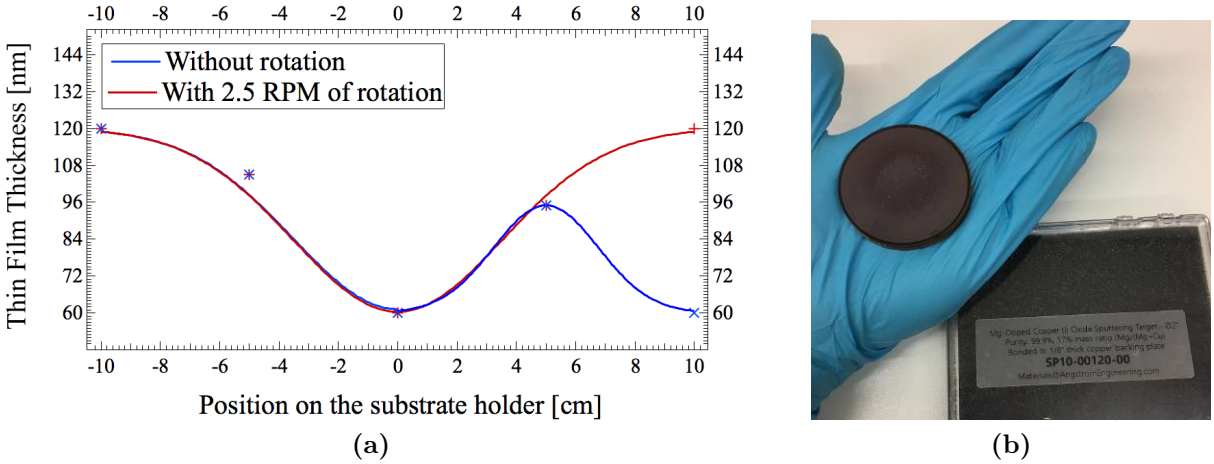

Fig. 6.4: (a) Study of Cu_2O:Mg thin film thickness variation as a function of the position of the sample on the substrate holder in the deposition chamber. 0 is taken as the centre of the substrate holder chosen as reference. (b) Cu_2O:Mg sputtering target. This one present an observable erosion in sinusoidal shape as seen from the centre to the edge of the target induced by the successive depositions performed.

[2] 10cm - 1km for a pressure between 8 10^{-4} and 8 10^{-8} Torr.

In order to complete the morphological and geometrical characterization of the sample, SEM imaging of the cross-cross-sectional view of the Cu_2O:Mg thin films are presented in Fig. 6.5 for deposition temperatures of RT, 200 and 350°C. These SEM images also allow to get a first insight of the nanoscopic roughness and crystallinity of the sample. In a following paragraph, the SEM images are specifically used to characterize the crystallinity of the deposited thin films based on the Thornton' structure-zone model.

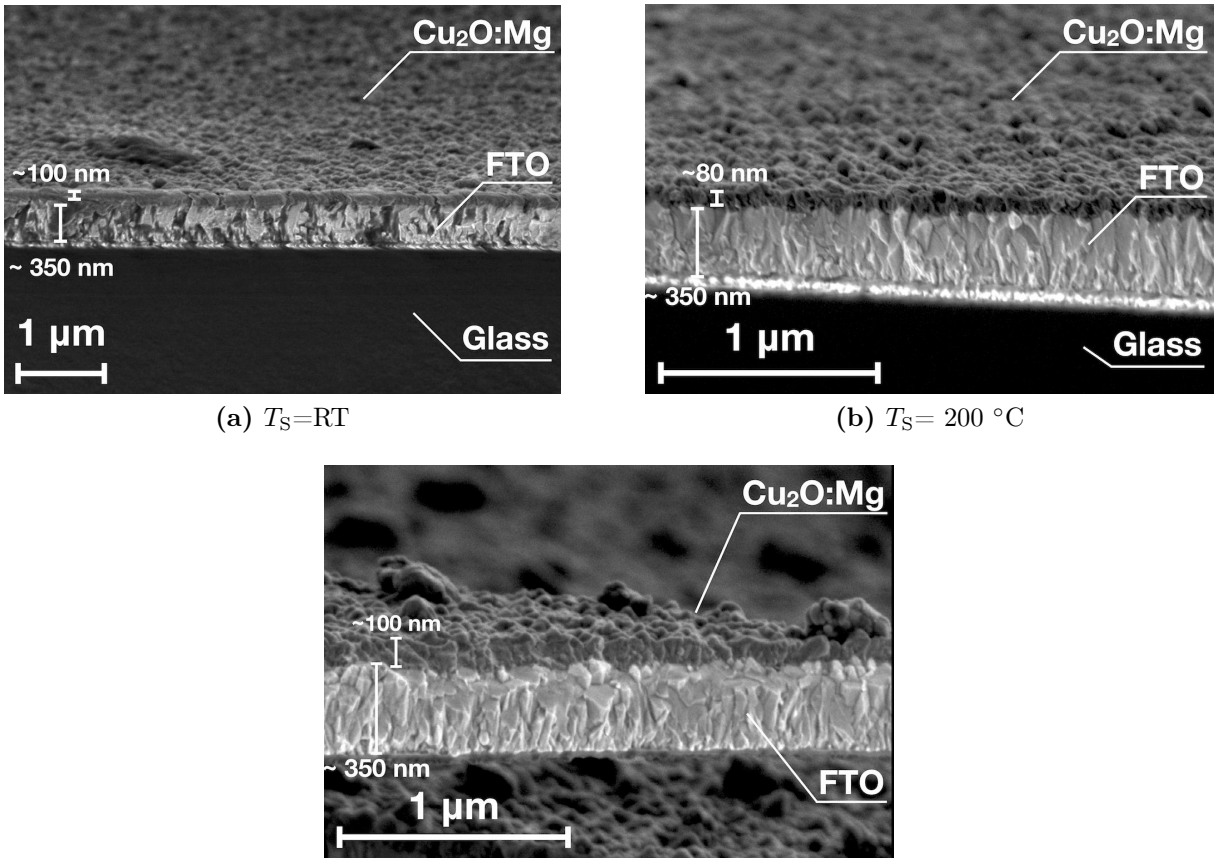

(a) T_S=RT **(b)** T_S= 200 °C

(c) T_S= 350 °C

Fig. 6.5: Morphological characterization of Cu_2O:Mg thin films deposited at (a) RT, (b) 200 and (c) 350 °C. SEM cross-sectional views of the different samples realised with a working distance of 4.9 mm.

As presented in Fig. 6.5, the upper layer consists in cuprous oxide. This layer is deposited on a 350nm-thick layer of FTO which is more contrasted due to the electrical conductivity difference between both materials. Finally, there is a third layer between the glass and the FTO. As the deposition temperature increases, the uniformity of the film tends to decrease. First at 200°C, bigger grains tends to appear at the surface of the deposited layer and at 350 °C, the thin film seems to grow from islands nuclei. The large grains present at 350°C have a dimension around 200 nm. A specific description of the crystallinity of the film as a function of the deposition temperature is performed at the end of this section and commented based on the optical and electrical results obtained.

The following part is focused on the electrical and optical characterization of Cu_2O:Mg thin films. The electrical resistivity ρ and the energy band gap E_g are provided in Tab.

6.2. These quantities are measured based on the thickness measured previously by using the profilomiter. These quantities are intrinsic properties of the semiconducting materials independent of its geometry. The error on these calculations comes mainly from the thickness measurement error, which propagates on the resistivity and E_g. The average transmittance $\mathcal{T}_{vis}$ is the mean transmittance measured over the visible wavelength range between 400 nm and 800 nm. This particular wavelength range consisting in the interesting part of the spectrum for TCO applications. Table 6.2 summarizes the characterization of Cu_2O:Mg thin films deposited at various temperatures. The next part focusses on the independent description and interpretation of these results.

6.1.3 Cu_2O:Mg Thin Films Electrical Characterization

The electrical resistivity associated to the majority charge carriers as a function of the deposition temperature T_S is presented in Fig. 6.6.

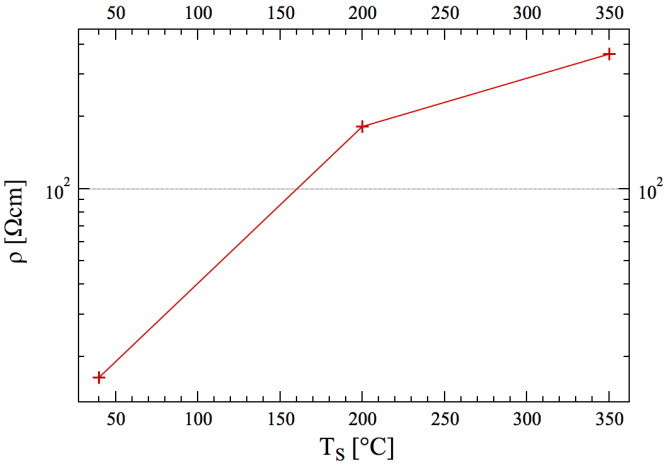

Fig. 6.6: Electrical characterization of Cu_2O:Mg thin films deposited at RT, 200 and 350 °C. Electrical resistivity, majority charge carrier concentration and mobility as a function of the substrate temperature T_S.

As presented in Fig. 6.6, the electrical resistivity increases as a function of the deposition temperature T_S. These ones are respectively 16.3, 181.8, 365.8 [Ωcm] for a substrate temperature equals to RT, 200°C and 350°C, respectively. **The optimal conductivity for Cu_2O:Mg thin film was obtained for the lowest deposition temperature.**

Concerning the measurements of the majority charge carriers concentrations and their related mobilities, the Hall measurement could not be performed in a reproducible way. Variation in term of concentrations of 4 orders of magnitude were observed between several successive measurements on the same sample ([4.8×10^{14}-3.08×10^{16}] cm^{-3}) and the a variation until three orders of magnitude was registered for the mobility measurement ([0.396-344] $cm^2\ V^{-1}\ s^{-1}$). As a result of the non-reproducibility of the Hall measurements, these data are not included in the interpretation of the electrical resistivity obtained. The limitations of the Hall measurement device presented in Chapter 4 could explain these observations. Furthermore, different sources of errors could explain the non-reproducibility of the Hall measurements such as the quality of the contact on

the sample, mechanical crack in the sample or even the heating of the sample induced by the charge carrier motion.

6.1.4 Cu_2O:Mg Thin Films Optical Characterization

Figures 6.7a and 6.7b show the optical transmittance spectra of Cu_2O:Mg thin films as a function of the substrate temperature T_S. In Fig. 6.7a, a baseline is first performed. It was found constant over the wavelength range and set as reference for the measurements which have followed. The baseline has an increasing level of noise for wavelengths over 1700 nm. The bumps that can be observed at 850 and 1700 nm do not seem to originate from physical causes. Instead, they are associated to the grating and the detectors changing occurring at these wavelengths (cfr. Section 4.2). These bumps, present in all transmittance curves, are thus ignored due to their artificial origin.

Then, the transmittance spectrum of the glass substrate is included in Fig. 6.7. It slightly decreases from 92 % to 85 % between 2000 nm and 300 nm. Finally, a drastic drop to 0 is observed below 300 nm. Below 300 nm, photons are consequently absorbed. Over 300nm, 92 % of the incident beam intensity is transmitted and 4 % is reflected at both interfaces with the air. This well-known behaviour reflects an energy band gap around 4.13 eV for the glass.

Concerning the optical general behaviour of Cu_2O:Mg thin films, the average transmittance increases by 15.85 % from T_S = RT to T_S = 200°C and becomes quite constant between T_S = 200°C and T_S = 300 °C. Between 2000 and 700 nm, a decrease of the transmittance and a bump at 580 nm is observed for all films before reaching 0 after 400 nm. From a TEDs application point of view, the optimal optical properties are obtained by deposited Cu_2O:Mg at 350°C, which are quite similar to the ones of Cu_2O:Mg at 200°C.

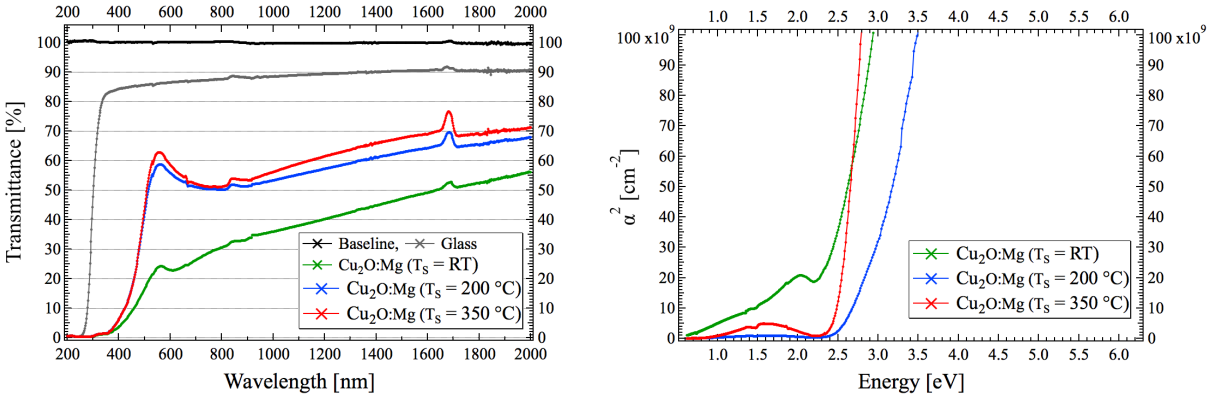

(a) Transmittance Spectra **(b)** Absorption Coefficient Spectra

Fig. 6.7: Optical characterization of Cu_2O:Mg thin films deposited at RT, 200°C and 350 °C. Presentation of (a) the transmittance spectra and (b) the absorption coefficient spectra from which the energy band gap E_g is extracted.

In order to calculate the absorption coefficient, the refractive index of the thin film is required (cfr. Section 4.2). A refractive index n equals to 2.26 is used based on the

results obtained for Cu_2O thin films [65]. Concerning the absorption coefficient spectra presented in Fig. 6.7b, the energy band gap are respectively evaluated to 2.32, 2.52 and 2.47 eV for T_S = RT, 200°C and 350°C. These values were obtained by intersection of a linear extrapolation of the slope of α^2 curves with the energy axis as presented in Chapter 4 (cfr. Eq.(4.19)).

As explained in Chapter 2, the Cu_2O:Mg energy band gap value fix the emission spectrum location in the wavelength range. By transformation of the band gap energies in eV obtained for the various substrate temperature using Eq.(6.1), the emission peaks should consequently be located at 530 nm, 492 nm and 497 nm respectively for T_S = RT, 200°C and 350°C.

$$E[\text{eV}] = \frac{hc}{q\lambda} \simeq \frac{1.24}{\lambda[\mu\text{m}]} \tag{6.1}$$

Figure 6.7b also provides information about the DOS behaviour close to E_C. For Cu_2O:Mg deposited at 350°C, the slope of the curve is higher than the ones for lower deposition temperature. This behaviour reflects a net increasing of the DOS available above E_C and consequently an improvement of the crystallinity. While for a lower slope, photons of energy higher than E_g have lower probability to get absorbed by the thin film.

Information concerning the defect levels can also be obtained from Figure 6.7b. Below the energy band gap, for a perfect crystal, the absorption coefficient should be 0. As presented, it is nearly the case for the 200°C-deposited thin film reflecting a improved crystallinity compared to Cu_2O:Mg deposited at RT and 350°C. Indeed, for these depositions temperatures, bumps in the absorption coefficients curves are observed. These bumps indicate the presence of defects levels within the band gap leading to absorption of photons with an energy lower than E_g. Consequently, the crystallinity of Cu_2O:Mg is improved between RT and 200 °C and then decreases slightly for T_S = 350°C.

To conclude the optical characterization, **the highest transmittance corresponds to the highest deposition temperature and the most optimal crystallinity was obtained for Cu_2O:Mg thin film deposited at 250°C, associated to an energy band gap of 2.52 eV**.

As the characterization of the thin film aims at the fabrication of TEDs, both optical and electrical properties are relevant parameters as explained in Chapter 2. In order to choose the most optimal substrate temperature, a figure of merit (cfr. Eq.(6.2)) and its value for the various deposition temperature is determined.

$$\mathcal{F}_{\text{Merit}} = \frac{\mathcal{T}_{\text{vis}}}{\rho}, \tag{6.2}$$

where $\mathcal{T}_{\text{vis}}$ is the average transmittance over the visible wavelength range between 400 and 800 nm expressed in % and ρ, the electrical resistivity in Ωcm. This figure of merit was established based on the results obtained by Tvarozek *et al.* [66]. As the thicknesses of the films are of the same order of magnitude, the resistivity was favoured. This figure of merit allows a simple understanding of the overall thin film material suitability as a TCO. Indeed, a large $\mathcal{F}_{\text{Merit}}$ value represents an efficient TCO, either through a sufficiently low

electrical resistivity or an important transmittance in the visible wavelength range or a combination of these 2 characteristics.

Sample ID	T_S [°C]	$\mathcal{F}_{Merit}$ [% $\Omega^{-1}cm^{-1}$]
Cu_2O:Mg-S2-1	RT	1.29
Cu_2O:Mg-S2-2	200	0.24
Cu_2O:Mg-S2-3	350	0.12

Tab. 6.3: Figure of Merit of Cu_2O:Mg thin films as a function of the deposition temperature T_S.

As presented in Tab. 6.3, the figure of merit decreases of more than 1 % $\Omega^{-1}cm^{-1}$ between T_S = RT and 200°C. This behaviour reflects the impact of the one order increase of the resistivity even if the transmittance in the visible wavelength range is improved. Then a slight decrease of 0.12 % $\Omega^{-1}cm^{-1}$ i the figure of merit value is observed due to the increasing resistivity of the deposited thin film for a constant value of the transmittance between T_S=200°C and T_S=350°C. To conclude this section, **the most efficient Cu_2O:Mg TCO thin film is obtained at RT**.

6.1.5 Cu_2O:Mg Thin Films Morphological Characterization

The last part of this section is dedicated to the characterization of the morphology of Cu_2O:Mg thin films as a function of the substrate temperature T_S.

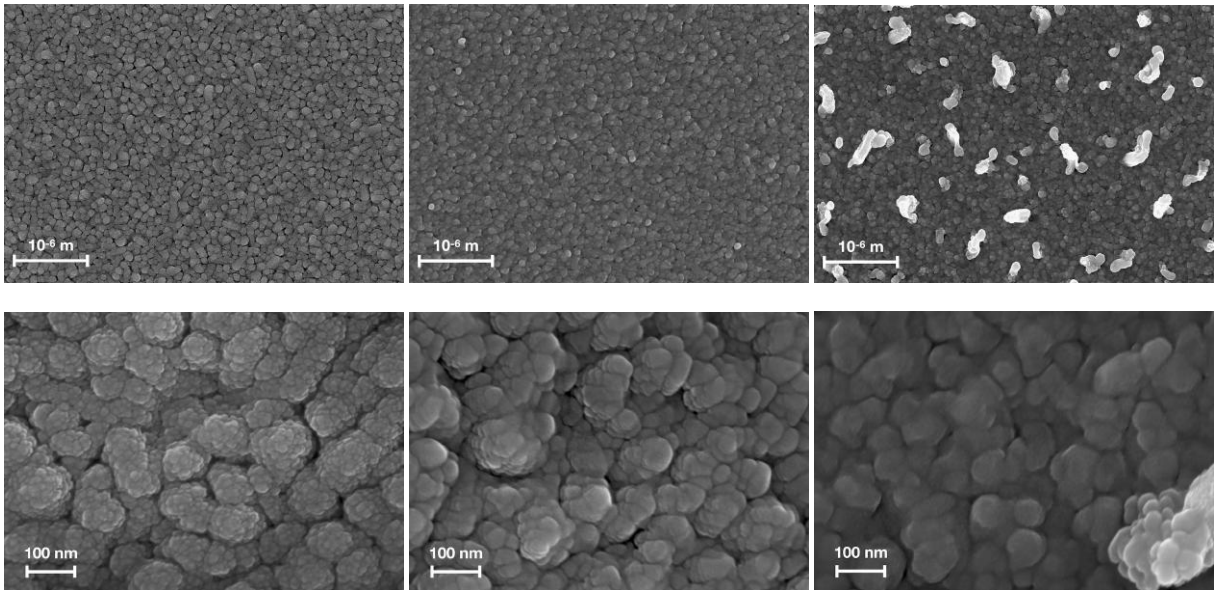

(a) T_S = RT **(b)** T_S = 200 °C **(c)** T_S = 350 °C

Fig. 6.8: Morphological characterization of Cu_2O:Mg thin films deposited at (a) RT, (b) 200°C and (c) 350 °C. Images obtained at a working distance of 3.1mm. (a),(b) and (c) refer respectively to the first, the second and the third column of SEM images.

In Fig. 6.8, SEM images of these thin films are presented with a micrometric scale. The images are first described and secondly compared to Thornton' structure-zone model presented in Chapter 3[33] (cfr. Fig. 3.4). As presented in the first range of images in Fig. 6.8, the film uniformity tends to decreases as the deposition temperature increases. Indeed, agglomerates and island-shaped structures appear on the film surface. As T_S increases, those structures increases in size and can reach several hundreds nanometers in length at $T_S = 350$ °C. These surface structures are also observable in Fig. 6.5 where the size expansion as a function of the temperature is clearly highlighted.

Then, on a smaller scale (second range of images in Fig. 6.8), the grains size is quite constant as a function of the substrate temperature. Nevertheless, the morphology of these ones change with the deposition temperature. As the temperature increases, the alveolar shape observed at RT is smoothed out and polished grains appear. The films grow as columnar structure with voids between them. As the temperature increases, the intergranulars joints are reduced and the voids are filled. This behaviour reflects an improvement of the crystallinity. In comparison to Thornton' structure-zone model, the alveolar shape of the grains composing the film deposited at RT indicates a growth in the zone 1. Then, as the substrate temperature increases, the crystalline structure enters into zone T without however reaching the zone 2.

In Fig. 6.9, an interesting view of a layer consisting of a Cu_2O:Mg thin film on a FTO-coated glass substrate is presented. This layer happens to have been separated from the glass substrate during the sample cut. The FTO and the Cu_2O:Mg layer are thus easily worn. In background, the Cu_2O:Mg layer can be observed as well as the cleavage between both parts. Moreover, large grain structures are observable at the surface corresponding to the one described at the beginning of this paragraph.

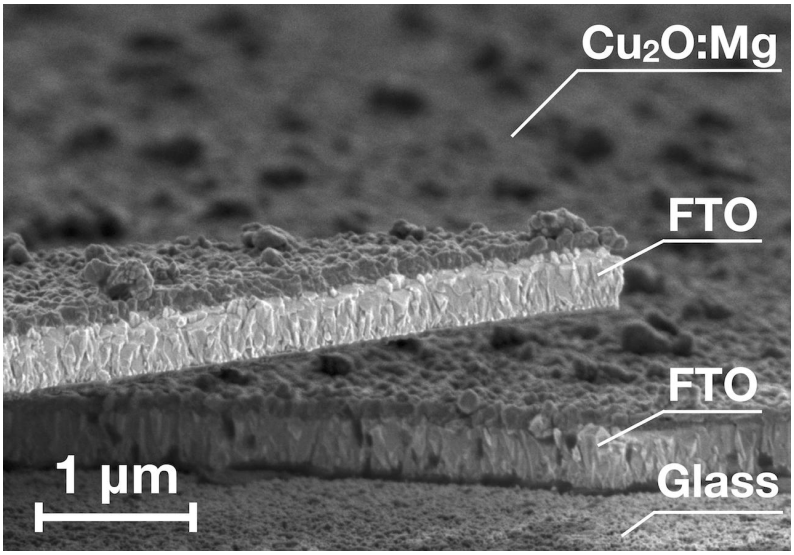

Fig. 6.9: Morphological characterization of Cu_2O:Mg deposited at 350 °C. Interesting SEM cross-sectional view realised with a working distance of 4.9 mm.

In the next section, the deposition parameters and the characterization of the AZO thin film are respectively described and performed.

6.2 ZnO:Al Thin Film Growth and Characterization

This section is dedicated to the optimisation of AZO thin films based on the different depositions parameters. The characterization of the films is presented and interpreted in order to fabricate the PN-junction.

6.2.1 ZnO:Al Thin Films Deposition

As presented in Section 3.3, the optimal electrical and optical properties of AZO thin films were obtained by depositing at the lowest chamber base pressure P, typically in the range [6.38×10^{-8}-1.18×10^{-7}] Torr. In comparison to [44], the chamber base pressure was improved by a factor of 0.5 to 1 as order of magnitude. In combination, the highest sputtering power $\mathcal{P}$ available within the limitation of the PVD-platform is used. A deposition rate of 0.3 [$Å s^{-1}$] is aimed for all deposition. However, as shown in Tab. 6.4, the deposition rate is affected by the deposition temperature. In order to maintain it at 0.3 [$Å s^{-1}$] for high substrate temperature, the associated sputtering power exceeded the limited power. During high substrate temperature depositions and for constant applied sputtering power, a decreasing of the deposition rate is observed during the ten first minutes. After that transient, all along the process, the deposition rate can then gradually increase. The aimed thickness is set to 150 nm and the argon pressure to 5 mTorr with a constant argon flux of 20 sccm. An ZnO target with 2% of Al by weight percentage (99.99% purity) was used during the processes. The deposition parameter studied in the AZO thin film growth is the substrate temperature T_S, is the most relevant parameter in order to improve the AZO thin film electrical and optical properties, as mentioned in Chapter 3. The substrate temperature T_S values that were investigated were 40, 150, 200, 250 and 300 °C. The motivations behind this choice was to highlight the impact of the base pressure reduction on the electrical and optical results, compared to previous data [44], and to obtain the set of data [44].

Sample ID	T_S [°C]	P [Torr]	$\mathcal{P}$ [W]	DR [$Å s^{-1}$]	P_{Ar} [mTorr]	t_{quartz} [nm]	Substrate
AZO-S1-1	RT	9.33×10^{-8}	48	0.3	5	151.04	Glass +FTO
AZO-S1-2	150	1.18×10^{-7}	69	0.27	5	151.01	Glass + FTO
AZO-S1-3	200	6.38×10^{-8}	66	0.23-0.26	5	151.01	Glass + FTO
AZO-S1-4	250	1.05×10^{-7}	63	0.21-0.24	5	150.66	Glass + FTO
AZO-S1-5	300	7.01×10^{-8}	69	0.25-0.27	5	150.32	Glass + FTO
AZO-S2-1	RT	9.33×10^{-8}	48	0.3	5	151.04	Glass
AZO-S2-2	150	1.18×10^{-7}	69	0.27	5	151.01	Glass
AZO-S2-3	200	6.38×10^{-8}	66	0.23-0.26	5	151.01	Glass
AZO-S2-4	250	1.05×10^{-7}	63	0.21-0.24	5	150.66	Glass
AZO-S2-5	300	7.01×10^{-8}	69	0.25-0.27	5	150.32	Glass

Tab. 6.4: Deposition parameters used for two sets of AZO thin films. S1 samples deposited on FTO-coated glass substrate and S2 samples deposited on glass substrates.

Based on the same motivations similar to those expressed in Section 6.1, two different sets of samples were deposited on two different types of substrate. The first set (S1)

deposited on FTO-coated glass substrate provided information on film crystallinity owing to a morphological characterization using SEM imaging. And the second set deposited on glass (S2) was optically and electrically characterized in order to extract the AZO thin film properties concerning the deposition temperature.

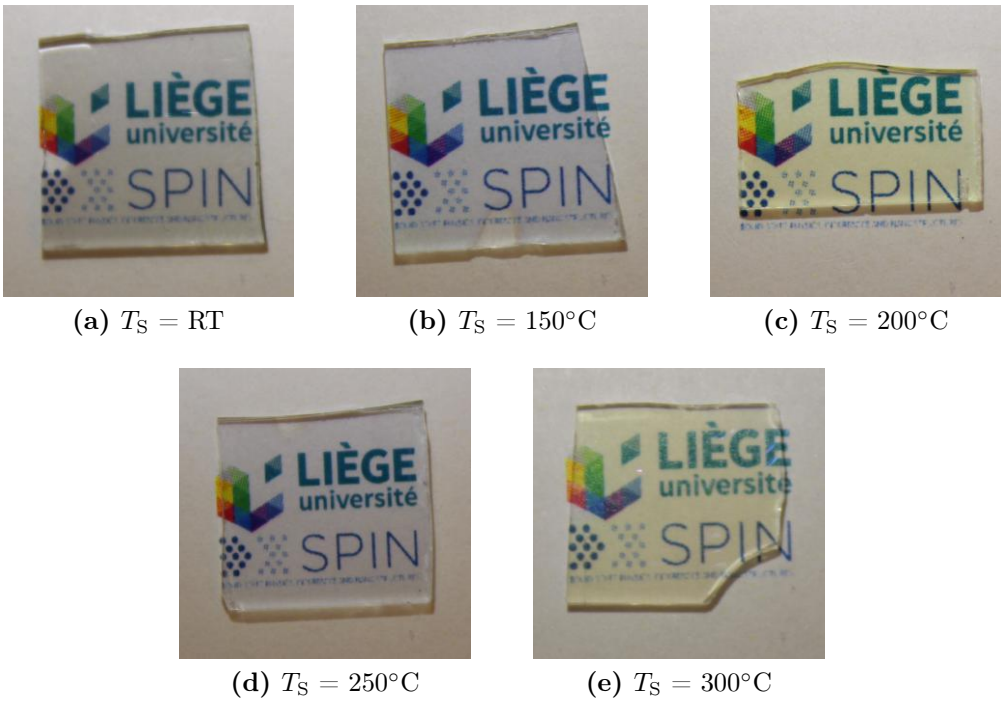

(a) T_S = RT **(b)** T_S = 150°C **(c)** T_S = 200°C

(d) T_S = 250°C **(e)** T_S = 300°C

Fig. 6.10: Photographies of AZO thin films deposited on glass substrate at a substrate temperature T_S of (a) RT=40°C, (b) 150°C, (c) 200°C, (d) 250°C and (e) 300°C.

As shown in Fig. 6.10, the optical transparency in the visible wavelength range can be evaluated by the visibility of the laboratory logo printed in color on a white paper. The qualitative transparent behaviour of the AZO thin films is quite net. In addition, the impact of the deposition temperature on this qualitative observation of the samples is quite limited. Concerning the sample deposited at RT, 150°C and 250°C, a slight blue shade is observed in comparison to the background uniform colour. The sample deposited at 200°C and 300°C a slight coloration which present a fade yellow reflect at the surface of the sample. In Figure 6.10b, the mark of the pin used to mechanically immobilized the substrate during the deposition is observed and the contrast between the glass substrate and the AZO-deposited glass is noticed.

6.2.2 ZnO:Al Thin Films Geometrical Characterization

Table 6.5 summarises the characterization results obtained for the AZO thin films deposited on glass substrate as a function of the substrate temperature. These ones are presented and interpreted throughout this section.

Sample ID	T_S [°C]	t_{Dektak} [nm]	ρ [Ωcm]	$\mathcal{T}_{vis}$ [%]	E_g [eV]
AZO-S2-1	RT	55	4.7×10^{-3}	67.70	3.43
AZO-S2-2	150	95	1.1×10^{-1}	81.18	3.34
AZO-S2-3	200	123	1.7×10^{-3}	83.92	3.55
AZO-S2-4	250	86	1.0×10^{-3}	81.26	3.53
AZO-S2-5	300	118	9.6×10^{-4}	77.23	3.56

Tab. 6.5: Cu_2O:Mg thin films resistivity and average transmittance in the visible wavelength range [400-800] nm.

Results of the thickness measurements of the AZO deposited thin films are presented in Tab. 6.5 as obtained from mechanical profilometry (Dektak). The surface surface profiles of the AZO films are shown in Fig. 6.11.

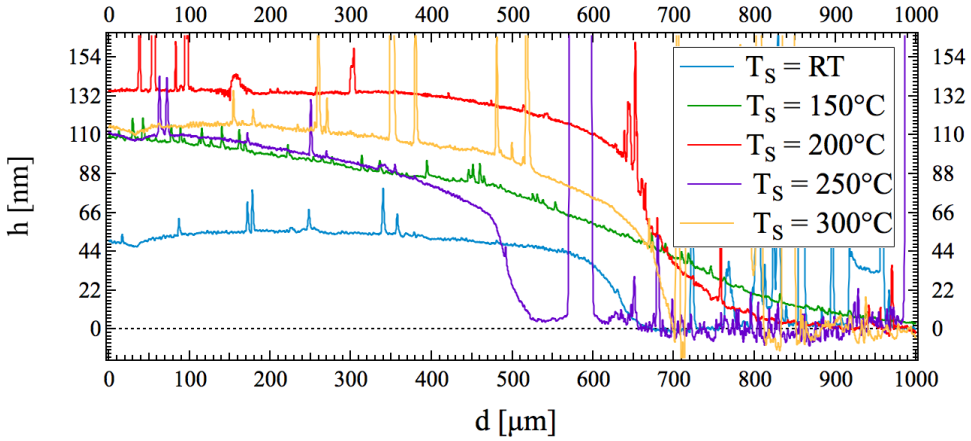

Fig. 6.11: Profilometry of the samples with AZO thin films deposited at 40°C, 150°C, 200°C, 250°C and 300 °C. d corresponds to the distance covered on the sample and h is the recorded vertical position of the profilometer tip in physical contact with the sample surface. h=0 corresponding to the substrate' surface height taken as reference for the measurement.

The film is quite uniform from a macroscopic point of view and its edge can be clearly identified. The large peaks observeable in the profiles correspond to the measurements of dusts particles present on the films due to the manipulations required to execute the measurement. The thickness values are used to calculate the electrical resistivity and the absorption coefficient. As explained in the previous section, the difference between the measured thicknesses and the expected ones given by the quartz crystal (cfr. Tab. 6.4) comes from the position of the samples on the substrate holder, due to on the one hand, the absence of rotation and on the another hand the erosion of the sputtering target caused by the large number of depositions performed. The electrical resistivity and the absorption coefficient are both intrinsic properties of the semiconducting materials which are independent of the geometry of the films.

In order to get an appreciation of the geometry of the deposited thin film and also to

observe this one at a microscale, SEM imaging was performed. In Fig. 6.19, cross-sectional views of the deposited films can be observed.

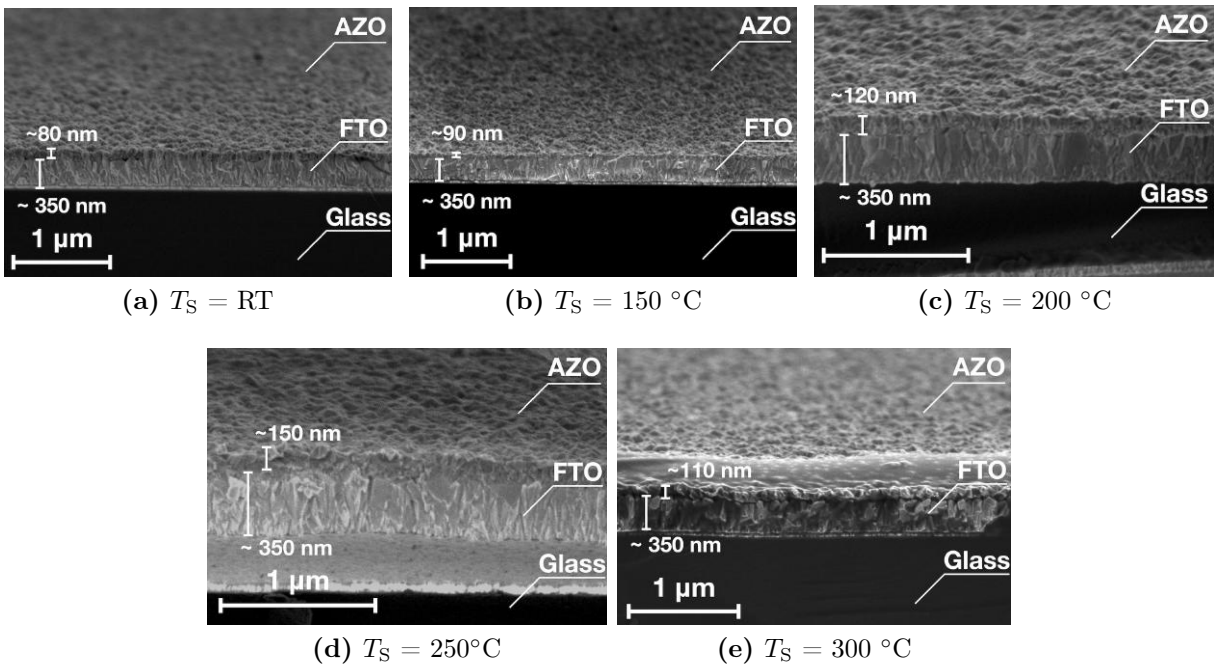

(a) T_S = RT **(b)** T_S = 150 °C **(c)** T_S = 200 °C

(d) T_S = 250°C **(e)** T_S = 300 °C

Fig. 6.12: Morphological characterization of AZO thin films deposited at (a) RT=40°C, (b) 150, (c) 200, (d) 250 and (e) 300 °C. By cross-section SEM imaging of the AZO deposited thin films deposited on FTO-coated glass subsrate. Images obtained at a working distance of 5 mm.

First of all, the contrast between the first layer made of FTO and the upper layer is less pronounced than with the Cu_2O:Mg thin film (cfr. Fig. 6.5). This is due to the relatively similar electrical sensitivity of AZO compared to the underlying FTO layer. Consequently the interaction with the electron beam in the SEM imaging process is also similar. Nevertheless, the frontier between both material can be still identified. The surface of the film seems to be uniform for all deposition temperatures. For T_S=300°C, a deteriorated layer is observed on a distance of several hundreds of nanometer. This observation could be related to the manipulation of the sample during the measurements and the cutting of this one. Concerning the crystallinity, three different types can be identified. First, at low deposition temperature, the film has an alveolar structure. Large grains of dimension around 120 nm exhibit some outgrown structure at their surface. Then, at 150, 200 and 250°C, another crystallographic structure is observed, the distinction between the grains is less easier, the shape of these ones is more polyhedral and the outgrown structure have disappeared. The surface roughness looks aslso reduced.

6.2.3 ZnO:Al Thin Films Electrical Characterization

Based on these first crystallographic observations of the deposited thin films, a good insight of the electrical and optical behaviour concerning the deposition temperature were obtained. For each deposition temperature, four AZO thin films samples were performed with the aim of applying RTA treatment on three of them. The annealing takes place in a nitrogen atmosphere at 250°C, 350°C and 500°C during 5 minutes. In Fig. 6.13a the

thin film electrical resistivity is presented as a function of the deposition temperature T_S while in Fig. 6.13b, the impact of the annealing temperature is highlighted.

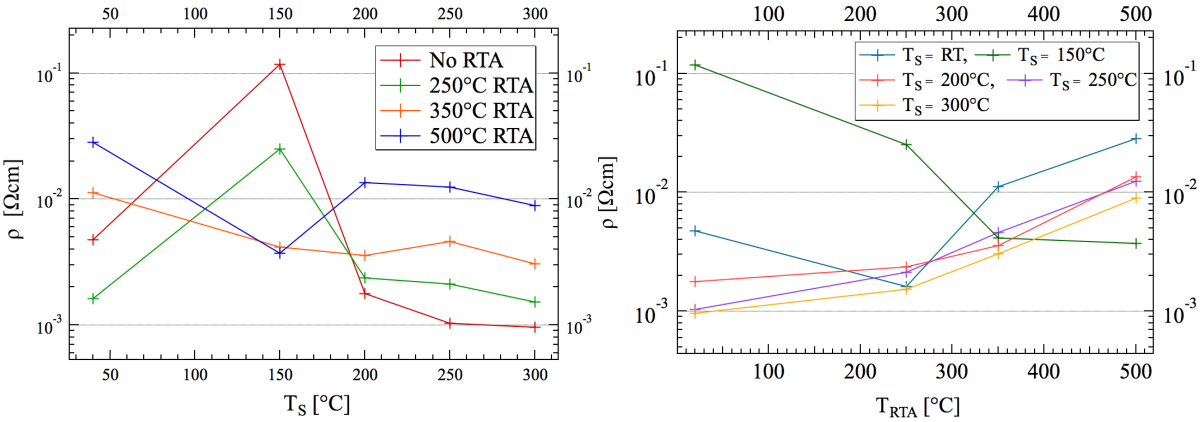

(a) Electrical Resistivity as a function of the deposition temperature T_S.

(b) Electrical Resistivity as a function of the annealing temperature.

Fig. 6.13: (a) AZO thin films resistivity as a function of the deposition temperature for 4 different RTA treatment applied (No RTA, 5 min RTA at 250°C, 5 min RTA at 350°C and 5 min RTA at 500°C) in nitrogen atmosphere. (b) AZO thin films resistivity as a function of the RTA temperature for 5 different substrate temperature (T_S= 40°C, 150°C, 200°C, 250°C and 300°C).

In a first part of this subsection, the resistivity of the thin film is presented as a function of the substrate temperature. and the RTA treatment temperatures. In the second part of this subsection, the interpretation of the resistivity variation is performed using the measurements of the majority charge carriers concentrations and mobilities.

In Fig. 6.13a, two regions can be distinguished. On the one hand, a decreasing of one order of magnitude in resistivity is observed between T_S=150°C and T_S=200°C without RTA. As the annealing temperature increases, this behaviour is reduced until 350°C and an inverting trend can be seen at 500°C-RTA where an increase in resistivity is observed between 150 and 200°C. Concerning the electrical behaviour below T_S=150°C, without thermal annealing and with RTA at 250°C, an increase in the resistivity was observed. In contrast, with RTA higher than 350°C, a decreasing resistivity was observed.

On the other hand, with and without thermal annealing, the electrical resistivity behaviour above 200°C is nearly the same with a slight decrease of the resistivity until T_S=300°C. Consequently, RTA with temperature higher than 350°C turns out to be beneficial for samples deposited at low temperature while for high deposition temperatures, a RTA a degradation in the thin film electrical behaviour for all annealing temperatures was observed. As evidenced in Fig. 6.13b, the films deposited at temperatures above 250°C have the same behaviour with a increasing electrical resistivity. For the film deposited at 150°C, a reduction of the resistivity was observed for all RTA temperatures. In contrast, at T_S=RT, a reduction of the resistivity is first observed at 250°C-RTA, while for higher RTA temperatures, the electrical behaviour of the thin film is worsened. In conclusion, **AZO thin film, with low electrical resistivity (9.6×10^{-4} [Ωcm]) could be grown at a substrate temperature of 300 °C without post-deposition annealing.**

In Fig. 6.14, the effect of the deposition temperature on majority charge carrier concentration and on the carrier mobility is shown for non-annealed AZO thin films.

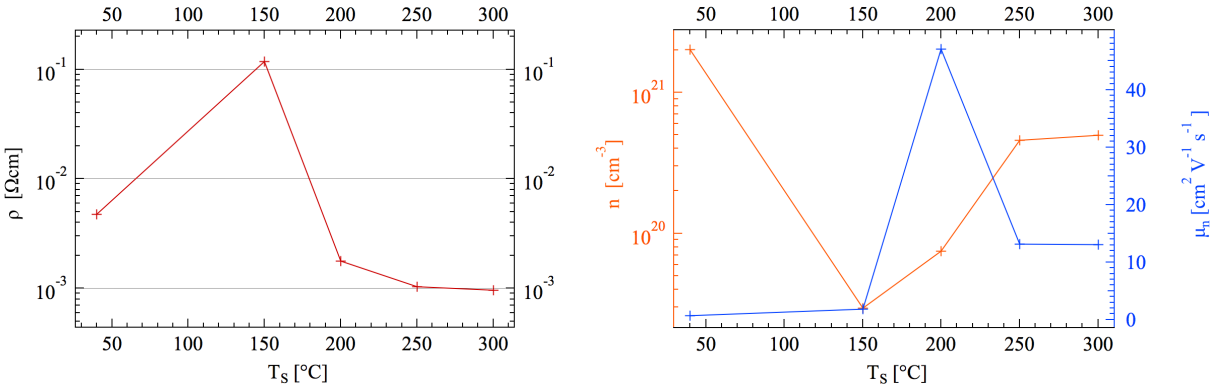

(a) Electrical Resistivity as a function of the deposition temperature T_S for as-deposited AZO films.

(b) Charge carrier concentration and mobility as a function of the deposition temperature T_S for as-deposited AZO films.

Fig. 6.14: Electrical characterization of AZO thin films deposited at RT, 150, 200, 250 and 300 °C without RTA.

The electrical resistivity behaviour as a function of the deposition temperature is a result of both the evolution of the majority charge carriers concentrations and their mobility. The Hall measurements first provide about the conductivity type (p or n) in the film. Then, as indicated in Fig. 6.14b, the charge carrier concentration drops from 2.02×10^{21} cm^{-3} to 2.93×10^{19} cm^{-3} between RT and 150°C. A two-order-of-magnitude reduction of the charge carrier concentration was observed while the charge carrier mobility is increased from 0.65 to 1.8 cm^2 V^{-1} s^{-1}. The combination of these effects result in the increase of the electrical resistivity. Then, between T_S=150°C and T_S=300°C, the abrupt reduction of the electrical resistivity can be attributed first to an increasing of the charge carrier concentration up to 4.9×10^{20} cm^{-3} and an increase of the charge carrier mobility followed by a saturation at 13 cm^2 V^{-1} s^{-1}. As reported in the results, the majority charge carrier concentrations are all above 10^{19} cm^{-3}. This observation highlights the fact the AZO is a degenerated semiconductor with a charge carrier concentration higher than N_C (cfr. Chapter 5) leading to a quasi-Fermi level associated to electron above the conduction band E_C implying an increase of the band gap energy width as explained in Chapter 2. As a result, the band gap energy obtained in the optical characterization of the thin films should be higher than the band gap energy of the undoped zinc oxide which is equal to 3.3 eV.

6.2.4 ZnO:Al Thin Films Optical Characterization

In this subsection, we present the results of the optical characterization of AZO deposited thin films. From a qualitative point of view, the observation of the annealed samples did not lead to any improvement (or degradation) on the transparency of the films. Based on the previous results, an optimal electrical resistivity, were obtained without annealing treatment of the films. As a consequence, the optical characterization was only performed on the non-annealed thin films. In Fig. 6.15, the transmittance spectra of the five non-

annealed AZO thin films is shown.

First, a baseline measurement was performed and the glass substrate transmittance data were collected as reference. As presented, this one reach 92 % of transmittance. This value is in agreement with values reported in the literature[3]. Then, the transmittance of thin films deposited on glass substrate were measured. A general observation is the that the transmittance range from 60 to 90 % was obtained for all deposited thin films between 400 to 2000 nm. Then, a rapid drop of the transmittance could be observed around 350 nm. This means that for the wavelength range below 350 nm, the light is either absorbed or reflected. A clear shift between the glass transmittance curve and the AZO thin film deposited samples transmittance curves can be observed. Such a wavelength shift is definitely attributed to the AZO deposited thin film. Due to optical interferences at different interfaces (AZO/air, AZO/glass or glass/air), transmittance of the system substrate/AZO film can exceed that of the glass substrate alone.

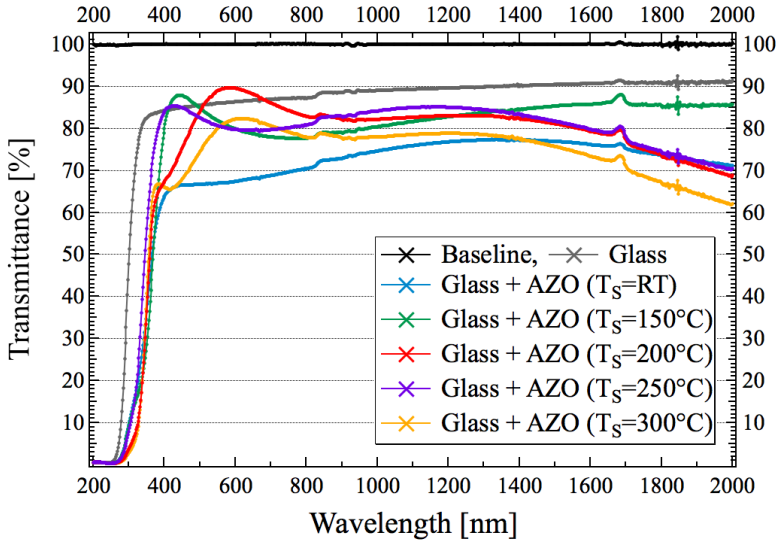

Fig. 6.15: Optical transmittance of AZO thin films deposited at RT, 150, 200, 250 and 300 °C as a function of the incident light wavelength.

Then, two sets of samples can be distinguished. The first one consists of the samples deposited at 200°C, 250°C and 300°C which show similar decreasing behaviours in the spectral region beyond 800 nm and which present a bump in the transmittance curve between 400 and 700 nm. This bump is also present for the AZO thin film deposited at 150°C but the decreasing behaviour at higher wavelength range is absent while it is the opposite for the film deposited at RT.

It can also be noted that samples deposited at temperatures between 150°C and 250°C show an average transmittance above 80% over the visible spectral range [400-800] nm.

In Fig. 6.16, the coefficient spectrum of the each different sample are presented. As presented, the energy band gap of the deposited thin films are respectively 3.43, 3.34,

[3]With 4% of reflection on each interface air/glass.

3.55, 3.53, 3.56 eV respectively for thin film deposited at RT, 150°C, 200°C, 250°C and 300°C.

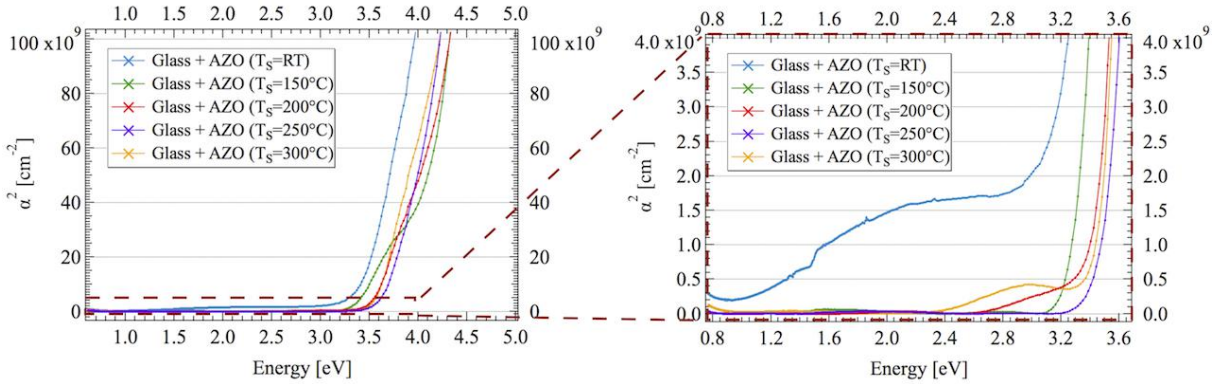

Fig. 6.16: Absorption coefficient spectra of AZO thin films deposited at RT, 150, 200, 250 and 300 °C. The band gap energy values were obtained by intersection of a linear extrapolation of the slope of α^2 curves with the energy axis as presented in Chapter 4 (cfr. Eq.(4.19)). Highlight of the impurity concentrations in the film deposited at a substrate temperature of RT=40°C. The absorption coefficients of AZO thin films have been calculated by taking into account the thickness and a refractive index n=1.820 based on the results obtained by Shantheyanda *et al.*[67]

From the viewpoint of electrical and the optical characteristics, one can draw a contrast between the AZO films deposited at temperatures below 150°C and those deposited at temperatures equal or higher than 200°C. On the one hand, a variation in the crystal quality can be hinted by the difference between band gap values [3.43, 3.34] eV corresponding to the films deposited at T_S below 200°C and [3.55, 3.53, 3.56] eV corresponding to the film deposited at a temperature higher than 200°C.

Furthermore, a closer analysis of the absorption coefficient spectra allows us to point out features that specifically relate the possible effects due to crystal defects. Indeed, for AZO deposited at 40°C, bumps in absorption were recorded in the photon energy range [0.8-3.2] eV. For higher substrate temperature, the amplitude of these bumps is reduced and the photon energy range concerned is restricted to [2.4-3.2] eV.

In Section 6.1), we have explained that, in the case of Cu_2O:Mg, the presence of these bumps highlight the lack of crystallinity of the deposited films. Indeed, an absorption coefficient value higher than correspond to an energetic value for which photons absorption could take place. Two cases must be taken into account. First, for photon energy higher a E_g, the absorption occurs with a transfer of additional kinetic energy to the EHP. Secondly, for energies lower than the band gap energy, absorption are prohibited in a perfect crystal. Concerning the observations realised in Fig. 6.16, especially for AZO thin films deposited at RT, photon absorption is likely to take place through defect levels within the band gap (at an energy lower than E_g.

Based on the analysis of the electrical and optical characteristics of the AZO thin films, the evolution of the properties of this material as a function of the deposition temperature could be explained in a comprehensive way. With the same motivation than in Section 6.1, a figure of merit corresponding to the ratio between the average transmittance in

the visible wavelength range ([400-800] nm) and the electrical resistivity can be used to determine the optimal deposition temperature in order to obtain the most efficient AZO thin film in terms of transparent conducting material. The figure of merit is plotted as a function of the substrate temperature and presented in Fig. 6.17.

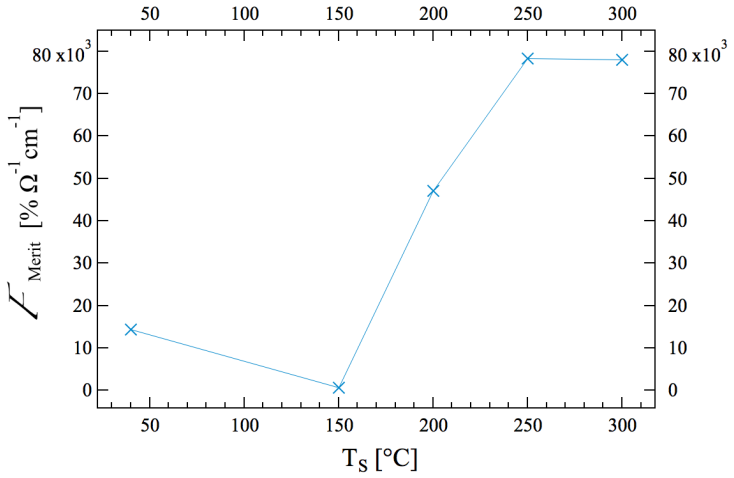

Fig. 6.17: Figure of Merit of AZO thin films as a function of the deposition temperature T_S as deposited.

As presented, first a degradation of the TCO properties is observed as the deposition temperature increases due to the increase of the electrical resistivity. Then, between 150°C and 250°C, the efficiency drastically increases due to an improvement of the electrical conductivity while the transmittance characteristic remains nearly constant. **The AZO thin film obtained with a deposition temperature of 250°C shows the most promising characteristics as a transparent conducting material.**

6.2.5 ZnO:Al Thin Films Morphological Characterization

In order to confirm the morphological modifications of the deposited thin films concerning the deposition temperature described in the previous subsection, SEM imaging of the samples from top view are presented in Fig. 6.19.

The SEM images presented are first described and then compared to the modified Thornton' structure zone model presented in Fig. 6.18. In this structure-zone model, O. Kluth *et al.* [68] motivates the axis inversion compare to the Thornton model presented in Chapter 3 [33] for metallic thin films by the fact that for AZO, the most influent parameter on the thin film crystallinity is the argon pressure. As a consequence, the substrate temperature and the Ar pressure axis has been inverted. This axis inversion can be understood by the fact that the Thornton' structure-zone model is a model initially presented for metallic compounds. It was therefore not specifically designed to describe the growth of semiconducting materials. Moreover, the evolution of the morphology as a function of the deposition temperature and the argon pressure is not always linear or unique for all materials. The same crystallinity can be achieved either with a high temperature and a low argon pressure or either with a high argon pressure and a low temperature. The investigation performed by O. Kluth *et al.* [68] was to determine which parameter is the

most influent.

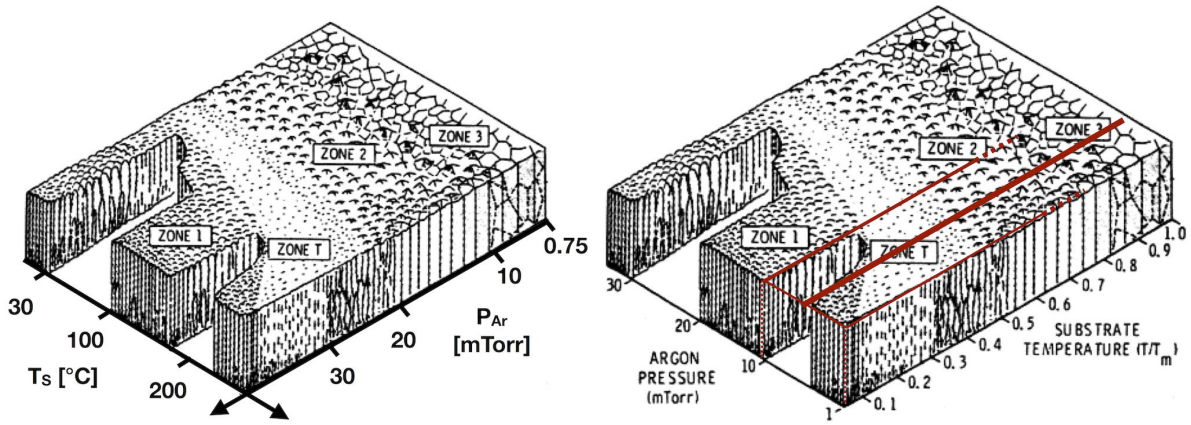

(a) Modified Thornton' structure-zone model for AZO thin films [68]. **(b)** Original Thornton' structure-zone model [33].

Fig. 6.18: Original [33] and modified Thornton' structure-zone model for AZO thin films [68]. The modified Thornton' structure-zone model implies an axis inversion due to the higher impact brought by the substrate temperature on the crystallinity of AZO thin films [68].

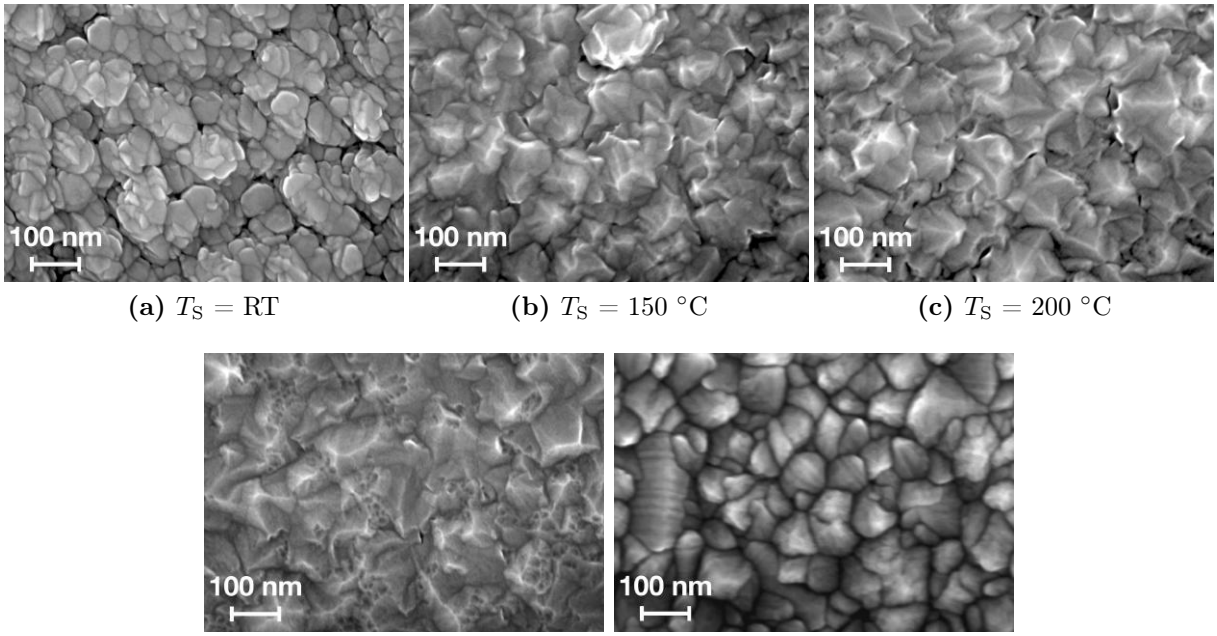

(a) T_S = RT **(b)** T_S = 150 °C **(c)** T_S = 200 °C

(d) T_S = 250°C **(e)** T_S = 300 °C

Fig. 6.19: Morphological characterization via top view SEM imaging of the surface of AZO thin films deposited at (a) RT, (b) 150°C, (c) 200°C, (d) 250°C and (e) 300 °C obtained at a working distance of 5 mm.

As shown in Fig. 6.19, three types of crystalline structures can be observed. First at RT, an alveolar structure is observed with grains dimension of nearly 100nm. This

confirm the results reported in a previous subsection concerning the cross-sectionnal SEM images. These grains are separated by large voids, which can lead to the large resistivity of AZO thin films deposited at RT compared to higher deposition temperatures. Then, at T_S=150°C, this alveolar structure disappears and the facets and angles of the grains gets sharpener as the deposition temperature increases. Between 150°C and 250°C the voids between the grains gradually disappear and a most compact crystalline structure is achieved for T_S=250°C. This observation highlights the fact that the electrical resistivity of AZO thin films is higly dependent on the film morphology, with a substantial contributions from boundaries and space between grains. Finally, at T_S=300°C, a structure with smaller grains was observed, with dimensions of the order of 50 nm. Compare to the Thornton's models presented in Fig. 6.18, the thin film deposited at RT corresponds to a zone 1 material in the original Thornton model. Then, between 150°C and 250°C, the crystalline structure corresponds to a regime between zone 2 and 3 in the modified Thornton model presented by O. Kluth *et al.* [68]. And finally, at T_S=300°C, a zone 3 structure is observed with an improvement of the crystallinity implying an improvement of the conductivity.

In Fig. 6.20, the first image corresponds to the observation of a crack in the glass substrate leading to this perspective landscape. Furthermore, at the bottom part of the images, the glass bare substrate can be observed. The second image shows a peeling of the FTO and AZO layers off the glass substate. This deformation is due to the breaking of the sample in order to obtain a cross-sectional view and to the usage of metallic tweezers for the manipulation of the sample.

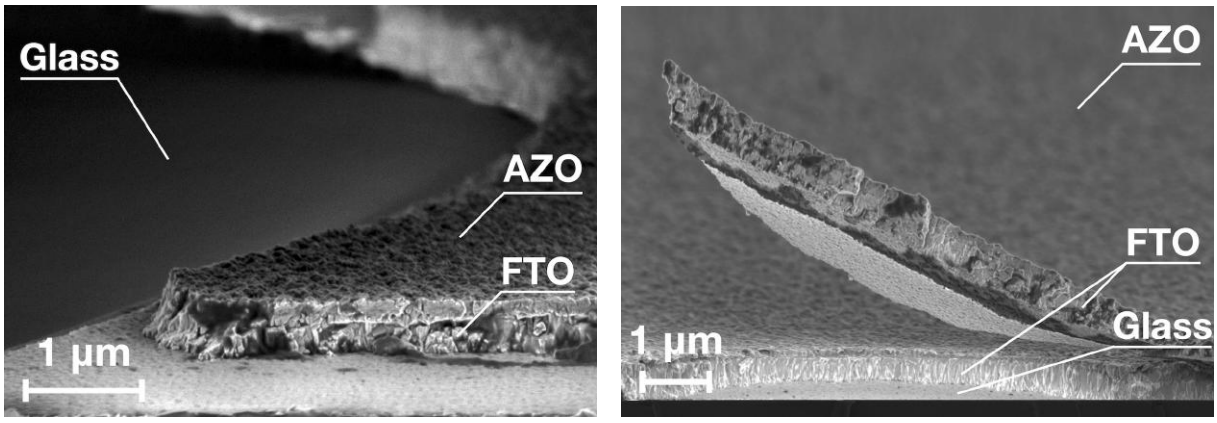

Fig. 6.20: AZO deposition SEM imaging interesting views. Respectively obtained at a working distance of 5 mm and 5.1 mm

In the following section, the fabrication of the heterojunctions is performed based on the results obtained in Sections 6.1 and 6.2.

6.3 Heterojunctions

The actual section is dedicated to the realization of the AZO/Cu_2O:Mg heteojunctions. We report first on the fabrication of the heterojunctions by successive depositions of thin films and metallic contacts (cfr. Section 6.3.1), then on the characterization of the PN-junctions (cfr. Section 6.3.2).

6.3.1 ZnO:Al/Cu_2O:Mg Junctions Fabrication

Concerning the results presented and interpreted in Sections 6.1 and 6.2, two configurations of junctions were selected and studied. First of all, as presented in Fig. 6.21, a 150nm-thick AZO layer is deposited at 250°C on a FTO coated glass substrate. An ohmic contact is assumed between the FTO and the AZO layers. Several arguments motivate the choice of AZO thin film as first layer. First, in order to avoid the formation of a rectifying junction between the p-type Cu_2O:Mg and the n-type FTO layer, this configuration is preferred. Secondly, the necessity of a rectifying junction in order to improve the efficiency of the electroluminescence phenomenon. As explained in Chapter 2, the electroluminescence efficiency increases thanks to the formation of the rectifying junction between both semiconducting materials and the confinement of the electrons as minority carriers in the Cu_2O:Mg layer. However, in the case of Cu_2O:Mg layer deposited first, the high temperature used for the deposition of AZO could lead to a rearrangement of the previously deposited thin film and also to diffusion of zinc and oxygen atoms within the Cu_2O:Mg. This phenomenon would consequently lead to a degraded interface consisting in a layer of Cu_2O:Mg, a mixed region of cuprous oxide and zinc oxide and finally a layer of AZO. This situation is prevented by the deposition of a first layer of AZO and a second layer of Cu_2O:Mg. Finally, the high transmittance characteristic of AZO prevents the absorption of the photons generated by the recombinations in the p-type semiconductor.

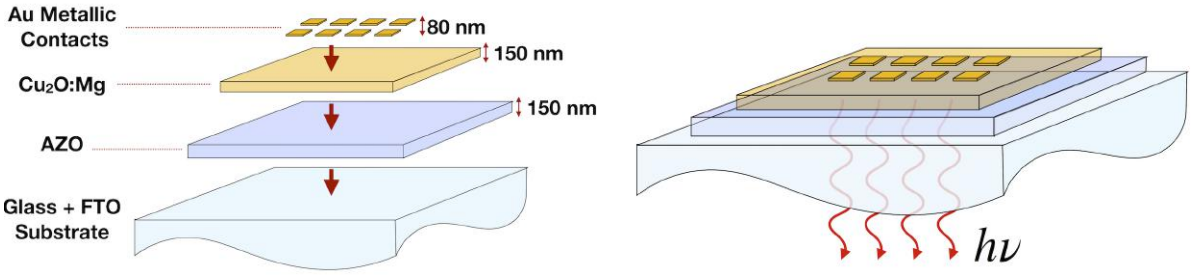

Fig. 6.21: Schematic representation of the heterojunctions. The PN-junction is deposited on a glass substrate coated with FTO. Metallic contacts, with typical thickness of 80 nm, are deposited above the junction in order to apply an external bias between both of these conductive layers.

In order to highlight the effect of the interface quality, which was previously described, two different processes of Cu_2O:Mg deposition are selected. In the first configuration, Cu_2O:Mg is deposited at RT. The choice aims at obtaining an optimal rectifying junction with the lowest achievable electrical resistivity. However, in this case the transmittance, of the film is quite poor (cfr. Section 6.1). In the second configuration, the Cu_2O:Mg layer is deposited at 200°C. In this case, a particular attention to the rectifying behaviour of the junction is required and an interesting comparison with the previous configuration is performed. Furthermore, no annealing study has been applied on Cu_2O:Mg due to its

position as second layer in the PN-junction. The parameters of the deposition for each semiconducting thin films are presented in Tab. 6.5.

Sample ID	T_S [°C]	P [Torr]	$\mathcal{P}$ [W]	DR [Ås^{-1}]	P_{Ar} [mTorr]
AZO-250	250	3.61×10^{-8}	63	0.25-0.28	5
Cu_2O:Mg-RT	RT	4.65×10^{-8}	51	0.3	5
Cu_2O:Mg-200	200	4.88×10^{-8}	57	0.3	5
	200	7.2×10^{-8}	57	0.3	5

Tab. 6.6: Deposition parameters of the thin film deposited by RF magnetron sputtering on a FTO-coated glass substrate in order to realise the PN-junction.

As it was highlighted in the previous sections, the impact of a slight variation in the deposition parameters induces non-negligible modifications of the thin films properties. The depositions are performed on FTO-coated glass substrates with an argon pressure of 5 mTorr and a constant argon flux of 20 sccm. As presented in Fig. 6.7, the positions of the samples on the substrate holder have been carefully chosen and thanks to the results of the thickness investigation carried out in Section 6.1, the deposition times have been adapted to obtain a targeted thickness value of 150 nm per film. A rotation of 2.5 rpm is applied in order to prevent the thickness issue presented in Section 6.1. For the PN-junctions, a minimal thickness value of 150 nm was aimed for two reasons: on one hand the presence of the depletion region at the interface, on the other hand the presence of neutral regions in both deposited layers. Indeed, these neutral regions facilitate the injection of sufficient free charge carriers to induce radiative recombination and thus electroluminescence.

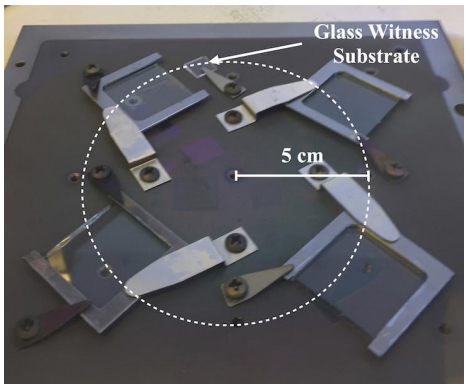

(a) Annotated substrate holder.

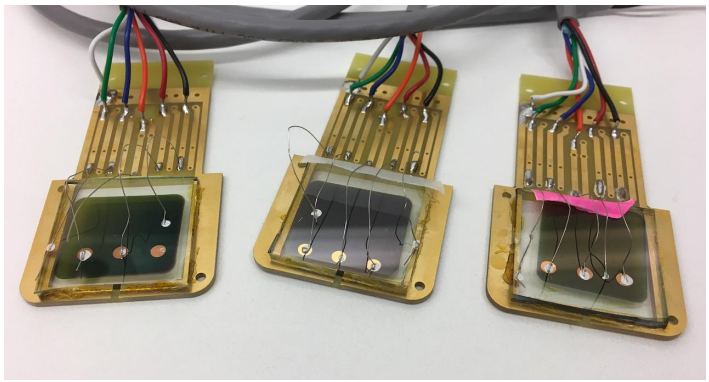

(b) View of the fabricated devices connected on the test holders.

Fig. 6.22: (a) Annotated picture of the holder with substrates to be processed. (b) Heterojunction devices glued on test holders used to connect the metallic contacts in order to perform the electrical characterization of the PN-junction.

In Fig. 6.22b, a photography of the PN-junctions is presented. The first one (left) consists in a 300nm-thick AZO-250/Cu_2O:Mg-RT (150 nm for each layer) and the other

ones (centre and right) are made of a 300nm-thick AZO-250/Cu_2O:Mg-200 deposited in two times. This successive deposition for the Cu_2O:Mg layer in order to reach the 150 nm of thickness will be taken into account in the following study. In the literature, Pushpa *et al.* [69] reported the effect of a two-step deposition in comparison to a direct deposited by observing a larger grain size for a two-steps deposition process.

For both configurations, 80nm-thick gold metallic contacts are deposited at the top of the device for the electrical connection to an external power supply. These gold metallic contacts are deposited using a thermal evaporation deposition process. In this deposition technique, the source material is placed in a tungsten boat trough which a high current is injected (over $\sim$ 100 A). Induced by Joule effect the melting and evaporation of the source material occur in the vacuumed deposition chamber. Then, thin tin wires are connected to the gold metallic pads using a silver paste[4]. The second contact is established on the FTO layer with the same technique. The silver paste has a sheet resistance of 0.02 $\Omega/\square$.

In the following section, the optical and electrical characteristics of the layer which composed the junctions are presented. Finally, the PN-junction is characterized and the results are interpreted in comparison the numerical simulations results (cfr. Chapter 5).

6.3.2 ZnO:Al/Cu_2O:Mg Junctions Characterization

In order to obtain an insight into the thin film properties of the layers within the PN-junctions, glass substrate samples are placed together on the sample holder (cfr. Fig. 6.22a) and then characterized. The optical and electrical characterization of the witness samples is summarised in Tab. 6.7. In order to complete the study, after a first characterization, the AZO-250 witness sample was annealed during three hours (deposition time of Cu_2O:Mg) at 200°C in vacuum conditions (6×10^{-8} Torr) and characterized a second time. This investigation was performed in order to simulate the annealing received by the AZO layer during the deposition of Cu_2O:Mg at high temperature. Nevertheless, the annealing does not fully recreate the complete conditions of the Cu_2O:Mg deposition. However, it provides a good insight of the AZO thin film properties after the high temperature deposition of the cuprous oxide.

Sample ID	$T_{\text{annealing}}$ [°C]	t_{Dektak} [nm]	ρ [Ω cm]	$\mathcal{T}_{\text{vis}}$ [%]	E_{g} [eV]
AZO-250	/	165	6.5×10^{-4}	71.91	3.55
AZO-250	200	165	6.0×10^{-4}	71.16	3.55
Cu_2O:Mg-RT	/	160	5.2×10^{-1}	23.26	2.05
Cu_2O:Mg-200	/	145	$\sim 10^3$	24.55	2.20

Tab. 6.7: Results for of the thickness, the resistivity, the average transmittance in the visible wavelength range and the band gap energy of the different layers composing the PN junctions.

[4]Further information on the silver paste can be found at the following reference: `https://www.electrolube.com/products/maintenance-service-aids/detail.html?pid=scp&section=farben_und_farbentferner?pid=scp&section=farben_und_farbentferner//` visited on May 25, 2018.

In comparison to the AZO thin film results (cfr. Section 6.2), the AZO-250 resistivity decreased from 10.3×10^{-4} to 6.5×10^{-4} Ωcm. This electrical improvement can be attributed to the lower deposition pressure that could be reached for the AZO deposition of the heterojunction. Concerning the average transmittance in the visible wavelength range, a value of 71.91 % was achieved. A decrease of less than 10% is consequently observed in comparison to the previous result (81.26 %). This decrease can be attributed to the increase of the thickness. Then, the band gap energy calculated base on the transmittance measurement yields a value of 3.55 eV with a refractive index of 1.82 [67]. Furthermore, as presented in Fig. 6.23b, a good crystallinity of the AZO thin film is obtained. Indeed, the absorption coefficient curve presents a drastic decrease at 3.55 eV and is nearly 0 for lower energy values. Concerning the impact of the annealing process, a slight decrease in the electrical resistivity was observed while the optical properties remained nearly constant. As investigated by Chang *et. al.* [49], annealing treatment under vacuum is beneficial for the properties of AZO as a TCO.

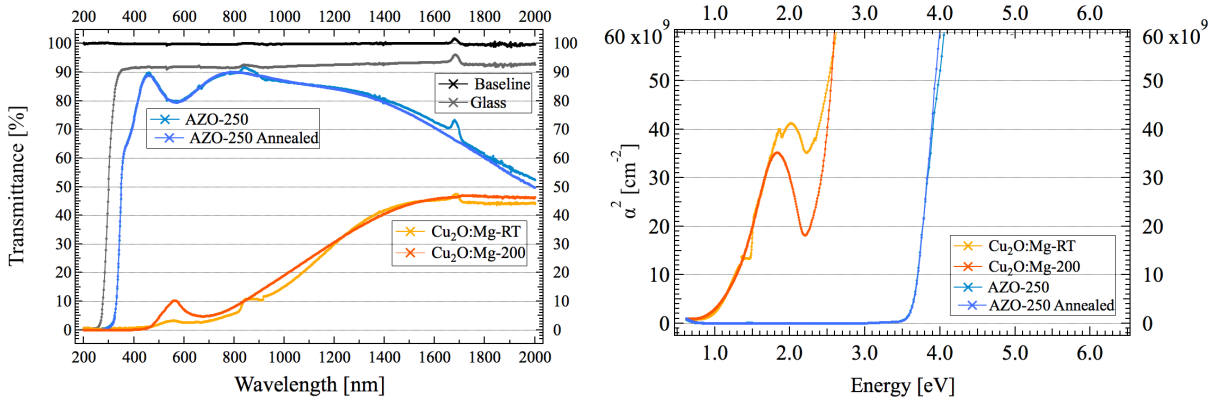

(a) Witness samples transmittance spectra. **(b)** Witness samples absorption coefficient spectra.

Fig. 6.23: Transmittance spectra of the PN-junction successive layers between 200 and 2000 nm and their related absorption coefficients.

Concerning the characterization of Cu_2O:Mg layers, an improvement of the electrical conductivity of Cu_2O:Mg deposited at RT is observed. The resistivity decreased from 16.3 to 0.5 Ωcm. This improvement can be related to the lower deposition pressure. In opposition, for Cu_2O:Mg deposited at 200°C, an increasing of the resistivity is observed. This result can be related to the deposition procedure performed in two times. Nevertheless, as explained in Section 6.1, the electrical measurement of Cu_2O:Mg thin films deposited at high temperature was hardly reproducible due to the low accuracy of the VdP measurement instrumentation for high resistive thin films. Concerning the optical property of the measured films, as presented in Fig. 6.23a, a decrease of the transmittance is observed for both deposition temperatures, from an average transmittance of 21.06 % to 23.26 % for Cu_2O:Mg deposited at RT and from 44.43 % to 24.55 % for Cu_2O:Mg deposited at 200°C. As explained in the previous section the difference between the transmittance level of both films comes mainly from the thickness difference (78.3 nm for T_S=RT and 50 nm for T_S=200°C). Indeed, a thinner film has a higher transmittance due to the exponential behaviour of the absorbance with respect to the thickness in Beer-Lambert's law (cfr. Eq.(2.56)). In this case, the deposited layers have a thickness of 160 nm and 145 nm, respectively for a deposition temperature of RT and 200°C. The thinner film also has the

lowest average transmittance. The impact of the thickness can also be observed in Fig. 6.23b. Indeed, in comparison to the Cu_2O:Mg thin films results (cfr. Section 6.1), the values of the energy band gap obtained for the same deposition temperatures are substantially lower. This result corroborates the observation of M. Rasadujjaman *et al.*[70] who observed a decreasing of the band gap energy as a function of the thickness. This result is important in this study due to the fact that the band gap value of the Cu_2O:Mg material determines directly the energy of the photons emitted. In this case, the electroluminescence occurs at a wavelength of 604 nm and 563 nm respectively for Cu_2O:Mg deposited at RT and at 200°C. In addition, a bump in the absorption coefficient curves is observed for lower energies. These bumps highlight a lower crystallinity quality and consequently the presence of defects within the films and/or imperfections at material interfaces such as atomic interdiffusion. These defects could lead to presence of electron states within the band gap associated to transitions of lower energies (longer wavelengths). A poorer crystallinity is observed for Cu_2O:Mg deposited at RT. As presented, the impact of the thickness on the optical properties of Cu_2O:Mg thin films can certainly not be neglected.

In the following part of this section, the characterization of the PN-junctions fabricated is performed. In Fig. 6.24, cross-sectional view images of the AZO-250/Cu_2O:Mg-RT PN-junction are presented.

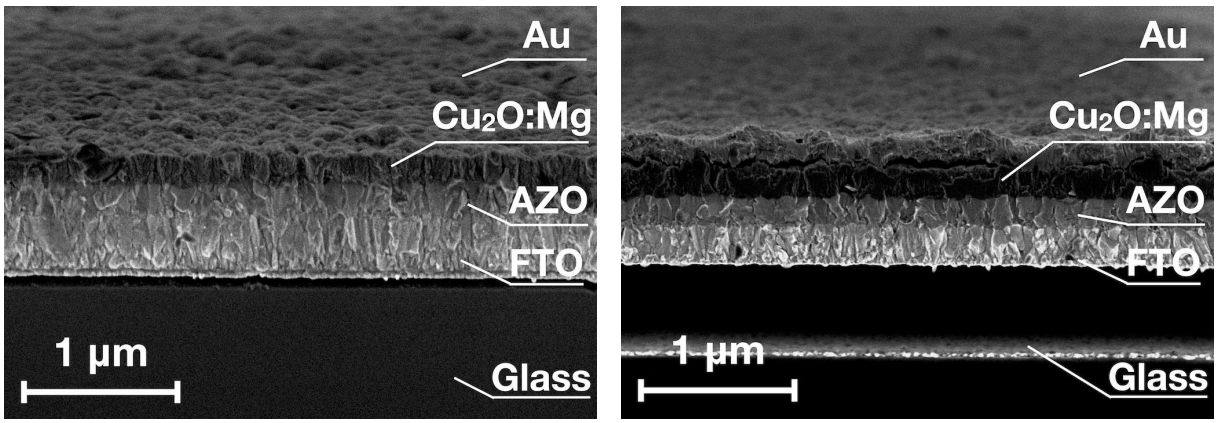

(a) Without metallic gold contacts **(b)** With metallic gold contacs

Fig. 6.24: Morphological characterization of AZO-250/Cu_2O:Mg-RT PN-junction. SEM cross-sectional view imaging obtained with a working distance of 2.9 mm. From the bottom to the top, the glass, an insulating layer, the FTO, the AZO and the Cu_2O:Mg can be observed.

As presented in Fig. 6.24a, the bottom of the image consists of the glass substrate (black), a thin insulating layer, and the 300 nm of FTO which compose the coated substrate. The deposited layer stack comprises the AZO film, which is slightly more contrasted than the FTO. Both materials have a low electrical resistivity leading a similar grey shade in the SEM imaging. The columnar structure of the AZO can be observed and this one is comparable to the one observed in the AZO thin film characterization. The cross-sectional view shows that the columnar growth of the AZO layer follows the directional structure of the underlying FTO. The darker layer is the cuprous oxide which has a higher electrical resistivity than the other layers. Concerning the structure, columns seem to match with the ones of the previously deposited AZO layer. At the surface, an

alveolar morphology and a apparent roughness were reported. These observations reinforce the ones performed in the previous characterization. In Fig. 6.24b[5], the last layer is the gold metallic contact. As it can be observed, this one tends to follow the roughness of the Cu_2O:Mg layer.

In Fig. 6.25, views of the AZO-250/Cu_2O:Mg-RT PN-junction are presented. These cracks, overturns and uprisings come from the cut of the sample before the acquisition of the SEM imaging.

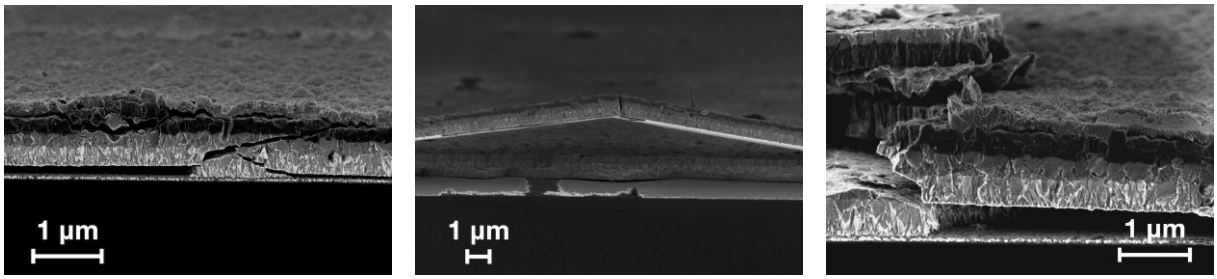

(a) Cracks in the successive layers resulting of the sample cutting.

(b) FTO and deposited layers uprising from the glass substrate.

(c) Thin films overturn from the FTO coated glass substrate.

Fig. 6.25: SEM cross-sectional view imaging of the AZO-250/Cu_2O:Mg-RT PN-junction obtained with a working distance of 2.9 mm.

In the next step, the results of the electrical characterization of the PN-junctions are presented. As indicate earlier, measurements were performed by using the gold metallic contacts previously deposited. However, by using this configuration, an ohmic behaviour of the current density voltage curve is observed for both PN-junctions (Fig. 6.26).

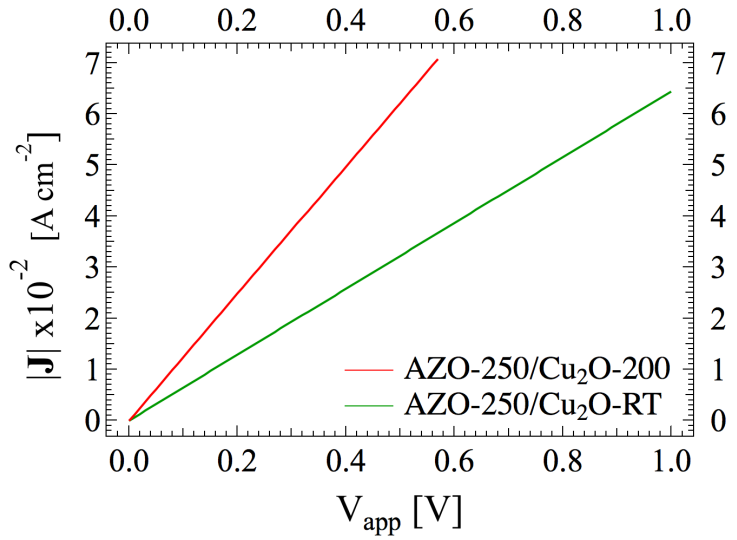

Fig. 6.26: Current density-voltage characteristics of AZO-250/Cu_2O:Mg-RT and AZO-250/Cu_2O:Mg-200 PN-junctions measured using the gold metallic electrical contact.

[5]The figure presented in the front cover of this master thesis report consists in an artificially colorised SEM image of this AZO-250/Cu_2O:Mg-RT PN-junction.

During the current-voltage measurements, a limited current of 5 mA was set to prevent the breakdown of the PN-junction. Indeed, Joule heating associated to excessive current densities can lead to non reversible undesired modifications of the film structure. In order to determine the current density, the measured current is divided by the area of the gold metallic contact (0.07068 cm^2). Figure 6.26 is an evidence for the ohmic behaviour of the current-voltage measurement. The resistance measured is of the order of 4.55×10^{-2} Ω and 8.7×10^{-2} Ω respectively for the AZO-250/Cu_2O:Mg-RT and the AZO-250/Cu_2O:Mg-200 junctions. The difference between the two junctions comes from a weak difference in thickness and from the difference of transport properties between the Cu_2O:Mg layers. One way to explain the ohmic behaviour is to point out the diffusion of gold atoms within the PN-junctions, which act as a short-circuit path through the junction. In order to confirm this hypothesis, Time of Flight Secondary Ion Mass Spectroscopy (TOF-SIMS) measurement can be used in order to determine the Au concentration as a function of the depth in the PN-junction.

A second set of current-voltage characteristics was obtained by making an electrical contact between a $12\mu m$-tungsten[6] tip and the surface of the Cu_2O:Mg. Using this configuration, a rectifying behaviour of the junction was determined.

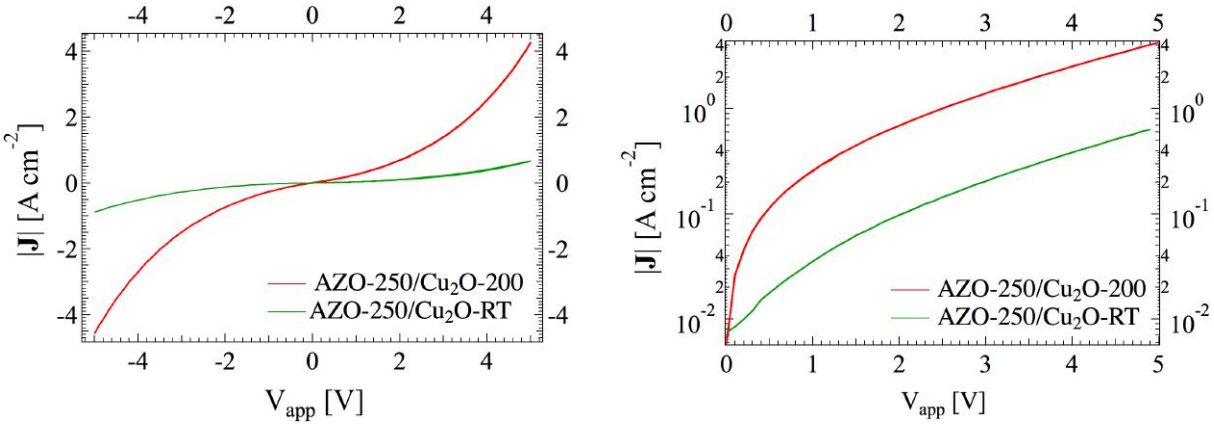

Fig. 6.27: Current density-voltage characteristics of AZO-250/Cu_2O:Mg-RT and AZO-250/Cu_2O:Mg-200 PN-junctions determined using a contacted tungsten tip on the Cu_2O:Mg layer as electrical contact.

As shown in Fig. 6.27, the rectifying behaviour of the PN-junction using a high deposition temperature for the cuprous oxide is improved in comparison to the AZO-250/Cu_2O:Mg-RT junction. Concerning the current density values, possible errors can be induced by the contact surface of the tungsten tip, depending on the sharpness of this one. As observed in the logarithmic representation of the JV characteristic, the depletion region dominates the behaviour of the PN-junction, while over V_{app}=1 V, a linear increasing of the current density is observed. This observation is related to a dominance of the neutral region over the PN-junction behaviour. However, in comparison to the numerical results, current density in this saturation region is lower. This can be explained, by the presence of defects in the layers, the non-ideality of the PN-junction manufactured or the presence of contact resistances inherent to the experimental process of measurement. These effects

[6] $12\mu m$ correspond to the diameter of the tip.

consequently reduce the total current obtained through the PN-junction. The shape of the JV characteristic under reverse bias, is generally explained by a combination of diffusion current and leakage current. Indeed as presented in Section 4.1, several artefacts have to be recognized when performing transport measurements on a PN-junction. The origin of leakage currents comprises the transport of charge carriers through defect bands [71]. The existence of such additional energy bands, within the material energy gap, was found in non epitaxial interfaces as well as in junctions with evidence of atomic interdiffusion such as metal semiconductor contacts.

As hinted in the analysis of the electrical characteristics of the studied heterojunctions, several additional investigations need to be performed in order to complement the interpretation of the results obtained for the Cu_2O:Mg/ZnO:Al junctions. The perspectives of improvement of this study include:

- The quantitative impact of the contact resistances in comparison to the series resistance of the material and consequently a more detailled study of the metallic contact in order to reduce this interface resistance. Depositions and characterizations of the efficiency of different metallic materials by using different depositions techniques could be performed to that perspective.

- The study of the leakage current through the PN-junction and the investigation of the sharpness of the interface. Additional analysis by secondary ions mass spectrometry (TOF-SIMS) would enable an investigation of the atomic concentrations as a function of depth.

- A study of the different interfaces in presence. Indeed, in this work, the investigation has been focus on the PN-junction formed between the aluminium doped zinc oxide and the magnesium doped cuprous oxide. Nevertheless, during the electrical measurement, an interface is created between the FTO and the AZO and between the metallic contact and the cuprous oxide layer. These interfaces have been assumed to be ohmic all along this work. However, the JV characteristics can also be impacted by the formation of a Schottky interface depending on the electronic affinity of the metal used for the contact.

As a conclusion for the part of this work dedicated to the electrical characterization, the fabrication of a rectifying PN-junction has been achieved based on the independent optimisation of the deposited thin films. In addition, an improvement of the rectifying behaviour has been observed for a higher deposition temperature of the cuprous oxide on the AZO thin film. Complementary analyses would help in the identification of the physical origin of junction leakage.

In the last part of this section, the optical characterization of the junction is completed by the measurement of the emission spectrum as presented in Chapter 4. Nevertheless, in order to measure the emission spectrum of the manufactured junction LED a thorough study of the metallic contact at the surface of the structure is required in order to develop permanent metallic contacts. An investigation of the deposition of several metallic materials (such as silver, nickel, gold, *etc.*) using different deposition techniques (such as electron beam deposition, thermal vapour deposition, *etc.*) is required to establish perma-

nent contacts to the junction. The use of the wirebonder[7] available at the nanofabrication platform can also be used to create permanent electrical connection. However, using gold contacts, the usage of this machine was not beneficial for the electrical contacts due to the removal of the gold deposition based on Malier's experience [44]. In order to compare the emission spectrum determined using the numerical resolution of the PN-junction, the measurement of a green GaP LED[8] is performed. The emission spectrum obtained by using the experimental protocol established in Section 4.2 is shown in Fig. 6.28. The light intensity $\mathcal{I}$ [cd] of the LED is comparable to the value reported in the manufacturer's datasheet, with a typical intensity of the order of 200 mcd located at a photon energy of 2.18 eV.

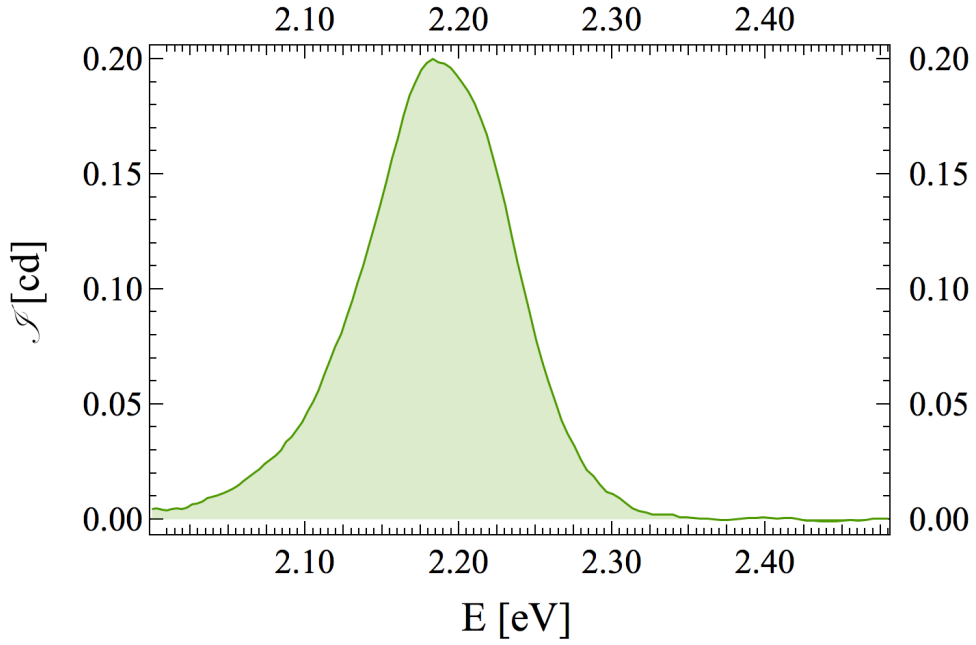

Fig. 6.28: Emission spectrum of the L-53SGC super bright green LED.

The peak location is only slightly shifted by 0.01 eV with respect to the referenced one. In comparison to the emission spectrum calculated with the numerical simulation results, the maximum intensity of the LED is one order of magnitude below. This observation is not surprising and several hypotheses were presented in Chapter 5. Furthermore, the shape of the emission spectrum presents some differences compared to the theoretical curve. This is mainly due to the encapsulation of the junction material in the LED packaging. Indeed, optical absorption, reflection and interference taking place at the different materials interfaces can lead to a modification of the emission spectrum shape.

[7]Further information on the wirebonder available in the nanofabrication platform can be found at the following reference: `http://www.mpptools.com/ibond5000-wedge`

[8]Further information the LED measured can be found using the following reference: KINGBRIGHT® L-53SGC SUPER BRIGHT GREEN.

Chapter 7

Conclusion and Perspectives

This final thesis was divided in two parts: the one-dimensional numerical simulation and the experimental fabrication and characterisation of the ZnO:Al/Cu_2O:Mg heterojunction. Both parts were supported by a theoretical background as well as technical details of the experimental protocol.

The results obtained in the numerical simulation of the PN-junction are in good agreement with the theory developed in Chapter 2. First, the iterative usage of the solution obtained at the previous bias calculation as guessed solution for the current calculation led to the improvement of the convergences. **Results for the band diagram, the charge carrier concentrations, the depletion width and the band to band recombination rates as a function of the external bias confirm the theoretical predictions**. As a result, the behaviour of the PN-junction under an external potential could be interpreted. Concerning the current density-voltage characteristic, an improvement of the numerical simulation accuracy is still possible. The tolerance factor could be reduced from 10^{-8} to 10^{-11} and an investigation on the refinement of the mesh for each external bias value could be performed to improve the convergences and prevent the oscillations observed. Concerning the emission spectrum, an optimisation could result from the determination of the bimolecular rate of Cu_2O:Mg and by taking into account the imperfections related by the experiment (leakage current, defects, contact resistance, *etc.*). The investigation of the behaviour of the PN-junction as function of the defects concentration can also highlight the impact of these ones in comparison to the experimental results.

The purpose of the experimental study was to grow TCO thin films using RF magnetron sputtering deposition. AZO and Cu_2O:Mg TCOs were studied and the enhancement of their respective transmittance in the [200;2000] nm wavelength range and their electrical resistivity was performed. Our study was particularly focused on the effect of the substrate temperature during deposition of both p-type and n-type layers. **The most efficient TCO properties were obtained at a deposition temperature of 250°C and at room temperature respectively for AZO and Cu_2O:Mg**. Another improvement of the TCO properties for both thin films were obtained by working on minimizing the residual pressure inside the deposition chamber. As summary of the obtained results, the electrical conductivity and the optical transparency of the TCO materials fabricated in this work are compared to references of the literature in Fig.7.1 [17]. The fabrication and the optimisation of transparent conductive AZO and Cu_2O:Mg thin films were therfore achieved in this work. Microscope imaging at a sub-micrometer scale was

an essential characterisation technique used all along this work in order to understand the film microstructure evolution as function of the deposition parameters.

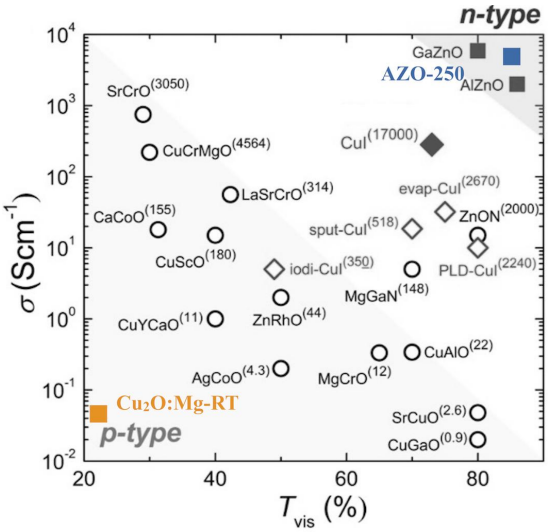

Fig. 7.1: Key properties of AZO and Cu_2O:Mg thin films deposited by RF magnetron sputtering in this work among TCOs results obtained in the literature [17].

As perspectives for the enhancement of the materials studied in this work, the investigation of the argon pressure in order to enhance their optical and electrical properties seem a first useful step. An increase of the sputtering power and consequently of the deposition rate could also lead to an improvement of the TCOs properties. Vacuum annealing of the AZO layers is also a possible improvement. In order to understand completely the influence of the annealing on the thin film properties, an investigation of the annealing time and the annealing temperature would be useful.

Concerning the experimental methodology, an improvement of the Hall measurement can be performed especially for Cu_2O:Mg for which the determination of the electrical properties were not reproducible. A possible enhancement can be performed concerning the electrical contact used as well.

Finally, two types of heterostructures have been fabricated by successive thin film depositions. The electrical and optical properties of each layer of the structure could be measured and confirmed by the use of a witness sample that was deposited in the same time at each deposition step. **Both PN-junctions present a rectifying behaviour** which has been the main purpose of this experimental part. The AZO-250/Cu_2O:Mg-RT junction presents a weaker rectifying behaviour in comparison to the AZO-250/Cu_2O:Mg-200 heterostructure. This result is quite interesting, however the interpretation of the result is not straightforward. A reason could be that the interface created between both semiconductors better defined and in addition, the thermal energy provided during the deposition of the second layer induces surface diffusion and rearrangement leading to an improvement of the crystallinity of the layers. The series resistances of both heterojunctions are equivalent. Nevertheless, the emission spectrum of the manufactured junction could not be obtained. Indeed, an investigation of the electrical contacts and of the different interfaces is required, aiming at reducing the contact resistance in order to isolate

the contribution of the PN-junction. As suggested, elemental analysis by secondary ions mass spectrometry could confirm the atomic diffusion of gold responsible for the short circuit observed in the current versus voltage measurement of some heterostructures. Ic could also be used to highlight the sharpness of the interface by measuring the respective atomic concentrations as a function of the depth. Finally, as presented in Annexe A, a measurement of the capacitance-voltage characteristic of the device can also be performed in order to obtain the depletion width of the PN-junction. Good electrical contacts are nevertheless required for this type of measurement.

As far as the structure of the junction is concerned, several optimisation of the design can be proposed in order to improve the efficiency of the PN-junction used as LED. For instance, an improvement of the minority charge carrier confinement could be performed by reducing the size of the device in other dimensions, using electron beam lithography. Such an approach would therefore aim at designing 1D (nanowire or nanopillar) or 0D (quantum dot) structures.

Bibliography

[1] N. Zheludev, *The life and times of the LED – a 100-year history*, Nature Photonics **1**, 189 (2007).

[2] H. J. Round, *A note on carborundum*, Electrical World **49**, 309 (1907).

[3] O. Lossev, *Luminous carborundum detector and detection effect and oscillations with crystals*, The London, Edinburgh, and Dublin Philosophical Magazine and Journal of Science **6**, 1024 (1928).

[4] E. F. Schubert, *Light-Emitting Diodes*, 2 ed. (Cambridge University Press, 2006).

[5] The Royal Swedish Academy of Sciences, *Efficient blue light-emitting diodes leading to bright and energy-saving white light sources*, (2014).

[6] J. Y. Tsao, *Solid-state lighting: lamps, chips, and materials for tomorrow*, IEEE Circuits and Devices Magazine **20**, 28 (2004).

[7] The Royal Swedish Academy of Sciences, *Blue LEDs – Filling the world with new light*, (2015).

[8] U.S. Department of Energy, *Energy Savings Potential of Solid-State Lighting in General Illumination Applications*, (2012).

[9] I. L. Azevedo, M. G. Morgan, and F. Morgan, *The transition to solid-state lighting*, Proceedings of the IEEE **97**, 481 (2009).

[10] S. T. Tan, X. W. Sun, H. V. Demir, and S. P. DenBaars, *Advances in the LED Materials and Architectures for Energy-Saving Solid-State Lighting Toward "Lighting Revolution"*, IEEE Photonics Journal **4**, 613 (2012).

[11] International Energy Agency, *Light's labour's lost policies for energy-efficient lighting.*, (2006).

[12] P. Waide, *Phase Out of Incandescent Lamps: Implications for International Supply and Demand for Regulatory Compliant Lamps*, IEA Energy Papers **5**, 1 (2010).

[13] Y.-H. Zhang, Z.-X. Mei, H.-L. Liang, and X.-L. Du, *Review of flexible and transparent thin-film transistors based on zinc oxide and related materials*, Chinese Physics B **26**, 047307 (2017).

[14] J. F. Wager, D. A. Keszler, and R. E. Presley, *Transparent Electronics* (Springer, 2008).

[15] A. Facchetti and T. Marks, *Transparent electronics: from synthesis to applications* (John Wiley & Sons, 2010).

[16] H. Kawazoe *et al.*, *P-type electrical conduction in transparent thin films of $CuAlO_2$*, Nature **389**, 939 (1997).

[17] C. Yang, M. Kneib, M. Lorenz, and M. Grundmann, *Room-temperature synthesized copper iodide thin film as degenerate p-type transparent conductor with a boosted figure of merit*, Proceedings of the National Academy of Sciences **113**, 12929 (2016).

[18] J. Avelas Resende, *Copper-based p-type semiconducting oxides: from materials to devices*, PhD thesis, University of Liege, (2017).

[19] L. D. Shah and S. M. Gulhane, *Transparent Electronics*, International Journal of Advanced Electrical and Electronics Engineering **2**, 1 (2013).

[20] C. Tsakonas *et al.*, *Transparent and Flexible Thin Film Electroluminescent Devices Using HiTUS Deposition and Laser Processing Fabrication*, IEEE Journal of the Electron Devices Society **4**, 22 (2018).

[21] P. P. Warke, *A Study on Transparent Electronic Devices*, International Journal of Innovative Research in Computer and Communication Engineering **5**, 1 (2017).

[22] B. Baert, *Impact of electron trap states on the transport properties of GeSn semiconducting heterostructures assessed by electrical characterizations*, PhD thesis, University of Liege, (2016).

[23] B. G. Streetman and S. K. Banerjee, *Solid state electronic devices*, 6 ed. (Prentice-Hall, 2005).

[24] N. D. Nguyen, *Physics of semiconductors lecture*, University of Liege, (2016-2017).

[25] R. N. Hall, *Electron-hole recombination in germanium*, Phys. Rev. **87**, 387 (1952).

[26] W. Shockley and W. T. Read, *Statistics of the recombinations of holes and electrons*, Phys. Rev. **87**, 835 (1952).

[27] M. Grundman, *The Physics of Semiconductors: An Introduction Including Nanophysics and Applications*, 2 ed. (Springer, 2006).

[28] B. Venderheyden, *Nanoelectronics/Optoelectronics lecture*, University of Liege, (2017-2018).

[29] S.-C. S. Jian-Jang Huang, Hao-Chung Kuo, *Nitride semiconductor light-emitting diodes (LEDs): Materials, performance and applications*, 2 ed. (Woodhead, 2018).

[30] P. D. C. King and T. D. Veal, *Conductivity in transparent oxide semiconductors*, Journal of Physics: Condensed Matter **23**, 334214 (2011).

[31] D. Smith, *Thin-Film Deposition: Principles and Practice* (McGraw-Hill Education, 1995).

[32] K. Wasa, M. Kitabatake, and H. Adachi, *Thin film materials technology: sputtering of control compound materials* (Springer Science & Business Media, 2004).

[33] J. A. Thornton, *Structure-zone models of thin films*, International Society for Optics and Photonics **821**, 95 (1988).

[34] A. C. Jones and M. L. Hitchman, *Chemical vapour deposition: precursors, processes and applications* (Royal Society of Chemistry, 2009).

[35] P. Savale, *Physical vapor deposition (PVD) methods for synthesis of thin films: A comparative study*, Archives of Applied Sciences Research **8**, 1 (2016).

[36] D. A. Jameel, *Thin film deposition processes*, International Journal of Modern Physics **1**, 193 (2015).

[37] N. D. Nguyen and A. Silhanek, *Nanofabrication lecture*, University of Liege, (2017-2018).

[38] J. Robertson and C. Clapp, *Removal of metallic deposits by high-frequency currents*, Nature **132**, 479 (1933).

[39] H. Hertz, *Ueber den druck des gesättigten quecksilberdampfes*, Annalen der Physik **253**, 193 (1882).

[40] M. Knudsen, *Experimentelle bestimmung des druckes gesättigter quecksilberdämpfe bei 0 und höheren temperaturen*, Annalen der Physik **334**, 179 (1909).

[41] S. Morohashi *et al.*, *Characteristics of superconducting Nb layer fabricated using high-vacuum electron beam evaporation*, Japanese Journal of Applied Physics **40**, 576 (2001).

[42] S. Rahmane, M. S. Aida, M. A. Djouadi, and N. Barreau, *Effects of thickness variation on properties of ZnO:Al thin films grown by RF magnetron sputtering deposition*, Superlattices and Microstructures **79**, 148 (2015).

[43] P. Samanta, *Review on wet chemical growth and anti-bacterial activity of zinc oxide nanostructures*, J Tissue Sci Eng **8**, 2 (2017).

[44] Y. Malier, *Radio-frequency magnetron deposition of transparent conducting thin films based on ZnO and Cu_2O for photovoltaic applications*, Master thesis, University of Liege, (2017).

[45] J. Avelas Resende, N. D. Nguyen, J.-L. Deschanvres, and C. Jimenez, *Magnesium-doped cuprous oxide (Mg: Cu_2O) thin films as a transparent p-type semiconductor oxide*, physica status solidi (a) **213**, 2296 (2015).

[46] R. Frerichs and R. Handy, *Electroluminescence in cuprous oxide*, Physical Review **113**, 1191 (1959).

[47] P. Nunes, D. Costa, E. Fortunato, and R. Martins, *Performances presented by zinc oxide thin films deposited by r.f. magnetron sputtering*, Vacuum **64**, 293 (2002).

[48] B. S. Chun *et al.*, *The effect of deposition power on the electrical properties of Al-doped zinc oxide thin films*, Applied Physics Letters **97**, 082109 (2010).

[49] J. Chang, H. Wang, and M. Hon, *Studying of transparent conductive ZnO:Al thin films by RF reactive magnetron sputtering*, Journal of Crystal Growth **211**, 93 (2000).

[50] A. Spadoni and M. L. Addonizio, *Effect of the RF sputtering power on microstructural, optical and electrical properties of Al doped ZnO thin films*, Thin Solid Films **589**, 514 (2015).

[51] Y. Igasaki and H. Saito, *The effects of deposition rate on the structural and electrical properties of ZnO:Al films deposited on (1120) oriented sapphire substrates*, Journal of Applied Physics **70**, 3613 (1991).

[52] Y. Kim *et al.*, *Effects of substrate temperature and Zn addition on the properties of Al-doped ZnO films prepared by magnetron sputtering*, Applied Surface Science **255**, 7251 (2009).

[53] N. M. S. Jahed, M. Mahmoudysepehr, and S. Sivoththaman, *Deposition and parametric analysis of RF sputtered ZnO:Al thin films with very low resistivity*, Materials Research Express **3**, 116402 (2016).

[54] S. Cornelius *et al.*, *Achieving high free electron mobility in ZnO:Al thin films grown by reactive pulsed magnetron sputtering*, Applied Physics Letters **94**, 042103 (2009).

[55] T. Minami, H. Sato, T. Sonoda, H. Nanto, and S. Takata, *Influence of substrate and target temperatures on properties of transparent and conductive doped ZnO thin films prepared by r.f. magnetron sputtering*, Thin Solid Films **171**, 307 (1989).

[56] D. K. Kim and H. B. Kim, *Room temperature deposition of Al-doped ZnO thin films on glass by RF magnetron sputtering under different Ar gas pressure*, Journal of Alloys and Compounds **509**, 421 (2011).

[57] M. Nie, A. Bikowski, and K. Ellmer, *Microstructure evolution of Al-doped zinc oxide and Sn-doped indium oxide deposited by radio-frequency magnetron sputtering: A comparison*, Journal of Applied Physics **117**, 155301 (2015).

[58] S. H. Jeong, J. W. Lee, S. B. Lee, and J. H. Boo, *Deposition of aluminum-doped zinc oxide films by RF magnetron sputtering and study of their structural, electrical and optical properties*, Thin Solid Films **435**, 78 (2003).

[59] W. Jeong, S. Kim, and G. Park, *Preparation and characteristic of ZnO thin film with high and low resistivity for an application of solar cell*, Thin Solid Films **506-507**, 180 (2006).

[60] H. Tong *et al.*, *Effects of post-annealing on structural, optical and electrical properties of Al-doped ZnO thin films*, Applied Surface Science **257**, 4906 (2011).

[61] L. J. van der PAUW, *A method of measuring the resistivity and Hall coefficient on lamellae of arbitrary shape*, Philips Technical Review **20**, 220 (1958).

[62] E. H. Hall, *On a new action of the magnet on electric currents.*, American Journal of Mathematics **2**, 287 (1879).

[63] F. Biccari, *Defects and doping in Cu_2O*, PhD thesis, University of Roma, (2010).

[64] V. Quemener, *Electrical Characterization of Bulk and Thin Film Zinc Oxide*, PhD thesis, University of Oslo, (2012).

[65] F. Hajakbari, A. Hojabri, M. Gholami, and M. Ghoranneviss, *Calculation of Cu_2O thin film optical constants using the transmittance data*, ISPC Proceedings, Bochum (2009).

[66] V. Tvarozek *et al.*, *Preparation of transparent conductive AZO thin films for solar cells*, 2008, Advanced Semiconductor Devices and Microsystems, International Conference on, 275 (2008).

[67] B. Shantheyanda, V. Todi, K. Sundaram, A. Vijayakumar, and I. Oladeji, *Compositional study of vacuum annealed Al-doped ZnO thin films obtained by RF magnetron sputtering*, Journal of Vacuum Science & Technology A: Vacuum, Surfaces, and Films **29**, 051514 (2011).

[68] O. Kluth *et al.*, *Modified Thornton model for magnetron sputtered zinc oxide: film structure and etching behaviour*, Thin Solid Films **442**, 80 (2003).

[69] P. Giri, C. Narayan, S. Vyas, and P. Chakrabarti, *Comparative studies on the characteristics of ZnO thin films deposited by single-step and two-step method using RF sputtering*, Devices, Circuits and Communications International Conference on, 1 (2014).

[70] M. Rasadujjaman, M. Shahjahan, M. Khan, and M. Rahman, *Deposition and characterization of p-Cu_2O thin films*, SUST Journal of Science and Technology **20**, 1 (2012).

[71] M. El Yacoubi, R. Evrard, N. D. Nguyen, and M. Schmeits, *Electrical conduction by interface states in semiconductor heterojunctions*, Semiconductor science and technology **15**, 341 (2000).

Appendix A

Characterization Complement

This annexe provides additional information concerning the morphological characterization of the independent layers and of the PN-junction. The method used to determine the thickness of the thin films is also presented. Finally, an additional electrical characterization of the PN-junction is presented as perspective.

A.1 Structural and Morphological Characterization

Scanning Electron Microscope (SEM) imaging was used to study crystallinity of layer by a high resolution and magnification observation of the thin films. These observations provide information about the crystallinity in order to locate in the Thornton' structure-zone model (cfr. Chapter 3). These SEM images also allow to observe the interface of the heterojunction and the stacking of the different layers. Then thanks to a Dektak measurement, the thickness t [nm] of the films is also obtaind. As presented in Section 4.2 and 4.1 the thickness of the deposited thin film is critical. Indeed, this one is involved in the resistivity calculation (cfr. Eq.(4.4)) and in the absorption coefficient relation (cfr. Eq(4.19)).

Fig. A.1: Raith Pioneer Two electron beam lithography platform and SEM.

The SEM used in the SPIN research group is a Pioneer Two electron beam lithography platform and scanning electron microscope from Raith[1] (cfr. Fig.A.1). This tool provide the resolution and the magnification required in order to observe the surface of the deposited layer at a nanoscopic scale. Thanks to the SEM imaging the crystallinity and the morphology of the thin films can be observed and related to electrical and optical properties.

The Dektak used in order to obtain the thickness of the thin film is a profilometer. The profilometry is a measurement technique used in order to obtain the macroscopic roughness of a materials. This one allows the characterization of the surface profile on large scale (several millimetres). The tip of the profilometer which has a dimension of the order of the micrometer enter in physical contact with the sample. This one perform a displacement along a straight direction on the sample by recording the height variation of the tip. The resolution of the profile obtained is a convolution product between the sample surface roughness and the shape of the tip. The usage of this technique is motivated by the swiftness and the convenient accuracy of the measurement. The average standard deviation of the thickness measurement is 7.844%. The Dektak device is consequently able to monitor a thickness difference of the order of the 100 nm with accuracy.

A.2 PN-Junction Electrical Characterization: Capacitance-Voltage Characteristic

The capacitance-voltage measurement is a two-points measurement method allowing to obtain the depletion width W_d of the PN-junction. Indeed a capacitance can be associated to the depletion region C_d [F]. The depletion region is by definition, the region at the interface of two different doping semiconductors characterised by the depletion of free charge carriers and the presence of a space charge (cfr .Chapter 2). The material in this region can be assumed to be a dielectric material with an electrical permittivity $\epsilon = \epsilon_\mathrm{r}\epsilon_0$ [F m^{-1}] and the capacitance of the depletion region is given by equation A.1. Where S [m^2] is the surface of the metallic contact on the PN-junction and x corresponds to the width of the depletion region. This leakage current lead to an ohmic like behaviour of the I-V curve until the threshold voltage.

$$C(x) = \frac{\epsilon S}{x} \tag{A.1}$$

The representation of $1/C_\mathrm{d}^2$ as a function of the applied bias V [V] gives us information about the depletion region width Wd [m]. The carrier concentrations are known thanks to the VdP and Hall measurements on the independent thin films. Inserted these latter results in equation A.2, the only unknown value is the built-in contact potential V_0. This one is obtained by the intersection of the curve $1/C_\mathrm{d}^2$ with the x-axis.

$$W_d = \left(\frac{2\ \epsilon\ (V_0 - V)}{q}\left(\frac{1}{N_A} + \frac{1}{N_D}\right)\right)^{\frac{1}{2}} \tag{A.2}$$

[1]Further information on the device can be found at the following reference: `https://www.raith.com/products/pioneer.html` visited on May 8, 2018.

Appendix B

Numerical Simulation Results

B.1 Band Diagrams

Presentation of the band diagrams obtained for an external potential applied on the PN-junction ranging from -2 V to 3.5 V with the referring legend:

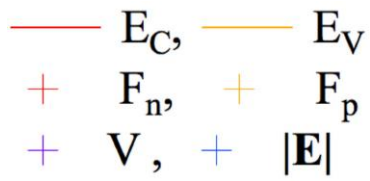

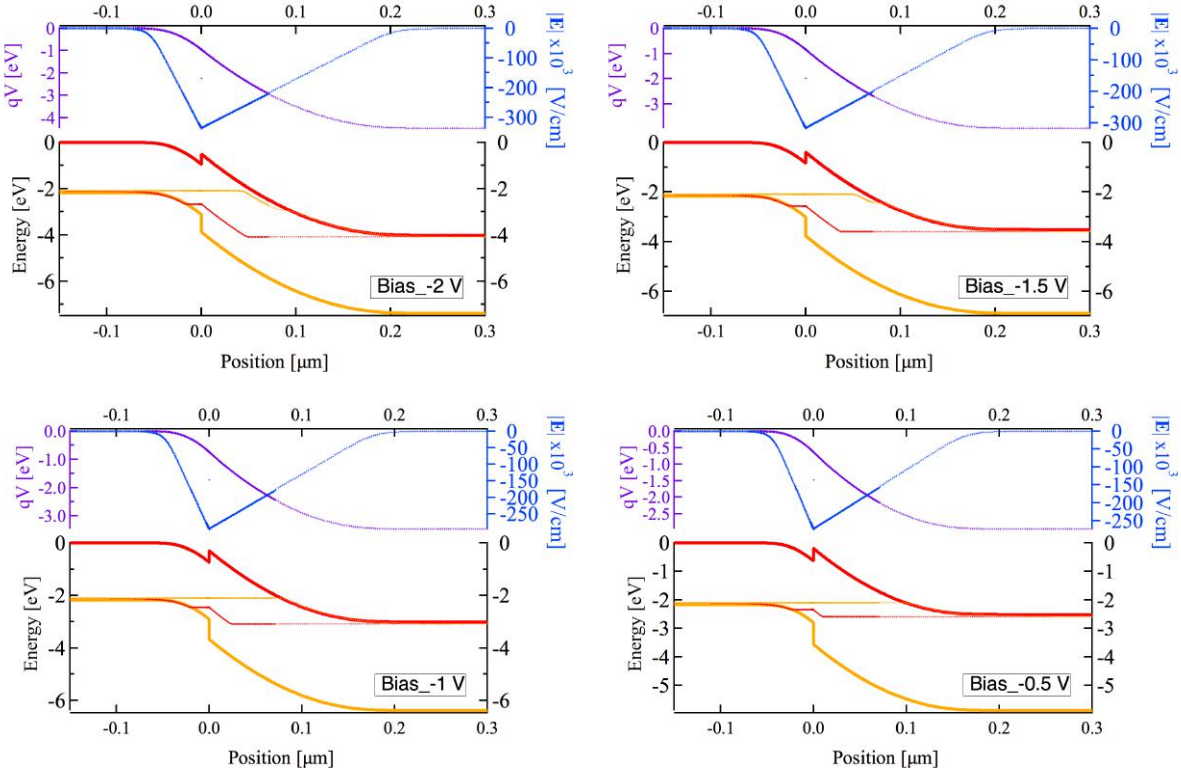

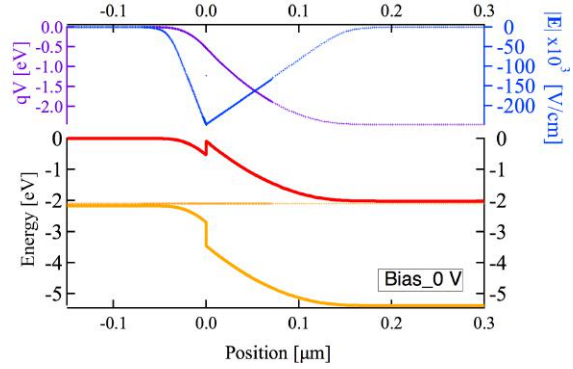
qV [eV]
|E| x10^3 [V/cm]
Energy [eV]
Bias_0 V
Position [μm]

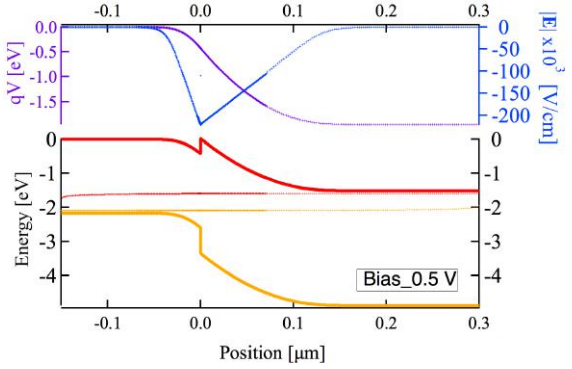
qV [eV]
|E| x10^3 [V/cm]
Energy [eV]
Bias_0.5 V
Position [μm]

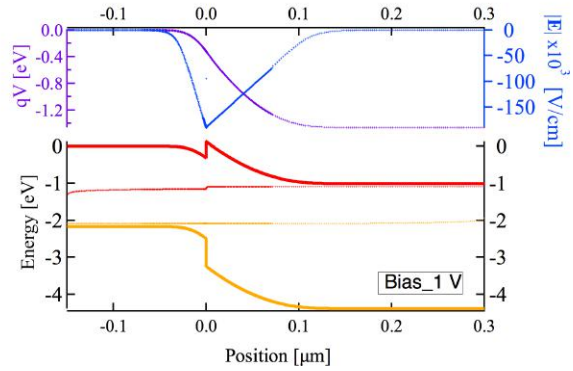
qV [eV]
|E| x10^3 [V/cm]
Energy [eV]
Bias_1 V
Position [μm]

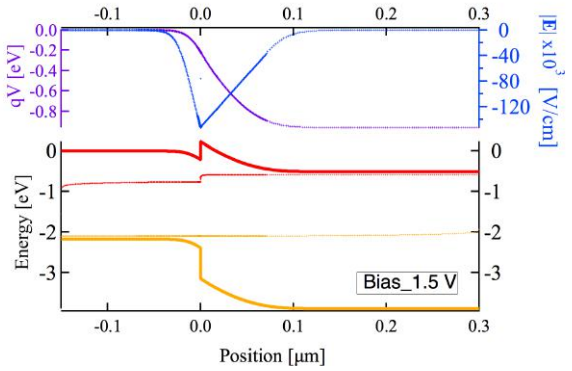
qV [eV]
|E| x10^3 [V/cm]
Energy [eV]
Bias_1.5 V
Position [μm]

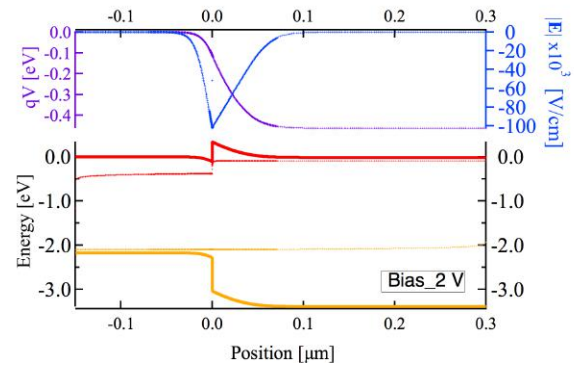
qV [eV]
|E| x10^3 [V/cm]
Energy [eV]
Bias_2 V
Position [μm]

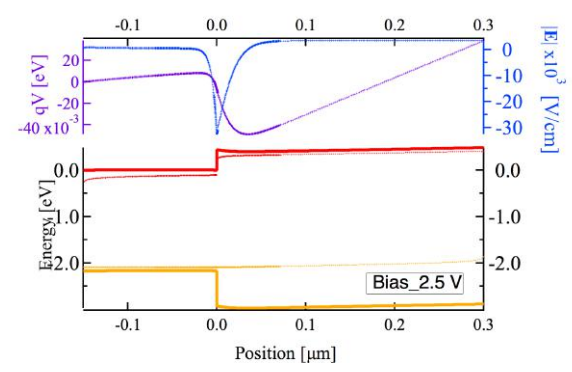
qV [eV]
|E| x10^3 [V/cm]
Energy [eV]
Bias_2.5 V
Position [μm]

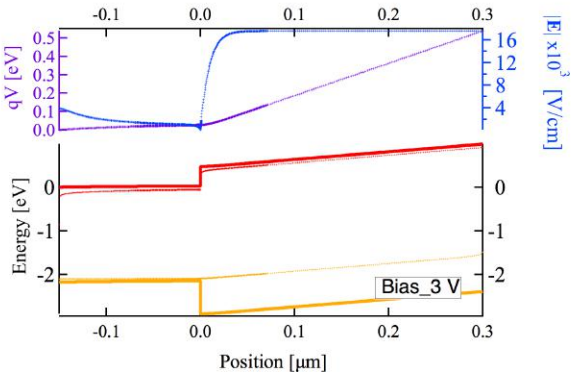
qV [eV]
|E| x10^3 [V/cm]
Energy [eV]
Bias_3 V
Position [μm]

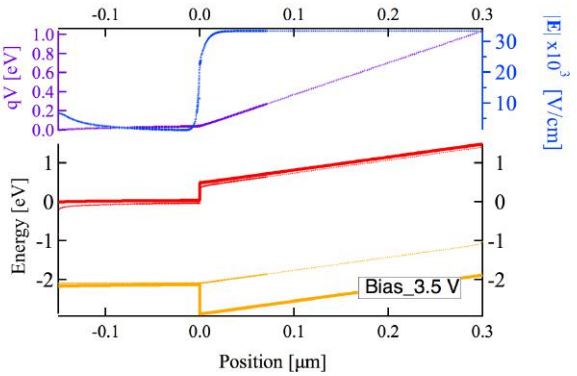
qV [eV]
|E| x10^3 [V/cm]
Energy [eV]
Bias_3.5 V
Position [μm]